SOCIAL BEHAVIOR BASED COLLABORATIVE SELF-ORGANIZATION IN MULTI-ROBOT SYSTEMS
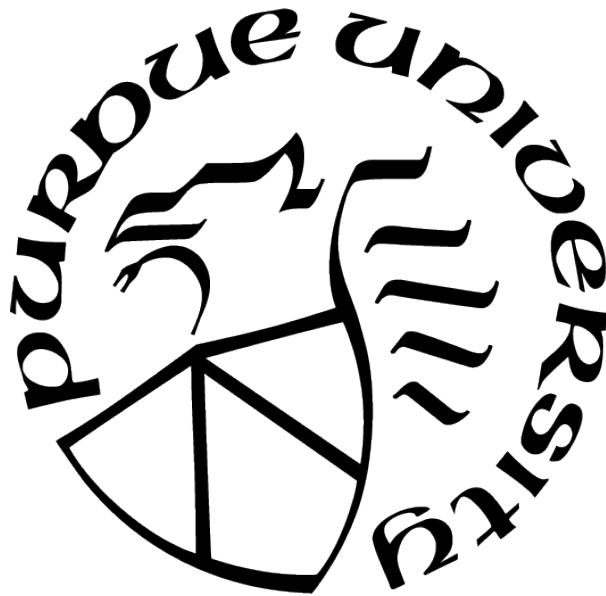
by

Tamzidul Mina

A Dissertation

Submitted to the Faculty of Purdue University

In Partial Fulfillment of the Requirements for the degree of

Doctor of Philosophy

Mechanical Engineering

West Lafayette, Indiana

December 2020

THE PURDUE UNIVERSITY GRADUATE SCHOOL
STATEMENT OF COMMITTEE APPROVAL

Dr. Galen B. King

School of Mechanical Engineering

Dr. Byung-Cheol Min

Department of Computer and Information Technology

Dr. Fabio Semperlotti

School of Mechanical Engineering

Dr. Seokcheon Lee

School of Industrial Engineering

Approved by:

Dr. Nicole L. Key

To my parents for all their sacrifice, love, endless support and encouragement.

ACKNOWLEDGMENTS

I would like to express my deepest gratitude to my co-advisors, Dr. Galen King and Dr. Byung-Cheol Min, for providing me the opportunity to work with them. I thank you for your patient advice, assistance and constant support over the years in helping me complete this research work and getting me where I am today. I would also like to thank my committee members Dr. Fabio Semperlotti and Dr. Seokcheon Lee for their time, effort and valuable contributions in the process. This dissertation would not have been possible without the strong support of my lab mates and research group members in SMART Laboratory to whom I will always be grateful.

I am forever indebted to my loving wife Maliha Hossain for all her sacrifice and unwavering support during my time in graduate school. You have been a constant source of inspiration to me through it all and I am lucky to have you by my side. Thank you for putting up with me over the years.

Lastly, I would just like to thank all my dear friends past and present for your friendship and support. My life just would not be the same without each and every one of you.

TABLE OF CONTENTS

LIST OF TABLES

LIST OF FIGURES

11

LIST OF SYMBOLS

N	total number of agents in the multi-robot system
r	agent position vector
v	agent velocity vector
u	agent control input
v_m	maximum robot linear velocity
ω_m	maximum robot rotational velocity
r_d	neighboring robot detection radius.

Chapter 2, Section 2.3

x, y	agent position
X, Y	stacked position arrays
b	agent battery level
B	stacked battery level array
c_y	global coordinate frame y-axis center-line
c_{A_i}	current charge potential of agent A_i
m	number of agents in 1st row of structured convoy formation
n	number of agents in 2nd row of structured convoy formation
μ_b^{use}	battery usage for unit movement by an agent
μ_{ca}	unit center advantage per unit time
Δt_c	time duration an agent is able to stay at the center
μ_{ca}^{min}	minimum center advantage
b_{use}	modeled general battery usage per unit time
b_{ad}	additional battery usage per unit time.

Chapter 2, Section 2.4

b	agent energy level
b_m	mean energy level of group
Δb_{ij}	difference in energy level between agents i and j
r_b	energy sharing radius

n	number of neighboring agents within r_b
β, ρ	scalar control gain constant
U	artificial potential function
$||r_{ij}||$	Euclidean distance between agents i and j
d_e	equilibrium distane between agents
μ_k	mean of agent positions in agent set k.

Chapter 3

r_c	initial robot group location vector
d_0	set equilibrium distance between agents
d_1	set radius for interaction between robots
n	number of neighbors detected within radius r_d
r_{ij}	distance between robots i and j
r_{ic}	distance of center robot i to r_c
v_f	inlet fluid velocity
ν	fluid viscous coefficient
$\beta_P, \beta_V, \alpha_I, \alpha_C, \alpha_d, \lambda$	scaling constants and weights
P_i^t and V_i^t	measured pressure and fluid velocity by robot i
$L_{threshold}$	health loss rate threshold to start relocating
F	artificial potential function
f	robot interaction force derived from F
k_{SE}	squared exponential kernel function
k_{SM}	spectral mixture kernel function
$m(x)$	mean function for Gaussian Processes Machine Learning
L_i^t	rate of health loss of robot i at time t
$L_i^c(t)$	cost function for global health loss rate minimum estimation
t_{int}	Gaussian Processes Machine Learning estimate time interval
L_i^g	total health loss travelling to global health loss rate minimum
L_i^l	total health loss settling at current health loss rate minimum
$_gH_i^t$	robot health relocating to the global health loss minimum

$_hH_i^t$	robot health relocating to the optimized health loss minimum
$_nH_i^t$	robot health when not allowed to relocate.

Chapter 4

r	distance to neighboring node
θ	angle of elevation to neighboring node
ψ	angle of azimuth to neighboring node
r_c	inter-robot communication radius
d_0	set equilibrium distance between agents
d_1	set radius for interaction between robots
r_{ij}	distance between robots i and j
X	shape structure representation matrix
V	set of nodes in in structure graph
E	set of edges in structure graph
O_i	parent robot of robot i
o_i	position vector of parent robot of robot i
$||r_i o_i||$	Euclidean distance between robot i and its parent
d_o	set surface following distance
b_i	surface gradient value of robot i
ε_i	bidding value of robot i
κ, α_a	scalar constants
v_r	random walk constant velocity
θ_r	random walk angle of elevation bound
ψ_r	random walk angle of azimuth bound

Chapter 5

O	arbitrary object
g	set goal location
θ	robot heading/orientation
ψ	angle of azimuth to neighboring node
$\theta_{i,g}$	direction to goal of robot i relative to its local frame

d_s	defined boundary following distance
d_e	set inter-robot safety distance
θ_{net}	collective heading angle error of all detected robots
o_i	nearest detected point on object by robot i
$\alpha, \rho_1, \rho_2, \rho_3, \rho_4, \rho_6$	scaling constants
ρ_5	modeled pushing effort
ϕ	acceptable heading angle error bound for relocation

ABBREVIATIONS

PHS   Penguin Huddling-inspired Shuffling

AIS   Adaptive Inter-agent Spacing

GPML   Gaussian Processes Machine Learning

ABSTRACT

Self-organization in a multi-robot system is a spontaneous process where some form of overall order arises from local interactions between robots in an initially disordered system. Cooperative coordination strategies for self-organization promote teamwork to complete a task while increasing the total utility of the system. In this dissertation, we apply prosocial behavioral concepts such as altruism and cooperation in multi-robot systems and investigate their effects on overall system performance on given tasks. We stress the significance of this research in long-term applications involving minimal to no human supervision, where self-sustainability of the multi-robot group is of utmost importance for the success of the mission at hand and system re-usability in the future.

For part of the research, we take bio-inspiration of cooperation from the huddling behavior of Emperor Penguins in the Antarctic which allows them to share body heat and survive one of the harshest environments on Earth as a group. A cyclic energy sharing concept is proposed for a convoying structured multi-robot group inspired from penguin movement dynamics in a huddle with carefully placed induction coils to facilitate directional energy sharing with neighbors and a position shuffling algorithm, allowing long-term survival of the convoy as a group in the field. Simulation results validate that the cyclic process allows individuals an equal opportunity to be at the center of the group identified as the most energy conserving position, and as a result robot groups were able to travel over 4 times the distance during convoying with the proposed method without any robot failing as opposed to without the shuffling and energy sharing process.

An artificial potential based Adaptive Inter-agent Spacing (AIS) control law is also proposed for efficient energy distribution in an unstructured multi-robot group aimed at long-term survivability goals in the field. By design, as an altruistic behavior higher energy bearing robots are dispersed throughout the group based on their individual energy levels to counter skewed initial distributions for faster group energy equilibrium attainment. Inspired by multi-huddle merging and splitting behavior of Emperor Penguins, a clustering and sequential merging based systematic energy equilibrium attainment method is also proposed as a supplement to the AIS controller. The proposed system ensures that high energy

bearing agents are not over crowded by low energy bearing agents. The AIS controller proposed for the unstructured energy sharing and distribution process yielded 55%, 42%, 23% and 33% performance improvements in equilibrium attainment convergence time for skewed, bi-modal, normal and random initial agent resource level distributions respectively on a 2D plane using the proposed energy distribution method over the control method of no adaptive spacing. Scalability analysis for both energy sharing concepts confirmed their application with consistently improved performances different sized groups of robots. Applicability of the AIS controller as a generalized resource distribution method under certain constraints is also discussed to establish its significance in various multi-robot applications.

A concept of group based survival from damaging directional external stimuli is also adapted from the Emperor Penguin huddling phenomenon where individuals on the damaging stimuli side continuously relocate to the leeward side of the group following the group boundary using Gaussian Processes Machine Learning based global health-loss rate minima estimations in a distributed manner. The method relies on cooperation from all robots where individuals take turns being sheltered by the group from the damaging external stimuli. The distributed global health loss rate minima estimation allowed the development of two settling conditions. The global health loss rate minima settling method yielded 12.6%, 5.3%, 16.7% and 14.2% improvement in average robot health over the control case of no relocation, while an optimized health loss rate minima settling method further improved on the global health loss rate settling method by 3.9%, 1.9%, 1.7% and 0.6% for robot group sizes 26, 35, 70 and 107 respectively.

As a direct application case study of collaboration in multi-robot systems, a distributed shape formation strategy is proposed where robots act as beacons to help neighbors settle in a prescribed formation by local signaling. The process is completely distributed in nature and does not require any external control due to the cooperation between robots. Beacon robots looking for a robot to settle as a neighbor and continue the shape formation process, generates a surface gradient throughout the formed shape that allow robots to determine the direction of the structure forming frontier along the dynamically changing structure surface and eventually reach the closest beacon. Simulation experiments validate complex shape formation in 2D and 3D using the proposed method. The importance of group collaboration

is emphasized in this case study without which the shape formation process would not be possible, without a centralized control scheme directing individual agents to specific positions in the structure.

As the final application case study, a collaborative multi-agent transportation strategy is proposed for unknown objects with irregular shape and uneven weight distribution. Although, the proposed system is robust to single robot object transportation, the proposed methodology of transport is focused on robots regulating their effort while pushing objects from an identified pushing location hoping other robots support the object moment on the other end of the center of mass to prevent unintended rotation and create an efficient path of the object to the goal. The design of the object transportation strategy takes cooperation cues from human behaviors when coordinating pushing of heavy objects from two ends. Collaboration is achieved when pushing agents can regulate their effort with one another to maintain an efficient path for the object towards the set goal. Numerous experiments of pushing simple shapes such as disks and rectangular boxes and complex arbitrary shapes with increasing number of robots validate the significance and effectiveness of the proposed method. Detailed robustness studies of changing weight of objects during transportation portrayed the importance of cooperation in multi-agent systems in countering unintended drift effects of the object and maintain a steady efficient path to the goal.

Each case study is presented independent of one another with the Penguin huddling based self-organizations in response to internal and external stimuli focused on fundamental self-organization methods, and the structure formation and object transportation strategies focused on cooperation in specific applications. All case studies are validated by relevant simulation and experiments to establish the effectiveness of altruistic and cooperative behaviors in multi-robot systems.

1. INTRODUCTION

The concept of multi-robot systems in robotics research was first proposed in the 1980s. A series of subsequent projects following its introduction, ACTRESS [1], GOFER [2], CEBOT [3], ALLIANCE [4], M+ [5], MURDOCH [6] and ASyMTRe [7] brought to light the immense potential of such systems to the research community. Potential advantages of multi-robot systems over single-robot systems include better spatial distribution, overall performance with regards to time required for task completion and energy consumption [8], [9], system robustness and fault tolerance resulting from redundancy [10], low cost, better system reliability, flexibility, scalability and versatility [11]. Multi-robot systems have since been widely proposed for numerous applications in exploration, monitoring, surveillance, search and rescue operations with research focused on coordination strategies between robots for self-organization [12]–[14]. A number of these systems have often been directed towards long-term applications in remote and dangerous locations with little to no human supervision; traditionally robots in such cases have been built to be individually self-sufficient and self-reliant [15], [16]. Regardless, the safety, security and survivability of these robots are important for the success of the mission.

Self-organization in a multi-robot system is a spontaneous process where some form of overall order arises from local interactions between robots in an initially disordered system without requiring any form of external control. Coordination between agents in a multi-robot system has been previously categorized as competitive or cooperative [17]. Competitive coordination strategies between individuals in such systems are considered selfish from a sociological point of view as individuals tends to make decisions motivated by self-preservation or some form of individual benefit. Cooperative coordination strategies on the other hand promote teamwork to complete a task while increasing the total utility of the system. A literature survey of prior work on this coordination distinction has been previously presented in [18]. Under a cooperative system, individuals can benefit as a social group by looking out for one another for support and survival. It is a proven phenomenon in nature with examples including foraging behavior in ant colonies for food [19], formation flying of birds allowing individuals to take turns resting during long flights [20], schooling of fish for en-

hanced predator detection and evasion [21] etc. amongst many. The research presented in this dissertation applies similar principles of social behavior and cooperation in a multi-robot system to improve robustness in terms of robot group survivability, self-sustainability and improved application specific performance. For part of the work, bio-inspiration has been derived from the huddling behavior of Emperor Penguins in the Antarctic surviving long extreme winters as a group.

Social behavioral concepts have historically been studied within groups of living organisms. In the robotics area social behavioral concept application has generally remained confined to human-robot interactions, where robots are designed to interact with people in a natural, interpersonal manner in areas such as education, health, entertainment, and tasks requiring collaborative teamwork [22]. In this dissertation, we focus specifically on the prosocial behavioral concepts of altruism [23] and cooperation [24] applied in multi-robot systems governing inter-robot interaction for the benefit of the group. It can be argued that social behavioral concepts require an innate will by individuals to help or work with others in the group, while being self-aware of one's actions and its consequences to the extent of understanding and prioritizing the need of the group over oneself. However, we emphasize here that prescribed behavioral characteristics by individuals can be just as effective in their outcome to benefit the group.

Individual robots determine their course of action based on a given set of current observation and analysis. Traditionally in cooperative robot groups, the decision making process has been confined to individual assessment maximizing individual gain or minimizing system cost at a given time [25]–[27]. As a step towards implementing prescribed altruistic behaviors in multi-robot systems, this research presents behavioral concepts by individual agents in different applications in a group that is based on trust that its current course of action might not result in immediate individual gain and may even be detrimental to itself, with the expectation that others will exhibit the same behavior in return for the overall benefit of the entire group. Although, cooperation in multi-robot systems have been previously proposed in applications such as localization [28] [10], exploration [9] [29], search and rescue [30], the benefits of altruistic behaviors or a combination of the two increasing the total utility of the group to the best of our knowledge has never been studied in the multi-robot area.

We stress the significance of this research in long-term applications involving minimal to no human supervision where self-sustainability of the multi-robot group is of utmost importance for the success of the mission at hand and re-usability in the future. Self-organization methods studied in this research include several group energy sharing and group surviving strategies for multi-robot systems, along with specific multi-robot applications of cooperative shape formation and object transportation requiring or relying on inter-agent support.

The dissertation chapters are organized as follows. Chapter 2 presents an Emperor Penguin huddling inspired, index-based cyclic energy sharing concept in convoying structured multi-robot systems. Individual robots are modeled as Emperor Penguin-based energy sharing units analogous to body warmth sharing in huddling Emperor Penguins during Antarctic winters while the group is on the move. A Position shuffling algorithm is presented for the robot group for cyclic flank movements allowing all individuals an opportunity to be in the center of the group which is shown to be the optimum place for energy sharing. Chapter 2 also presents an adaptive inter-agent spacing control law for efficient energy distribution in an unstructured multi-robot system with a supplementary clustering and sequential merging process to reach global equilibrium in large swarms inspired by the continuous splitting and merging of Emperor Penguin huddles sharing body heat. Inter-robot interaction is modeled as artificial potentials and the proposed concept is validated with simulation experiments. Chapter 3 introduces an Emperor Penguin huddling based multi-robot group survival strategy from damaging directional external stimuli without any human intervention. Individuals on the exposed side of the group successfully relocate to the global and optimum low health-loss rate position in the group to settle on the leeward side in a distributed manner following two separate settling criteria, without requiring any communication or prior knowledge of the group size or shape. Gaussian Processes Machine Learning is implemented by individuals for minimal health loss location estimation using only local stimuli measurements. The proposed energy sharing and continuous cyclic relocations for energy sharing and surviving damaging external stimuli improve the overall survivability of the robot group with no robots left behind as validated by relevant simulations.

Lastly, as direct applications of inter-robot cooperative self-organization, Chapters 4 and 5 present a collaborative shape formation method based on robots guiding one another for neighboring-robot settling to form prescribed shapes, and a transportation strategy for objects of unknown, irregular shape, size and properties in multi-robot systems. Artificial potential fields and a finite state machine controller governs the interaction between robots and avoid collision, while completing the respective application specific tasks. Validation of proof of concept of the proposed shape formation strategy and object transportation method are presented with successful simulation and experimental results with a focus on inter-agent cooperation and its benefits to the system.

Each application chapter includes its own relevant literature review on the topic along with their respective assumptions, list of variables and symbols used. The dissertation is concluded with closing notes on possible implications of the presented concepts in each of the chapters, and the overall contribution of the dissertation in the field of self-sustaining multi-robot systems relying on social and cooperative behaviors.

1.1 Preliminaries: Bio-inspiration of Social Behavior from the Huddling Behavior of Emperor Penguins in the Antarctic

Chapters 2 and 3 of this dissertation present cooperative energy sharing and group survival concepts proposed for multi-robot systems deployed on long-term missions without any human supervision. The research work is partially based on the huddling behavior of Emperor Penguins in the Antarctic surviving long extreme winters as a group. In this section, a brief description of this huddling phenomenon and its social implications in surviving as a group is presented along with relevant prior work on the topic. Further details of this huddling behavior relevant to each research work presented in this dissertation is included in their respective chapters.

Every winter, thousands of Emperor Penguins (Aptenodytes forsteri) in the Antarctic survive one of the harshest environments on Earth together as a group [31]. To survive the severe cold conditions during storms and low ambient temperatures, they huddle together from several hours [32] to even days [33] depending on weather conditions as depicted in Fig. 1.1a. This allows them to conserve and share body heat with one another; survive

25

(a) Emperor Penguins huddle together in tightly packed structures in winter conditions [39].

(b) Penguin huddling in the Antarctic winter showing boundary movements from the windward to the leeward side. Image taken from the PBS Nature show.

Figure 1.1. Huddling behavior of Emperor Penguins in the Antarctic to survive long extreme winters as a group.

winds over 100mph and temperatures below -45^oC [34]. The huddles are not motionless. Penguins that are most exposed to strong winds, slowly advance along the flanks downwind to receive shelter behind the huddle [35]. This eventually causes penguins that were previously at the center to be exposed and they start to move along the flanks to the leeward side in turn as well accumulating behind the penguins that moved in before them. This flank movement and constant shuffling of the penguins in the huddle ensure that each penguin has an approximately equal opportunity for warmth and none are left behind [35].

The huddling behavior of Emperor penguins in the Antarctic has been studied extensively, but very few theoretical models have been presented in literature so far. One theoretical model of position shuffling was presented based on observations that Emperor penguins move from the windward to the leeward side in a huddle [36]. This work was continued by taking into account models of wind flow and the temperature profile around the huddle in [37]. Their model was based on a simple rule that individual penguins relocate themselves in the huddle to a new position where its heat loss is minimized, without displacing another. The huddle was modeled as a hexagonal grid based on [34]. The huddling behavior was modeled as a second order phase transition triggered by cold temperatures in [38]. The work was validated experimentally with a group of mice and suggested huddling as a self-organizing event relevant among large groups of endotherms such as penguins.

A lot of inspiration on multi-robot research has come from collective behaviors of biological organisms such as ant colonies [19], flocking of birds [20], schooling of fish [21] etc. The huddling behavior of penguins shares some behavioral traits with some of the above-mentioned organisms, but their social behavioral characteristics for group survival have remained untouched. It allows them to look out for one another so that the entire population of the colony may survive the whole winter as one unit. Upon literature review, no studies have been found where the huddling phenomenon has inspired any potential work in the multi-robot arena.

2. ENERGY SHARING AND DISTRIBUTION

The material in this chapter of the dissertation is partially based on the following previously published papers. The content has been added with the consent of all co-authors of all papers.

- "Penguin Huddling-inspired Energy Sharing and Formation Movement in Multi-robot Systems," T. Mina, B.C. Min, 2018 IEEE International Symposium on Safety, Security, and Rescue Robotics (SSRR), Philadelphia, PA, USA, August 6-8, 2018.

- "Efficient Resource Distribution by Adaptive Inter-agent Spacing in Multi-agent Systems," T. Mina, M. Hossain, J.H. Park and B.C. Min, 2019 IEEE International Conference on Systems, Man and Cybernetics (SMC), Bari, Italy, October 6-9, 2019.

2.1 Introduction

Multi-robot systems have the potential for application in various long-term missions such as surveillance, monitoring, exploration etc covering large areas at a time. Self-sustainability is a vital requirement in such cases where human supervision may not be available. Depending on the application, each robot in the group may have a different role in the team, different hardware and movement actuation requirements; therefore, may use different levels of battery. Different units may even use different types/sizes of batteries altogether requiring different recharging times and processes. Regardless of having some on-board battery re-charging system (e.g. solar cells), the duration of continuous survival/work of the entire unit together is only as strong as the robot with the lowest battery life.

This chapter includes energy sharing and distribution concepts for convoying structured and unstructured robot groups on long-term missions. The proposed concepts rely on neighboring agents supporting one another by sharing or distributing energy, or self-organizing in a systematic process by design where their immediate action might be detrimental to themselves but serves as beneficial to all in the long run. A cyclic energy sharing concept using carefully placed induction coils for a structured group of robots convoying over large distances in long-term missions is presented in Section 2.3 followed by an Adaptive Inter-agent

Spacing (AIS) control based self-organization process with group clustering and sequential merging formulations for efficient global energy equilibrium attainment in multi-robot systems in Section 2.4 to ensure that entire multi-robot teams can survives longer in the field as a group. The proposed cyclic energy sharing method for structured robot groups in convoy is directly inspired by the huddling behavior of Emperor Penguins presented in Section 1.1.

2.2 Related Work

The term trophallaxis is used in entomology to describe a mutual exchange of regurgitated fluids between social insects [40]. It is also used in the multi-robot arena as exchanging information [41] or energy [42] between agents. As a solution of energy transfer between agents, a method of physical battery swapping between robots was proposed in [41]. However, the mechanism is complicated and lacks robustness for application in a heterogeneous robot group. An energy usage optimization approach for a multi-robot system inspired by the foraging behavior and energy management of honeybees was proposed in [42]. This method improves individual robot performance but fails to utilize the advantage of being in a group.

A number of wireless power transmission methods has been summarized by [43] and an efficient non-contact method using inductive coils was patented in [44]. An image processing based proper alignment of the induction coils for wireless charging between robotic agents was later proposed in [45]. The coil alignment was later improved upon with a Bayesian estimator in [46].

The work in [45] proves the feasibility of wireless charge sharing between robots. The energy sharing concepts presented in this chapter builds on this prior work by providing feasible self-organization methods within the group for energy sharing and distribution irrespective of heterogeneity constraints to extend the life of the group in the field.

2.3 Structured Self-organization for Cyclic Energy Sharing

In this section, the survival of a group of heterogeneous robots deployed on a long-term mission to a remote location and on the move from site A to site B is considered. Studying the

(a) Close packing of huddling penguins from Nature by PBS showing an individual A_i and its neighbors indexed $j \in (1, 2, .., 8)$.
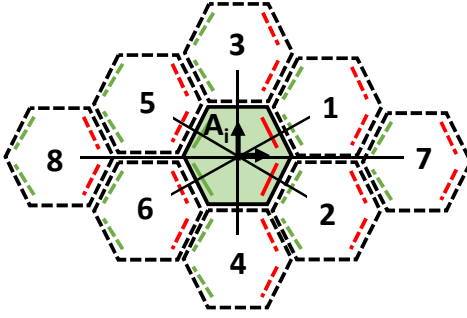
(b) Top view of neighboring agents modeled from (a).
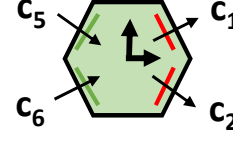
(c) Top view of individual agent showing inductive coil placement for energy sharing with neighbors.

Figure 2.1. Individual agent and group configuration based on close packing of huddling penguins.

social behavior of Emperor penguins for group survival, the following concepts are proposed to ensure the survival of the entire convoy for a longer period of time in the field:

- A gradient based multi-robot charge sharing concept using carefully placed inductive coils.

- A position shuffling algorithm (PHS) for a group of robots to move to the center of the formation in turns.

2.3.1 Methodology

Formation building block - Single agent Setup with Gradient based Charge Sharing

Huddling of Emperor penguins involves dense packing for maximal body heat sharing and retainment as shown in Fig. 2.1a. In two dimensional euclidean space, the highest

density lattice arrangement of circles is the hexagonal packing [47]. Therefore, we consider the hexagonal lattice formation for our proposed group of robots and note an individual's neighbors as shown in Fig. 2.1b following Fig. 2.1a.

A hexagon structured robot is proposed as a concept for the charge sharing robot unit as shown in Fig. 2.1c. Each agent is equipped with four induction coils; two coils upfront marked in red to only transmit power to two front agents and two coils at the back marked in green to only receive power from two rear agents. Charge transfer occurs when there is a battery level difference between adjacent agents. Each side has a single coil only due to size restrictions of the robot and efficiency requirements of the charge transfer process dependent on the diameter of the coils [45]. In this study we only consider four coils rather than six on each robot to minimize energy usage in transferring energy.

Consider an agent A_i, $i \in D$ for $D = \{1, 2, 3, .., N\}$ with battery level b_i and its neighboring agents A_j, $j \in \{1, 2, .., 8\}$ with battery levels b_j respectively as shown in Fig. 2.1b. The proposed gradient based charge sharing scheme of agent A_i with surrounding agents A_j is shown in (2.1)-(2.3):

$$\Delta_{ij} = b_i - b_j, \tag{2.1}$$

$$f(b_i, b_j)_{\forall j \in (1,2)} = \begin{cases} K\Delta_{ij} & \Delta_{ij} > 0, \ K\Delta_{ij} \leq \Delta_t \\ \Delta_t & \Delta_{ij} > 0, \ K\Delta_{ij} > \Delta_t \\ 0 & \text{else}, \end{cases} \tag{2.2}$$

$$f(b_i, b_j)_{\forall j \in (5,6)} = \begin{cases} -K\Delta_{ij} & \Delta_{ij} < 0, \ -K\Delta_{ij} \geq -\Delta_t \\ -\Delta_t & \Delta_{ij} < 0, \ -K\Delta_{ij} < -\Delta_t \\ 0 & \text{else} \end{cases} \tag{2.3}$$

where Δ_{ij} represents the battery level gradient between agents A_i and A_j, $f(b_i, b_j)$ represents the proposed gradient based charging function with a scalar constant $K > 0$ dependent on the charging efficiency of the inductive coils subject to misalignments during charging and

Δ_t is the charge sharing threshold allowed per unit time. Following Fig. 2.1c, the current charge potential, c_{A_i} of agent A_i is therefore the sum of $f(b_i, b_j)$ for $j \in (1, 2, 5, 6)$:

$$c_{A_i} = c_5 + c_6 - c_1 - c_2 = \sum_{j \in (1,2,5,6)} f(b_i, b_j). \tag{2.4}$$

The proposed method allows agents to share energy in a group. Note that the charge sharing is one-directional; the net energy transfer is towards the front of the group supportive of keeping the convoy moving forward in formation. For simplicity and to maintain generality of our proposed method, each agent is assumed to be fully actuated and free to move in any direction.

Formation Setup

We define the hexagonal lattice formation by a $m - n$ notation with N agents each denoted as A_i, $i \in D$, where m denotes the number of agents on the front row and $n = m + 1$ denotes the number of agents on the second row from the front. This $m - n$ structure is repeated p number of times until all N hexagonal agents are placed in a hexagonal lattice structure as shown in Fig. 2.2. Therefore, $p = \frac{N}{m+n}$. For simplicity, we assume that m is always even and N is a multiple of $m + n$; i.e. p is $\mathbb{Z}_{>0}$.

Penguin Huddling-inspired Shuffling (PHS) Algorithm

Emperor penguins in a huddle lose more energy being exposed to the environment along the boundary and save energy by being at the center. Similarly, robotic agents along the boundary of a convoy use more energy monitoring the surroundings and being exposed to the environment, than robots at the center that remain protected and are able to turn off non-essential processes while following the leading agents. The battery usage with no charge sharing and no flank movement is illustrated in Fig. 2.2. We combine this assumption with our charge sharing scheme to present the need for the proposed PHS algorithm.

In Fig. 2.2, group 3 agents form the rear line of the convoy formation. Based on the proposed charge sharing scheme, the agents here are always providing charge to one or more
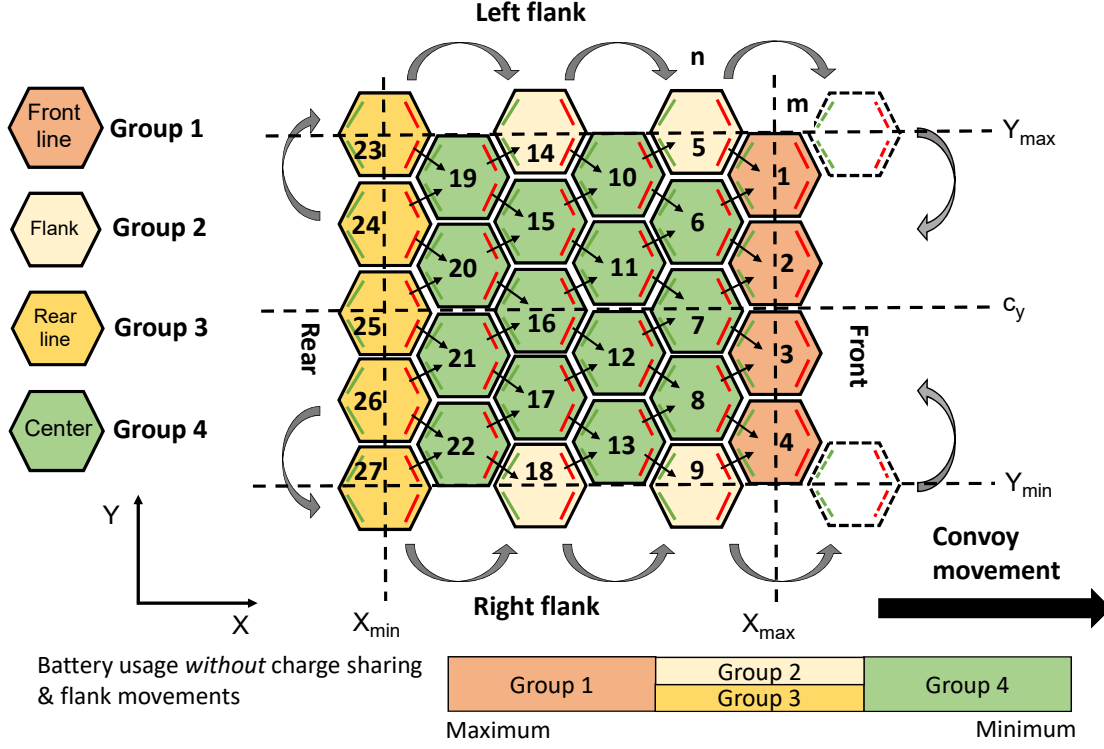
Figure 2.2. $m - n$=4-5 formation setup for $N = 27$ agents illustrating flank movement and charge sharing. Robot groups by varying battery usage within the formation without flank movement are also identified.

agents immediately in front. This is therefore the least favorable position in the convoy. Group 2 agents form the flanks of the convoy and share charge with two adjacent agents; one providing charge and the other taking charge. However, being at the boundary the agents keep up monitoring the surroundings. This position is therefore better than group 3 but still not the best place to be in the convoy. The agents in group 1 form the front line of the convoy and they are in charge of navigation (e.g. path planning, obstacle avoidance) tasks. They have to keep their on-board functionalities on at all times. Sensing mechanisms such as laser scanners, cameras [48] use a lot of power when used continuously. Such sensors along with movement actuation results in group 1 agents having the highest battery usage in the convoy. Agents in group 4 are in the most advantageous position being at the center surrounded by agents on all directions. They are able to share charge with their neighbors most effectively, and are protected from potentially harsh environmental conditions. They

Algorithm 1 Penguin Huddling-inspired Shuffling (PHS) algorithm

1: procedure Boundary Movement(X, Y, B) ▷ Position movements of agents given battery levels

2:     Input: Stacked agent configurations, x_i and y_i, and corresponding battery levels, b_i.

3:     Output: Updated coordinate position arrays X and Y, and battery level, B

4:     Determine centerline, $c_y \leftarrow \frac{\Sigma_{i=0}^{N} y_i}{N}$, $Y_{max}, Y_{min}, X_{max}, X_{min}$ of formation from X, Y

5:     for $i = 1 \to N$ do ▷ Find boundary agents

6:       if A_i lies on $Y_{max}||Y_{min}||X_{max}||X_{min}$ then

7:         Determine current charge potential, c_{A_i}, setting $c_1 = c_2 = c_3 = c_4 = 1$ ▷ Check Eq. (2.4)

8:         Determine charge potential at neighboring points, $n_{cp_j} = c_{A_i}$ for $i = j$, $\forall j \in (1, 2, .., 8)$

9:         Determine net charge gain at neighboring points, $n_{g_{i,j}} = c_{A_i} - n_{cp_j}$, $\forall j \in (1, 2, .., 8)$

10:         if $y_i \geq c_y$ then ▷ if A_i is on left half

11:           if $c_{A_i} \geq 0$ then ▷ A_i not on rear line

12:             Check positions $j = 4, 2, 7$ in order, for movement availability ▷ Refer to Fig. 2.1b

13:             if $n_{g_{i,j}} \geq 0$ then

14:               Move A_i to new position

15:           else ▷ A_i is on rear line

16:             Check positions $j = 7, 1, 3$ in order, for movement availability ▷ Refer to Fig. 2.1b

17:             if $n_{g_{i,j}} \geq 0$ && *new position* $\leq Y_{max}$ then

18:               Move A_i to new position

19:         else ▷ A_i is on right half

20:           if $c_{A_i} \geq 0$ then ▷ A_i not on rear line

21:             Check positions $j = 3, 1, 7$ in order, for movement availability ▷ Refer to Fig. 2.1b

22:             if $n_{g_{i,j}} \geq 0$ then

23:               if *new position* $== 3$ then

24:                 Hold until front line is full and then move A_i to new position

25:               else

26:                 Move A_i to new position

27:           else ▷ A_i is on rear line

28:             Check positions $j = 7, 2, 4$ in order, for movement availability ▷ Refer to Fig. 2.1b

29:             if $n_{g_{i,j}} \geq 0$ && new position $\geq Y_{min}$ then

30:               Move A_i to new position

31:       Update x_i, y_i, b_i

32:     return X, Y, B ▷ Return the new position coordinates and battery levels of the formation agents

34

can also turn off non-essential on-board tasks such as navigation, exploration, environment monitoring, etc. We will refer to this phenomenon as center advantage.

Even though huddles of Emperor penguins are inconsistent and change shape over time, for a robotic system, it is important to maintain a set formation for ease of control and proper functionality. If left freely to individual agents to try to move to the center directly their movements may become chaotic and inefficient. To maintain a set formation and allow agents to move to the center in turns in an organized way, the proposed one-directional charge sharing scheme creates a net power flow towards the front of the huddle. This creates an incentive for agents to try to move to the front first where they only receive charge from their neighbors. For simplicity, we assume the net movement of the entire formation is constrained to be along the x-axis only.

PHS described in Algorithm 1 systematically moves rear and flank agents to the front. The agents are attracted towards the center line c_y and hence they fill up the front line over time. The agents that were previously on the front line therefore now become center agents. As the flank agents move forward, space opens up for rear line agents to move along the flanks in turn. The previously center agents at the back therefore now become rear-line agents. This cyclic motion continues allowing all agents an equal opportunity for center advantage.

PHS is effective only if the energy saving while being at the center is more than or equal to the energy spent by an agent at the rear to move up the flank and get to the front and eventually the center; without which there is no incentive for an agent to follow Algorithm 1. This condition is formulated mathematically by:

$$
\begin{aligned}
\mu_b^{use} z &\leq \mu_{ca} \Delta t_c \\
&= \mu_b^{use}\left(2\left\lfloor\frac{n}{2}\right\rfloor + \frac{N}{m+n} + \frac{\left\lfloor\frac{n}{2}\right\rfloor + \frac{N}{m+n}}{\left\lfloor\frac{m+n}{2}\right\rfloor}\right) \\
&\leq \mu_{ca}\left(\left\lfloor\frac{n}{2}\right\rfloor + \frac{m}{2}\right)\left(\frac{N}{m+n} - 1\right)
\end{aligned}
\tag{2.5}
$$

where z denotes the total number of movements required by an agent in the worst case to get from the rear line to the front, μ_b^{use} denotes the battery usage for unit movement by an agent, μ_{ca} denotes the unit center advantage gained by an agent per unit time by being at

the center and Δt_c represents the time duration an agent is able to stay at the center from the front to the back as the formation progresses forward.

Therefore, the minimum center advantage, μ_{ca}^{min} required for agents to have an incentive to follow the proposed PHS algorithm and move to the center in turns can be written as:

$$\mu_{ca}^{min} = \frac{2\lfloor \frac{n}{2} \rfloor + \frac{N}{m+n} + \frac{\lfloor \frac{n}{2} \rfloor + \frac{N}{m+n}}{\lfloor \frac{m+n}{2} \rfloor}}{(\lfloor \frac{n}{2} \rfloor + \frac{m}{2})(\frac{N}{m+n} - 1)} \mu_b^{use}. \tag{2.6}$$

The required μ_{ca}^{min} decreases with increasing N for any arbitrary $m-n$ formation.

Stability Analysis of PHS algorithm

$$S(k) = \begin{cases} a_e = a_0 + (e-1)d & \text{where } a_0 = m+1, \\ & d = 2m+1, \, e \in (1,2,..,p) \\ \begin{cases} a_e = a_{p-u} + v & \text{where } v \in (1,2,..,\frac{m}{2}) \\ & e \in (\alpha p + 1, \alpha p + 2,..,\alpha p + \frac{m}{2}) \\ a_e = a_{p-u} - m + w & \text{where } w \in (0,1,2,..,\frac{m}{2}-1) \\ & e \in (\alpha p + \frac{m}{2} + 1, \alpha p + \frac{m}{2} + 2,..,\alpha p + m) \end{cases} & \forall u \in (0,1,..,p-1), \, \alpha \in (1,2,..,p) \end{cases}$$

$$\tag{2.7}$$

$$S(k+1) = \begin{cases} \begin{cases} a_1 = a(k)_{wq+1} \\ a_e = a(k)_{vw-u} & \text{for } u \in (0,1,2,..,w-1), \\ & \forall v \in (1,2,..,q), \, e \in (2,3,..,p(m+1)) \\ a_e = a(k)_{vw-u} & \text{for } u \in (0,1,2,..,w-1), \\ & \forall v \in (1,2,..,q), \, e \in (1,2,..,p(m+1)) \end{cases} & \text{when } mod(N,2) = 1, \, q = \frac{p(m+1)-1}{w} \\ & \text{when } mod(N,2) = 0, \, q = \frac{p(m+1)}{w} \end{cases}$$

$$\tag{2.8}$$

The $m-n$ formation with m always even, is symmetric about the center line c_y parallel to the x-axis. The left and right flank movements happen independent of each other but are symmetric and in sync following PHS. Therefore, the stability proof of the proposed PHS algorithm is shown for the left flank only as it holds true for the right flank as well.

We denote the indices of the agents A_i, $i \in D$ in the left half of the formation as G, i.e. $G \subset D$ with elements a_i. We represent agents in G as a sequence $S(k)$ dependent on the order at which they move from the initial state defined as z_0 at time step k. At z_0 the front row agents a_i, $i \in (1,2,..,\frac{m}{2})$ denoted as H, where $(H \subset G)$, receive charge from two rear

agents but do not have any agents in front to provide charge to. Following the proposed PHS algorithm, we consider one complete cycle of movement when at least one agent in H return to the front line receiving charge from two rear agents, with no one to provide charge to in front and no open space is left in the front row. Based on the sequence of movements from z_0, the boundary agents on the left flank come first in the sequence. They are followed by the rear line, and eventually the inner lines from the left-most to the middle in order. For the 4-5 formation with $N = 27$ in Fig. 2.2, the sequence $S(k)$ with $p(m+1)$ elements is written as:

$$S(k) = 5, 14, 23, 24, 25, 19, 20, 15, 16, 10, 11, 6, 7, 1, 2. \tag{2.9}$$

We denote this initial sequence at state z_0 as S_0. The sequence $S(k)$ can be built for a general case of $m - n$ formation with N agents and $p = \frac{N}{2m+1}$ as (2.7). After each cycle the sequence elements re-organize by (2.8) for $w = \frac{m}{2}$ following Algorithm 1. To investigate the stability of Algorithm 1, assuming that the sequence starts from S_0, we show that $S(k+s) = S(k)$ for some finite $s > 0$.

Referring to (2.8), the even N case shows a pattern where sets of w consecutive elements reverse order every cycle without overlap; i.e. at every even iteration, the cycle returns to the original sequence S_0. The general pattern of consecutive cycles of $S(k)$ for even N and the simplest case of $q = 1$ and arbitrary w can be written as:

$$a_i(k+1) = a_{w+1-i}(k) \qquad\qquad \forall i \in (1, 2, .., w). \tag{2.10}$$

The odd N case is similar to the even case of reversing sets of w consecutive elements without overlapping at each cycle. The difference is that, at each cycle the last element of $S(k)$ cycles to the front as element 1 in $S(k+1)$. Some key observations of this process include:

- At every order reversal of w consecutive elements without overlapping, element indexed $(\frac{w}{2}+1)$ in that set remains in its position; i.e. for $\beta \in (0, 1, 2, .., q-1)$,

$$a_{\beta w + \frac{w}{2}+1}(k+1) = a_{\beta w + \frac{w}{2}+1}(k). \tag{2.11}$$

- At every cycle, a_1 and every consecutive $(w+1)^{st}$ element move forward by w; i.e. for $\beta \in (0, 1, 2, .., q-1)$,

$$a_{\beta w+1}(k+\beta) \rightarrow a_{(\beta+1)w+1}(k+\beta+1)$$
$$a_{qw+1}(k+\beta) \rightarrow a_1(k+\beta+1). \tag{2.12}$$

We denote these segments of the sequence as F_1.

- Taking (2.12) into account, with every order reversal of w consecutive elements without overlapping, one can see that only elements indexed $i = 2$ through $i = w$ for every set of w essentially reverse their order on every cycle; i.e. for $\beta \in (0, 1, 2, .., q-1)$,

$$a_{\beta w+2}, a_{\beta w+3}, a_{\beta w+4}, ..., a_{\beta w+w}$$
$$\rightarrow a_{\beta w+w}, a_{\beta w+w-1}, ..., a_{\beta w+3}, a_{\beta w+2}. \tag{2.13}$$

Following the proof for the even N case, every even iteration of (2.13) results in these fragments of the sequence to return to the order in S_0. Following the pattern from (2.12), if every $(\gamma w + 1)^{st}$, $\gamma \in (0, 1, 2, .., q-1)$ element moves forward by w indices on every cycle and on reaching the $(qw+1)^{st}$ position cycles to index 1, these elements return to their original position after $q+1$ iterations. We denote these segments of the sequence as F_2.

Since F_1 returns to S_0 at every even iteration and F_2 returns to S_0 at every $q+1$ iteration, the number of cycles where both segments return to S_0 at the same time satisfies:

$$mod(\min_{\eta \in \{1,2\}} \eta(q+1), 2) = 0. \tag{2.14}$$

Therefore, $s = \eta(q+1)$ is the number of iterations needed for $S(k+s) = S_0$ for an odd N.

For any even $m > 0$, $w = \frac{m}{2}$. For $p = 1$, the total number of agents, $N = 2m+1$ is always odd. Using (2.8), we get $q = 2$. The formation converges back to the original state z_0 after $s = 6$ cycles for $\eta = 2$.

For $p = g$, where g is arbitrary, the total number of agents $N = g(2m+1)$ is either odd (for odd g) or even (for even g). Using (2.8), we get $q = \begin{cases} \frac{2(g(m+1)-1)}{m} & \text{odd } N \\ \frac{2g(m+1)}{m} & \text{even } N \end{cases}$. For either case, q can be odd or even. Therefore, regardless of N being odd or even, the formation converges back to the original state z_0 after s cycles for the $p = g$ case depending on η.

For $p = g+1$, the total number of agents, $N = (g+1)(2m+1) = 2mg+g+2m+1$ is either odd(for even g) or even(for odd g). Using (2.8), we get $q = \begin{cases} \frac{2((g+1)(m+1)-1)}{m} & \text{odd } N \\ \frac{2(g+1)(m+1)}{m} & \text{even } N \end{cases}$. For either case, q can be odd or even. Therefore, regardless of N being odd or even, the formation converges back to the original state z_0 after s cycles for the $p = g+1$ case depending on η.

Therefore, the PHS algorithm is stable for any N as it cycles agents and holds the original formation for any case of valid m, where $m > 0$, $mod(m, 2) = 0$ and p, where $p = \mathbb{Z}_{>0}$ as proved by induction.

PHS Algorithm Simulation

Fig. 2.3 shows the sequence of unit time step position shuffling movements by agents in a 2-3 formation of $N = 10$ following Algorithm 1. After a finite number of steps, the formation returns to the initial configuration. Each agent is equipped with four induction coils; green denote receiving of charge, red denote providing of charge and inactive coils are shown in black. Agents in the most favorable positions in the convoy are marked green.

2.3.2 Validation

To validate the proposed concepts, we consider a group of N robots in the $m-n$ formation deployed on a 2-D terrain with no obstacles; starts at an initial position A and travels along the x-axis towards B. We assume that all agents are in ideal communication with one another and are capable of making precision movements.

The convoy moves forward from point A towards point B at velocity v. The agents in the convoy are designed to be structurally identical (hexagonal) but have different roles or assigned tasks; as a result, their battery usage varies significantly per unit time. The general
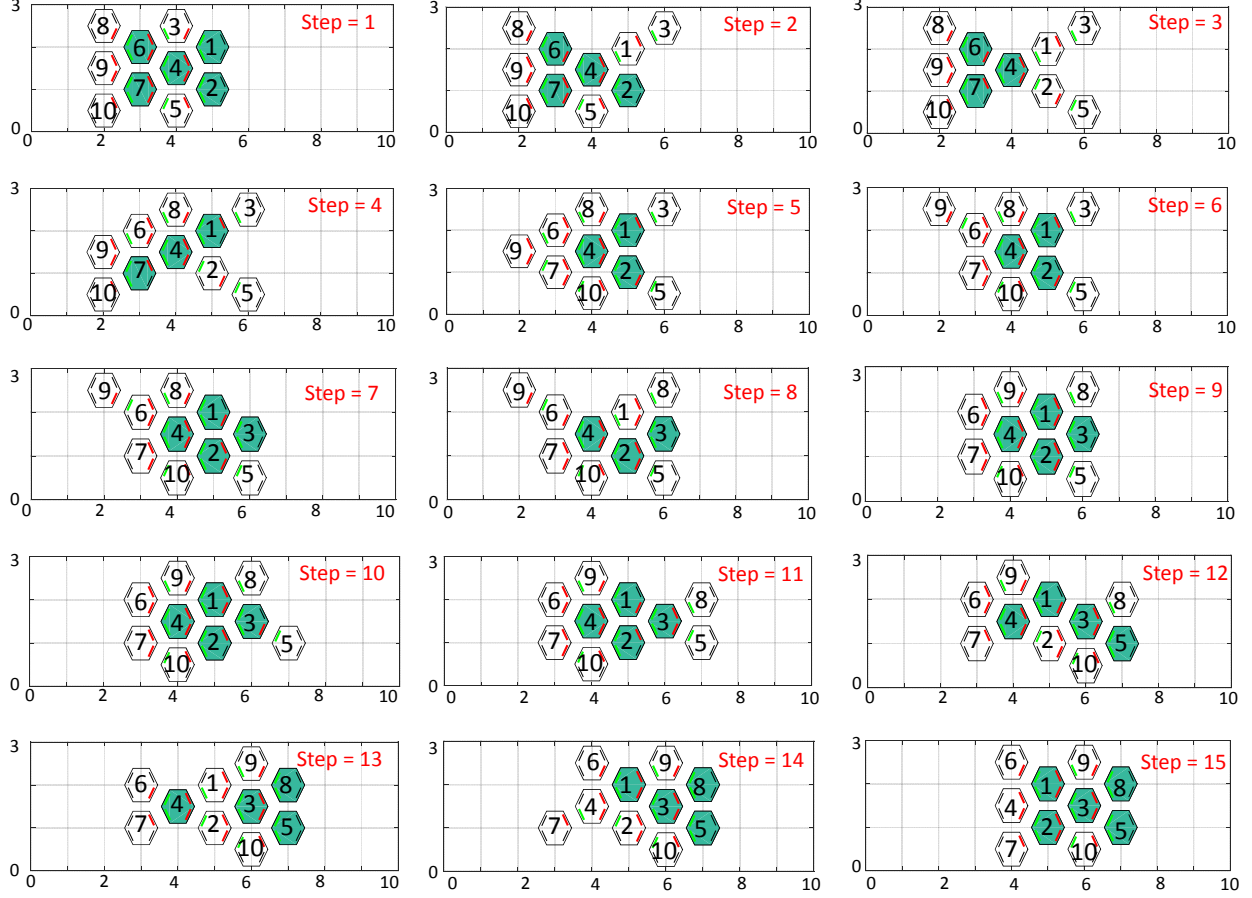
Figure 2.3. Simulation steps showing position shuffling progression and convergence back to original configuration for a $2-3$ formation with $N = 10$. Agents capable of receiving charge from both rear coils are identified as green.

battery usage (movement, specific tasks) is modeled per unit time as $b_{use} \sim \mathcal{N}(\mu_b^{use}, \sigma_{use}^2)$. The additional battery usage by group 1 robots per unit time using specialized navigation sensors such as LIDAR, camera etc. is modeled as $b_{ad} \sim \mathcal{N}(\mu_b^{ad}, \sigma_{ad}^2)$. The power consumption due to the charge sharing mechanism itself is assumed to be negligible compared to b_{use} based on [49]. Referring to Fig. 2.2, the battery usage of agent A_i, $\forall i \in D$ without charge sharing is therefore modeled as:

$$b_i = \begin{cases} b_i - b_{use} - b_{ad} & A_i \in \text{Group 1} \\ b_i - b_{use} & A_i \in \text{Group 2 \& 3} \\ b_i - b_{use} + \mu_{ca} & A_i \in \text{Group 4}. \end{cases} \tag{2.15}$$

40

Table 2.1. Validation Scenarios for Cyclic Energy Sharing

Scenario	Forward movement	Center advantage	Gradient based charge sharing	Position shuffling
S1	✓			
S2	✓	✓		
S3	✓	✓		✓
S4	✓		✓	✓
S5	✓	✓	✓	✓

Table 2.2. Validation Parameters for Cyclic Energy Sharing

Forward velocity, v	2 x-units/time
Battery usage for movement, charge sharing mechanism (groups 1, 2, 3, 4), b_{use}	$(\mu_b^{use}, \sigma_{use}^2)$ (0.5 units/time, 0.5)
Additional battery usage for navigational task (group 1), b_{ad}	$(\mu_b^{ad}, \sigma_{ad}^2)$ (0.3 units/time, 0.1)
Charge sharing threshold, $\lvert \Delta_t \rvert$	0.2 units/time

The simulation is set up with five different scenarios, where the effectiveness of each of the proposed methods is presented individually and as combinations. At the initial state z_0, all agents start with individual batteries at 100%. In S1, the agents only move forward as a group to represent the base scenario as control. In S2, the agents are allowed the minimum center advantage. In S3, the agents are allowed PHS so that all agents get an opportunity for center advantage. In S4, PHS is allowed with gradient based charge sharing but without center advantage to compare the effect these two concepts have on the convoy performance. Finally, S5 utilizes all proposed concepts in this chapter adopted from the huddling behavior of Emperor penguins. With this setup, the proposed concepts can be validated if the convoy travels the furthest distance in S5 compared to the other scenarios. The scenarios are summarized in Table 2.1.

The simulation parameters are exaggerated for brevity of the simulations and are listed in Table 2.2. We set $\mu_{ca} = \mu_{ca}^{min}$ for all cases. Since the aim of the study is to extend the working life of the convoy as a whole, the simulation stops when the battery life of any agent falls below 5%. The x-distance travelled by the convoy center and the battery level variance amongst agents at the end are measured.

(a) 4-5 formation, $N=54$

(b) 6-7 formation, $N=78$

(c) 10-11 formation, $N=126$

(d) 12-13 formation, $N=200$
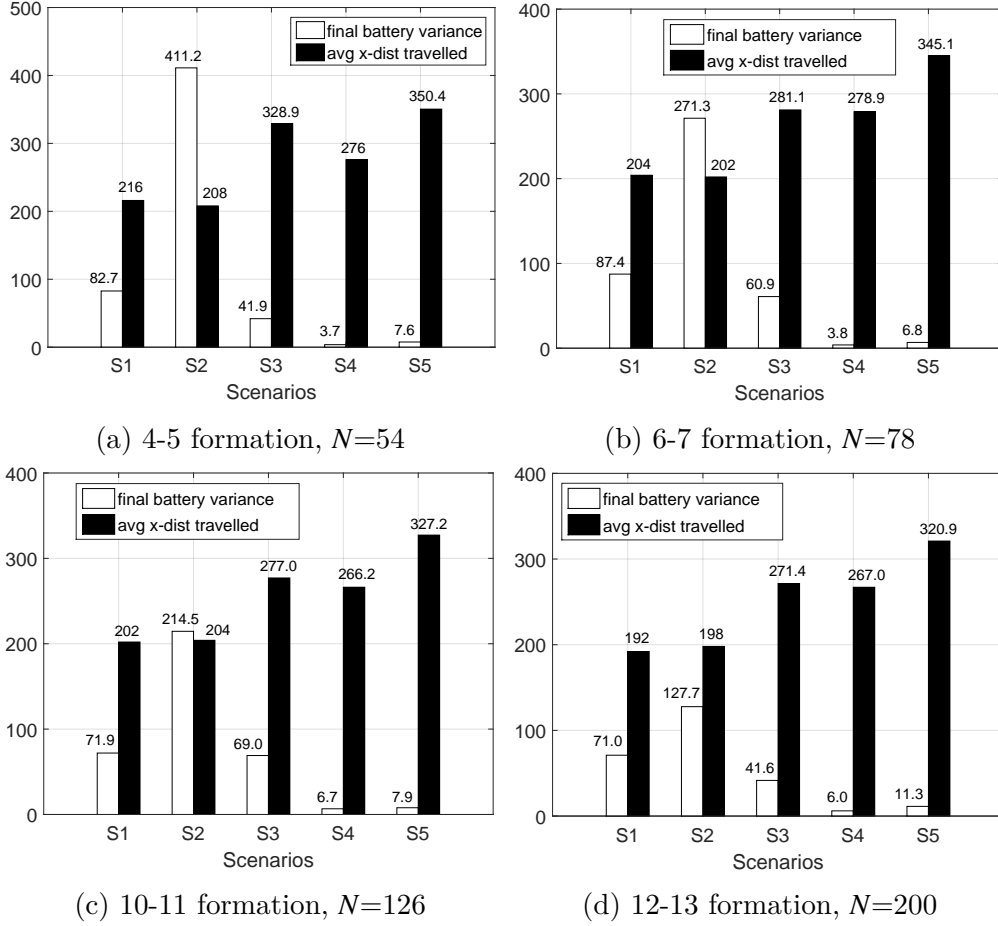
Figure 2.4. Simulation results showing the final battery level variance and x-distance traveled by convoys under five different scenarios. The results presented are averages of 10 simulation runs. S5 yielded the maximum x-distance with the lowest final battery level variance in all setups.

Results and Discussion

A 4-5 formation of $N = 54$ robots was considered for the first set of simulations with calculated $\mu_{ca}^{min} = 0.3$. The average results from 10 independent runs for each of the scenarios are tabulated in Fig. 2.4a. The x-distance traveled by the convoy in S1 and S2 was approximately equal. This is because even though S2 allowed center advantage, the convoy was still as strong as the boundary agents who remained in place without any such advantage. With agents in the center saving energy, the final battery variance in S2 was significantly higher.

S1 and S4 did not allow any center advantage. The x-distance values obtained for S4 were close to S1 and S2 but consistently higher by a margin for all individual simulation runs.

(a) 4-5 formation   (b) 6-7 formation

(c) 10-11 formation   (d) 12-13 formation
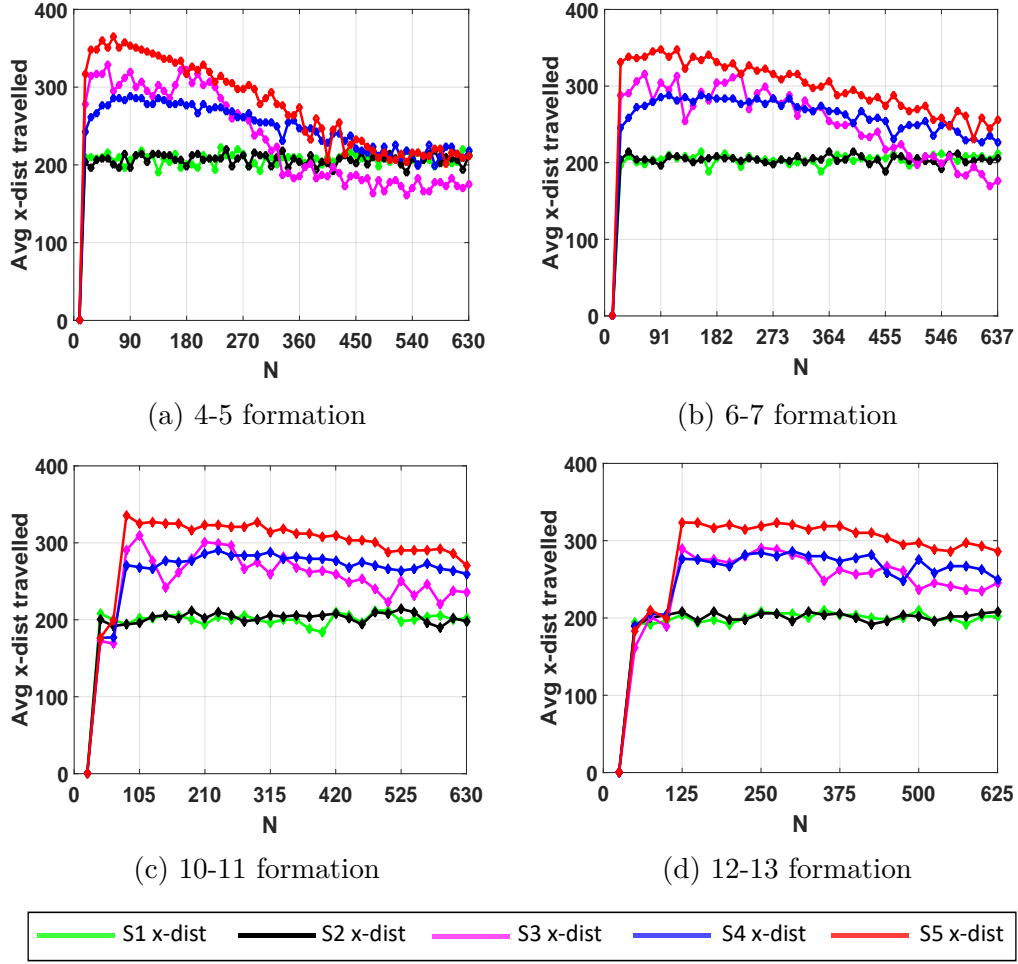
Figure 2.5. Scenario performance comparison for $m-n$ formation with varying N. S5 allows maximum x-distance traveled for all simulated formation cases over a wide range of N values.

This observation closely relates to the final battery level variance readings for S1, S2 and S4. S4 has the lowest final battery level variance because the gradient based charge sharing method evened differences in battery levels of neighboring agents. This allowed agents using more battery to survive longer by receiving energy from its neighbors.

S3 allowed position shuffling along with S2 methods and so all robots got an equal opportunity to move to the center of the convoy in turns for center advantage. The convoy was no longer as strong as the boundary agents only and so the x-distance traveled in S3 was consistently higher than S1, S2 and S4. The final battery level variance between agents is

also significantly lower than S2 but much higher than S4 without the gradient based charge sharing method.

S5 allowed the convoy to travel the maximum x-distance consistently with a low final battery level variance for all simulation runs. The combined effects of center advantage, PHS and the gradient based charge sharing methods allowed the convoy to survive longer in the field using the full potential of the group as validated by the simulation results.

Simulations were repeated for cases of 6-7, 10-11 and 12-13 formations with $N = 78$, 126 and 200 robots, calculated μ_{ca}^{min} of 0.225, 0.171 and 0.126 respectively. The results are shown in Fig. 2.4b-2.4d. For bigger convoys, the final battery level variance decreased for S2 as expected given the large sample size for all cases. The effect of center advantage was dominant over gradient based charge sharing with PHS (S3 vs S4) for smaller groups as shown by the much higher x-distance values obtained in the 4-5 formation with $N = 54$. The effect quickly deteriorates with bigger groups as shown for larger formation and N cases. However, the overall conclusion remained the same. S5 with all the proposed concepts combined, consistently yielded the best results in terms of maximum x-distance traveled while keeping a low variance in battery levels of agents by a wide margin.

To verify that these conclusions hold over a range of N, the simulations were repeated with varying N and corresponding μ_{ca}^{min} for all the formation cases. The 4-5, 6-7, 10-11 and 12-13 formation x-distance travelled for varying N are plotted in Fig. 2.5a-2.5d. In each case the average x-distance travelled over 10 independent sets of simulations for each value of N are used. For all $m - n$ setups, S1 and S2 consistently yielded similar x-distances over the entire range of N as expected. S3 provided better results than S4 for smaller $m - n$ formations with low N. For larger values of N, the x-distance traveled with S3 become increasingly worse. This is because the calculated μ_{ca}^{min} does not take σ_{use}^2 into account. Since for larger N, the agents have to move much longer distances to get to the front, the effects of the high σ_{use}^2 add up and the center advantage is unable to match this significant quantity of extra energy spent by any agent to get to the center. Similarly in S4, the gradient based charge sharing alone is unable to counter this effect and its performance deteriorates with increasing N as well. The performance of S5 deteriorates with larger N for the same reason but with center advantage and the gradient based charge sharing scheme working

together it is able to counter the effects of the high σ^2_{use} for much larger N values than S3 or S4. Therefore, S5 shows much higher x-distances traveled by the convoy over a larger range of N compared to the other scenarios. The performance deterioration is higher in smaller formations such as the $4-5$ case where S5's performance becomes the same as S1 and S2 for $N > 500$. Therefore, we conclude that the width of the convoy $(m-n)$ should be increased with increasing N for better performance.

We conclude the topic of cyclic energy sharing in structured multi-robot systems here with favorable simulation results validating that formations of different sizes successfully survive longer as a group with the proposed concept compared to the base case of individuals only relying on themselves. The next section of this chapter is aimed at energy sharing and distribution in an unstructured robot group spread out over a large area.

2.4 Adaptive Self-organization in Unstructured Groups for Efficient Energy Distribution

In this section, we propose an artificial potential based, efficient and generalized approach to energy distribution in a multi-agent system with optimal distribution of higher energy bearing agents throughout the group with adaptive inter-agent spacing (AIS) control, dependent on individual energy levels for fast energy distribution and group energy equilibrium attainment. The adaptive inter-agent spacing control consequently prevents over-crowding of low energy bearing agents on high energy bearing agents maximizing the usage of individual energy transfer capabilities on minimal number of neighbors at a time within a specified radius for optimal performance.

2.4.1 Preliminaries

Robot Group Dynamics and Setup

We consider N fully actuated mobile agents with dynamics of the form:

$$\dot{r}_i = v_i \text{ and } \dot{v}_i = u_i \qquad\qquad i \in \{1,2,..,N\} \qquad (2.16)$$

in which $r_i \in \mathbb{R}^p$, $v_i \in \mathbb{R}^p$ and $u_i \in \mathbb{R}^p$ denote the position, velocity and control input of each robot i respectively. We denote the on-board energy level on each agent to be distributed as $0 < b_i \leq 100$, $i \in \{1, 2, .., N\}$. Maintaining generality, we assume that each agent is able to transmit/receive energy b to/from other agents within a specified radius r_b, at a rate dependent on the number of agents within r_b due to space and bandwidth limitations. We model generalized energy sharing for the purposes of this work as:

$$\delta b_i = \beta \frac{\sum \Delta b_{ij}}{n} \qquad\qquad i, j \in (\{1, 2, .., N\} | r_{ij} \leq r_b) \qquad (2.17)$$

where β is a scalar control gain, $\Delta b_{ij} = b_j - b_i$ is the difference in energy level between agents i and j, and n represents the number of agents around agent i within radius r_b. energy sharing only occurs when $\Delta b_{ij} > 0$.

We denote the mean energy level of the group of N agents as b_m. At any given time, agent $i \in (\{A, B\} \ni A \cup B = \Lambda, \ A \cap B = \emptyset)$, where A is defined as the set of agents with $b_i > b_m$, and B as the set of agents with $b_i \leq b_m$.

2.4.2 Methodology

Adaptive Inter-agent Spacing (AIS) Control Law

For efficient energy distribution in a group of N mobile agents governed by the dynamics model in (2.16), we base our proposed control law on the previously established multiple heterogeneous units segregation solution put forward in [50]:

$$u_i = -\sum_{j \neq i} \nabla_{r_i} U_{ij}(||r_{ij}||) - \sum_{j \neq i} (v_i - v_j) \qquad (2.18)$$

where $U_{ij}(||r_{ij}||)$ is an artificial potential function defining the interaction between agents $i, j \in \{1, 2, .., N\}$, $||r_{ij}||$ is the Euclidean norm of the vector $r_{ij} = r_i - r_j$, and ∇_{r_i} is the gradient with respect to the coordinates of agent i. The first term represents the resultant force acting on agent i due to interactions with all other agents in the system. The second term acts as a velocity damping force such that agents match their velocities to counter large variations in potential differences among agents causing chaotic movements and maintain system stability.
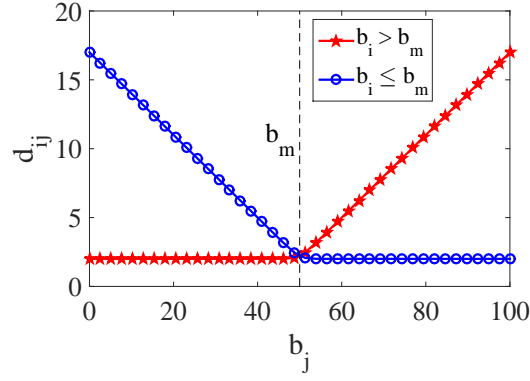
(a) Inter-agent spacing function plot for agent i based on neighbor j energy level. Inter-agent spacing is dictated by the group mean energy level b_m.
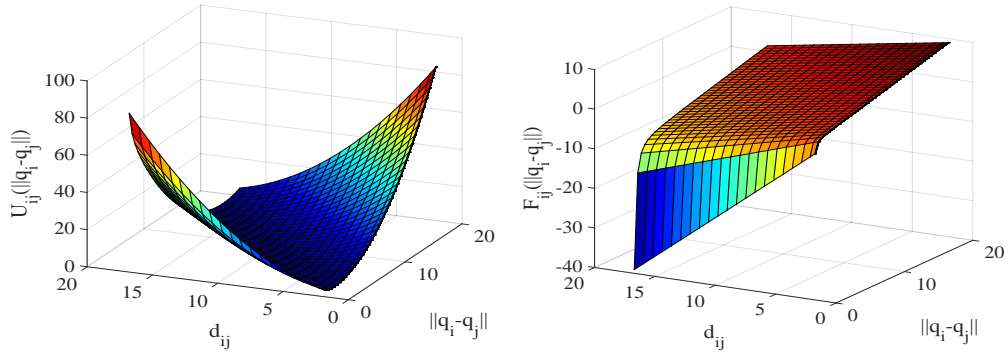
(b) Potential function plot based on inter-agent distance with $b_m = 50$.

(c) Scalar force plot based on inter-agent distance with $b_m = 50$.

Figure 2.6. Proposed artificial potential function and corresponding scalar force plot against agent inter-distance and proposed inter-agent spacing function d.

The artificial potential field U_{ij} is defined as a function of current and target relative distances between a pair of agents, expressed as:

$$U_{ij}(||r_{ij}||) = \alpha(\frac{1}{2}(||r_{ij}|| - d_{ij})^2 + \ln||r_{ij}|| + \frac{d_{ij}}{||r_{ij}||}) \tag{2.19}$$

in which α is a scalar control gain, and d_{ij} is a positive inter-agent target distance parameter described as a function of b_j, and b_m later in the chapter. We assume that at the initial time instant $||r_{ij}|| \neq 0$, for which (2.19) is undefined; i.e. agents i, j do not collide.

47

AIS for Efficient Energy Distribution

For efficient distribution of energy b, we design the inter-agent target distance parameter d_{ij} as a continuous function based on individual agent energy levels with the following properties:

- At system equilibrium, all agents converge to the mean energy level b_m and maintain the equilibrium inter-distance d_e.

- Agents in A must maintain inter-distances proportional to the other's energy level, such that the higher the amount of energy to be distributed by the pair for equilibrium, the higher the number of agents from B can occupy the created in-between space to receive the distributed energy.

- Agents in B must maintain inter-distances inversely proportional to the other's energy level, such that the higher the amount of energy required by the pair for equilibrium, the higher the number of agents from A can occupy the created in-between space to distribute their energy.

We propose the following continuous function for d_{ij}, for:

- agents in A interacting with agents in $\Lambda \setminus A$

- agents in B interacting with agents in $\Lambda \setminus B$

derived from a smoothed approximation of the rectified linear unit (ReLU) activation function, satisfying the above set requirements:

$$d_{ij} = \begin{cases} \rho \, \ln(1 + e^{b_j - b_m}) + d_e & \text{if } i \in A, \, j \in \Lambda \\ \rho \, \ln(1 + e^{b_m - b_j}) + d_e & \text{if } i \in B, \, j \in \Lambda \end{cases} \tag{2.20}$$

where ρ is a scalar control gain. Figure 2.6 illustrates the distance relationship between agents for the two cases.

The significance of the proposed function for d_{ij} is that it ensures that agents with large on-board energy for distribution, spread out throughout the group without accumulating

48

together. This is particularly important for efficient energy distribution in systems where the initial energy distribution is skewed on certain areas of the group.

Furthermore, the design of the spacing between agents with lower energy ensure that no agent with energy level larger than the mean is over-crowded with agents with lower energy level agents at any given time. This allows fast and efficient energy transfer between agents within r_b when transfer limits are present dependent on number of connecting agents.

AIS Controller Analysis

To investigate the stability and the convergence of the multi-agent system to equilibrium distance d_e using the proposed control law, we define the Lyapunov function as,

$$V(q,v) = U(q) + \frac{1}{2}v^{\mathrm{T}}v \tag{2.21}$$

where $q \in \mathbb{R}^{Np}$ and $v \in \mathbb{R}^{Np}$ are stacked position and velocity vectors of N robots in the system, and $U(q) : \mathbb{R}^{Np} \longrightarrow \mathbb{R}_{>0}$ is the collective potential energy of the system written as,

$$U(q) = \frac{1}{2}\sum_{i \in A}\sum_{j \neq i}U_{ij}(||q_{ij}||) + \frac{1}{2}\sum_{i \in B}\sum_{j \neq i}U_{ij}(||q_{ij}||). \tag{2.22}$$

where the first term represents the total potential for pairs of agents $i \in A$, $j \in \Lambda$ and the second term for pairs of agents in $i \in B$, $j \in \Lambda$. The collective dynamics of the system is written as,

$$\dot{q} = v \tag{2.23}$$

$$\dot{v} = -\nabla U(q) - \hat{L}(q)v \tag{2.24}$$

where $\hat{L}(q)$ is the Kronecker product of the fully connected system's graph Laplacian $L(q)$ and a $p \times p$ identity matrix I_p.

Proposition: Assuming a complete underlying adjacency graph at all times, for any initial condition that belongs to the level set $\Omega_C = \{(q,v)|V(q,v) \leq C\}$, for $C > 0$, a multi-agent system with agents in sets A or B, and dynamics, energy sharing and control defined

49

by (2.16), (2.17) and (2.18) respectively, asymptotically converges to the largest invariant set in $\Omega_I = \{(q,v) \in \Omega_C | \dot{V}(q) = 0\}$ without any inter-agent collision. At the largest invariant set in Ω_I, the velocity of each agent is bounded, all velocities match and the system's collective potential reaches a local minimum.

Proof: For proof of the proposition defined above, we refer to [50], where LaSalle's Invariance Principle is applied to show convergence, by demonstrating that $\dot{V}(q,v) \leq 0$, substituting the collective dynamics equations (2.23), (2.24). By design, the potential field and collective dynamics defined for the proposed AIS control law in this research is identical to the multi-robot segregation model put forward in [50]. Therefore, for proof of convergence we refer to [50] where the authors show that the velocity of each agent is bounded, and the system reaches a local minima at energy equilibrium ($d_{ij} = d_e$, $\forall i,j$) with no change in velocities. Collision avoidance is also proved assuming no collision occurs at initialization.

2.4.3 Supplement for Large Swarms using AIS

The AIS based energy distribution method is designed to produce fast individual energy convergence to the group energy mean by spacing high energy robots throughout the group. It must be noted that the AIS controller requires high energy robots to travel at high speeds over large distances avoiding collision with other robots to reach their spaced distances with other high energy robots, which may be impractical in real life situations.

In reality, robotic agents are limited by their mobility. Maximum speed limitations may prevent high energy bearing agents from initially distributing themselves throughout the group, and continuously narrowing pathways may prevent further self-organization. The problem incrementally worsens for larger robot swarms spread out over larger areas, where more robots have to travel increasingly larger distances to re-distribute themselves with narrowing passageways.

The huddling behavior of Emperor Penguins in the Antarctic presented in Section 1.1 is a dynamic process, where observations suggest that huddles merge and split over time. Current understanding of merging and splitting of huddles is limited to having a correlation with ambient temperature that dictates penguin density in individual huddles [37]. However,

observations of this phenomenon reveal that the continuous process of merging and splitting of huddles create pathways for penguins to relocate to other huddles in the colony.

Clustering and Sequential Merging Algorithm for Large Swarms

Inspired by this continuous multi-huddle merging/splitting process where Penguins may number in thousands, we propose an initial clustering method of all agents and a sequential merging process of adjacent clusters each utilizing AIS locally, to eventually merge all clusters into one. The clustering and merging process for large swarms is described as follows.

Large Swarm Clustering/Merging for AIS:

- Step 1: Determine k tanker agents as 90th percentile of the initial energy distribution.

- Step 2: Perform $k-means$ clustering of the initial agent distribution.

- Step 3: Assign k tanker agents to the k cluster centroids, such that the total distance travelled by all tankers is minimized.

- Step 4: k tanker agents move to the k cluster centroids avoiding collision with other agents.

- Step 5: Run AIS controller for energy distribution locally within each cluster to reach local cluster equilibrium.

- Step 6: Merge with adjacent neighboring cluster if both clusters have reached their local energy equilibrium.

- Step 7: Repeat process from Steps 5 until all clusters are merged as one.

In order to ensure that the highest energy bearing agents of the group are distributed throughout the group, we determine the 90th percentile of sorted agent energy levels, where the number of agents is denoted as k and the agents are termed as tankers. We denote the initial positions of the k tanker agents as vector A.

The agent swarm is divided into k clusters by $k-means$ clustering. The clustering problem is formulated as follows where the objective is to find,

$$\underset{S}{\arg\min} \; \sum_{i=1}^{k} \sum_{r \in S_i} ||r - \mu_i||^2 = \underset{S}{\arg\min} \; \sum_{i=1}^{k} \frac{1}{2|S_i|} \sum_{r_m, r_n \in S_i} ||r_m - r_n||^2 \tag{2.25}$$

where r denotes the vector of N agent positions, $S = \{S_1, S_2, .., S_k\}$ denotes the k partitioned sets of agents such that $k \leq N$, and μ_i is the mean of agent positions in S_i [51]. The $k-means$ clustering method is a well-established partitioning algorithm based on a squared error criterion with a complexity of $\mathcal{O}(k)$ [52]. The centroid positions of each of the k clusters is denoted as vector B. Each tanker robot is assigned to move to one of the centroid locations, such that the total distance travelled by the k tankers is minimized. The optimization problem is formulated as,

$$P^* = \underset{P}{\arg\min} \; ||A - PB||_2 \tag{2.26}$$

$$B^* = P^* B \tag{2.27}$$

where P is a permutation matrix generated using Heap's algorithm [53]. B^* denotes the sequence of cluster centroid positions corresponding to the sequence of tanker positions in A such that the total distance is minimized. The complexity of the optimization formulation is $k!$ and therefore computationally heavy for large k. Since optimization is not the focus of our study, we continue our formulation with this brute force approach. A number of relatively efficient methods including the Hungarian algorithm [54] may be used to solve this problem. A brief review of applicable methods is presented in [55].

The tanker agents relocate to their assigned cluster locations avoiding collision with other agents. Once the tanker agents are in place, the local clusters use the proposed AIS controller to attain their respective local mean energy level equilibriums. Once adjacent clusters reach their equilibrium, they merge together sequentially and the process continues with each merged cluster attaining their local energy mean equilibrium following the proposed AIS controller. The continuous sequential merging process eventually joins all clusters together into one and the global energy mean equilibrium is reached.

2.4.4 Validation

To validate our proposed concept, we show that a group of agents randomly distributed on a flat planar surface each having a different energy level $0 < b_i \leq 100$, successfully converge to the mean group energy level b_m faster with AIS than without. We define the base case for our comparison as, all agents rendezvous with agent inter-distance d_e and share energy with all neighbors within r_b. With such a setup, where all aspects of the experiment are held constant except for the proposed d_{ij} function, we isolate the effectiveness of the proposed AIS control law on system performance. First, the proposed clustering and sequential merging method specifically for large swarms with a maximum speed restriction of $v_m = 1$ is validated by time lapse illustrations of the initial clustering, tanker allocation, local AIS implementation and sequential merging of said clusters to eventually reach the global energy mean. Notable observations of the simulation are presented along with their effectiveness on the agent self-organization and energy distribution process. Scalability results are also presented for increasing N.

Finally, an in-depth validation and effectiveness analysis of the proposed AIS controller for general implementation is then presented in the following section without any maximum velocity restrictions focusing specifically on the agent self-organizing process. The validation process is set up with four specific scenarios to study the performance and effectiveness of our proposed energy distribution method in comparison to the defined base method. The scenarios include N randomly distributed agents on the $x-y$ plane initially having:

- Scenario 1 (S1): Skewed

- Scenario 2 (S2): Bi-modal

- Scenario 3 (S3): Normal

- Scenario 4 (S4): Random

distributed energy levels on agents along the planar x-axis, each being compared to its corresponding base approach solution. The left-skewed initial distribution is designed such that all agents on the right one-quarter of the x-y plane have $80 \leq b \leq 100$, while all others

have $0 < b \leq 20$. The bi-modal initial distribution is designed such that all agents on the left one-quarter and right one-quarter of the x-y plane have $80 \leq b \leq 100$ and while all others have $0 < b \leq 20$. The normal initial distribution is designed such that all agents on the middle one-quarter of the x-y plane have $80 \leq b \leq 100$, while all others have $0 < b \leq 20$. Lastly, the random initial distribution allows all agents in the x-y plane to have a random energy level $5 < b \leq 100$.

Each set of experiments consisted of $N = 100$ robots, each with zero initial velocity, with exaggerated parameters $d_e = 2$, $r_b = 3$, $\alpha = 0.8$, $\beta = 0.1$ and $\rho = 0.8$ for brevity of the simulations.

Clustering and Sequential Merging Implementation for Large Swarms

We present the validation results of the proposed supplementary clustering and sequential merging process utilizing local AIS control for energy distribution with time lapse images of the process with $N = 50$ and $N = 100$ agents shown in Fig. 2.7. The respective sequential global energy equilibrium attainment process with time is plotted in Fig. 2.8.

For $N = 50$, the 90th percentile tanker robot determination yielded 5 tanker robots resulting in 5 k-means initial clusters to form. The tanker robots were allocated to their respective cluster centroids minimizing the required total distance to be travelled. The tanker robots successfully navigated to the cluster centroids avoiding collision with neighboring robots. Once the cluster centroids were reached, each cluster initiated their local AIS controller to locally share and distribute their energy centered by their tanker agent. As adjacent clusters reached their local equilibrium, sequential merging allowed clusters to join and eventually reach the global energy mean as a single group. We emphasize here that compared to the AIS controller applied to the entire group as a whole, the clustering method allows agents to travel shorter distances within their clusters. The corresponding agent energy level plot for $N = 50$ agents shows the sequential local equilibrium attainment process for each cluster. After the initial clustering process, each cluster reaches an equilibrium where the cluster-to-cluster energy level variance is observed to be small. Similar observations are noted for the $N = 100$ agent simulation initially producing 10 tankers and 10 k-means clusters. Sequential
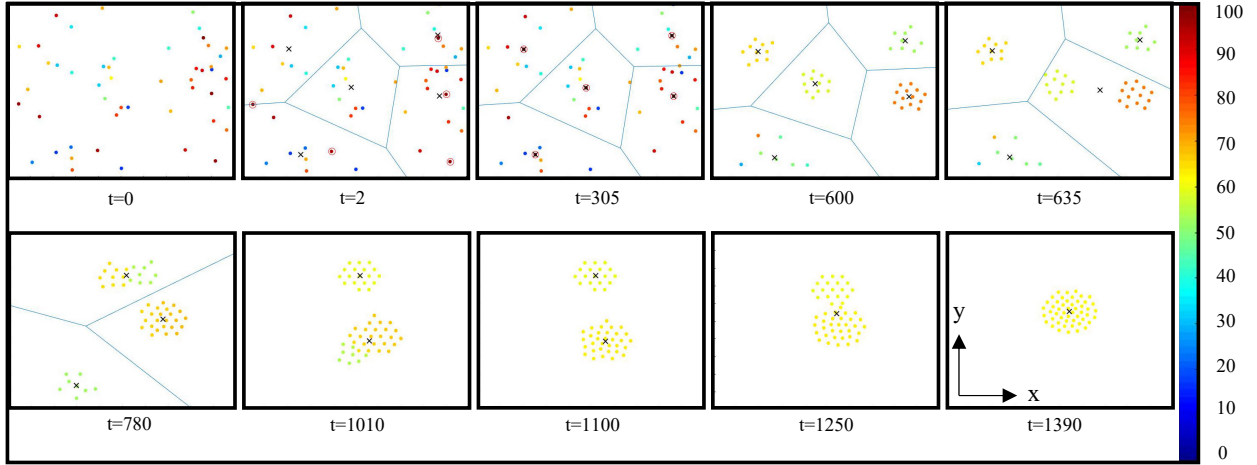
(a) Clustering and merging for $N = 50$ agents using local AIS to reach global energy equilibrium.
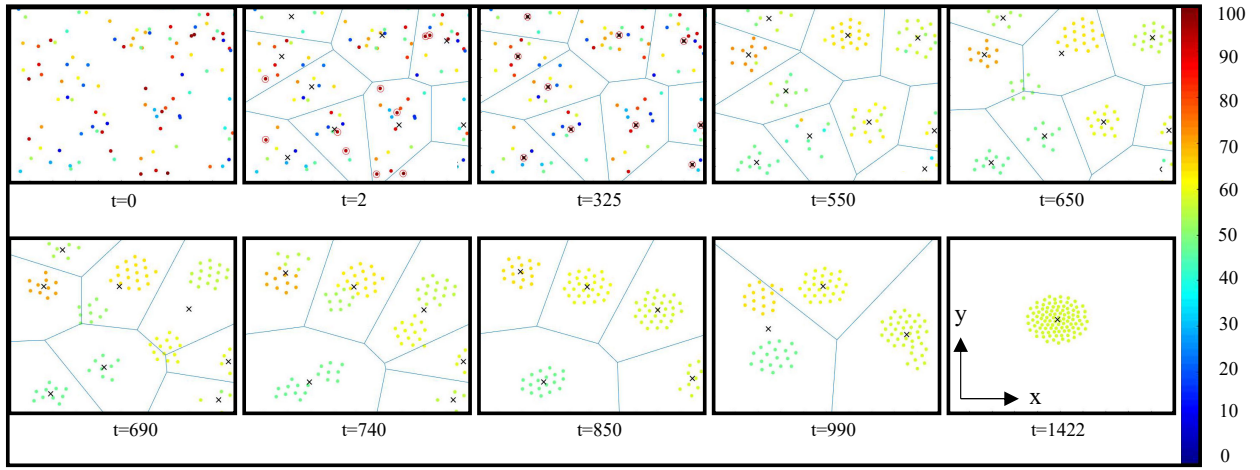
(b) Clustering and merging for $N = 100$ agents using local AIS to reach global energy equilibrium.

Figure 2.7. Proposed clustering and sequential merging with local AIS implementation for energy distribution with $N = 50$ and $N = 100$ agents to reach global mean energy equilibrium.

merging eventually resulted in global energy mean equilibrium attainment under $1,500$ time steps.

We note here that low variance in inter-agent energy levels obtained by the clustering and sequential merging of small groups is desirable using AIS, since inter-agent spacing following the AIS controller is dependent on differences in energy levels. With a smaller variance, sets of high energy bearing agents and sets of low energy bearing agents are not required to space themselves far apart moving faster than other group members avoiding collision with narrowing passageways. Therefore, the clustering method allowed reduced inter-agent

(a) $N = 50$ (b) $N = 100$
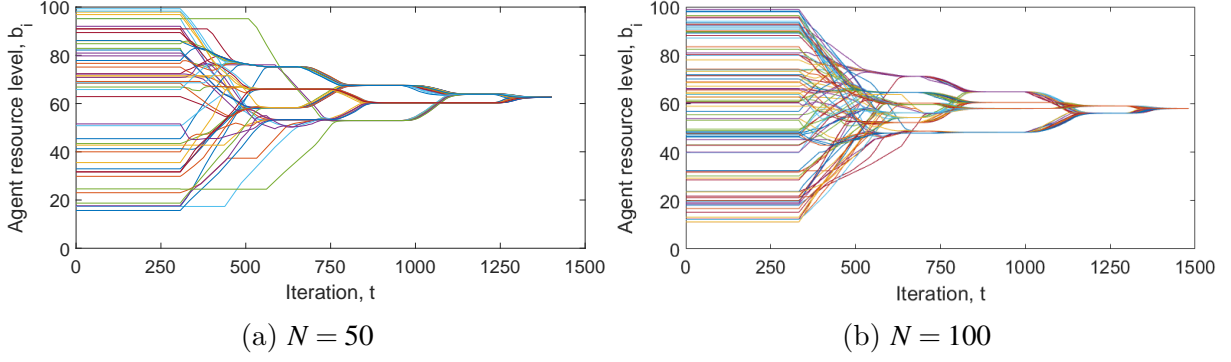
Figure 2.8. Random initial energy distribution - individual agent energy level convergence vs. iteration time with clustering and merging using AIS.
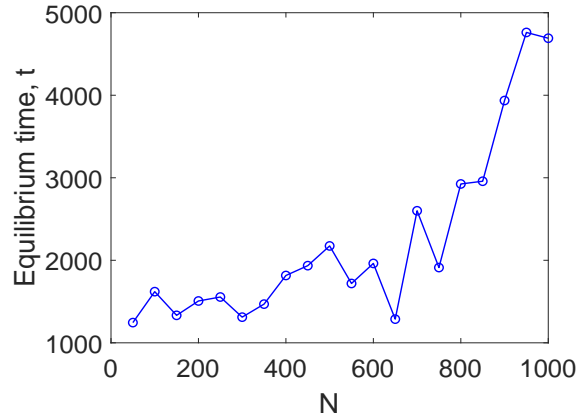
Figure 2.9. Scalability analysis of the clustering and sequential merging process showing increasing iteration time to reach global energy mean equilibrium for increasing N with limited maximum velocity.

energy level variances and subsequently less travel for local AIS and at lower speeds during cluster merging. Since, agent mobility and speed is minimal, each set of cluster merging contributes to less energy usage by the self-organization process. The energy saving becomes more evident for larger swarms spread over larger areas.

The clustering and sequential cluster merging simulation using local AIS was repeated for a range of $N = 50$ to $N = 1,000$ at increments of 50, with each N value case being independently repeated 5 times. The mean global energy equilibrium attainment time for each N is shown in Fig. 2.9. The equilibrium attainment time was observed to increase slowly with N as expected; with larger N more clusters were formed and the sequential merging process required more time to reach global equilibrium.

AIS Simulation

Figure 2.10a, 2.10b and 2.10c each illustrate sets of simulation time step sequences using the proposed method and its corresponding base method (a.1, a.2), (b.1, b.2) and (c.1, c.2) for scenarios S1, S2 and S3 respectively.

Following the d_{ij} inter-distance formulation of the proposed method, agents with high energy levels from the right in S1 fig. 2.10a (a.1), start to diffuse in to the rest of the group at $t = 30$ and $t = 80$. Similar behavior was observed in S2 fig. 2.10b (b.1) and S3 fig. 2.10c (c.1) with the proposed method, where agents with high energy levels from the ends and center respectively, diffuse throughout the group at $t = 30$, $t = 80$ and $t = 20$, $t = 60$. With high energy level agents placed throughout the group, the energy distribution following (2.17) reaches the group mean energy level equilibrium at $t = 229$, $t = 208$ and $t = 232$ for S1, S2 and S3 respectively.

In contrast, using the base method in each of the scenarios S1 fig. 2.10a (a.2), S2 fig. 2.10b (b.2) and S3 fig. 2.10c (c.2) respectively, all agents rendezvous to a minimal potential state at inter-distance d_e regardless of each other's energy level. In S1 fig. 2.10a (a.2), due to the left-skewed initial energy distribution, agents with higher energy levels clump together on the right. Similarly, agents with higher energy levels clump together on the ends and center in S2 fig. 2.10b (b.2) and S3 fig. 2.10c (c.2) respectively, because of the bi-modal and normal initial energy distribution in their corresponding scenarios. At time step $t = 229$, $t = 208$ and $t = 232$ for S1, S2 and S3, while the system has already reached the group mean energy level equilibrium using the proposed method, the base case was yet to reach equilibrium as seen from the simulation time step in each of the scenarios. The optimal placement of high energy agents throughout the group using the proposed energy distribution method ensured fast and efficient energy equilibrium attainment over the base method.

The convergence of energy levels of each agent to the group mean energy level for each of the described scenarios S1, S2 and S3 using the proposed energy distribution and the base method approaches is illustrated in fig 2.11, 2.12 and 2.13 respectively. The system converges to the mean group energy level at $t = 521$, $t = 398$ and $t = 260$ without using AIS for each of the S1, S2 and S3 scenarios. Therefore, 55%, 42% and 23% performance

(a.1) Resource distribution with AIS time lapse

(a.2) Resource distribution without AIS time lapse
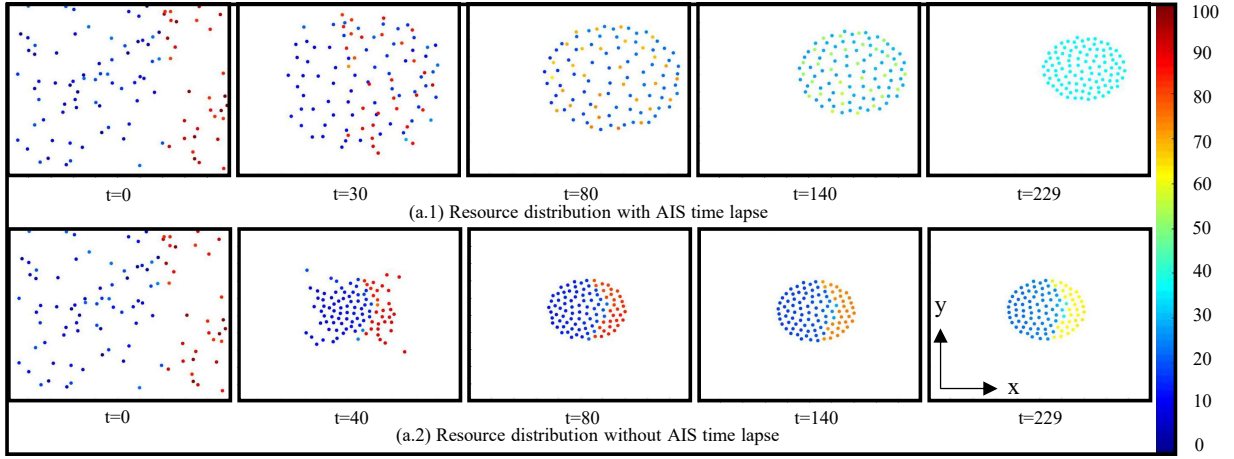
(a) S1 - Left skewed initial resource distribution along x-axis

(b.1) Resource distribution with AIS time lapse

(b.2) Resource distribution without AIS time lapse
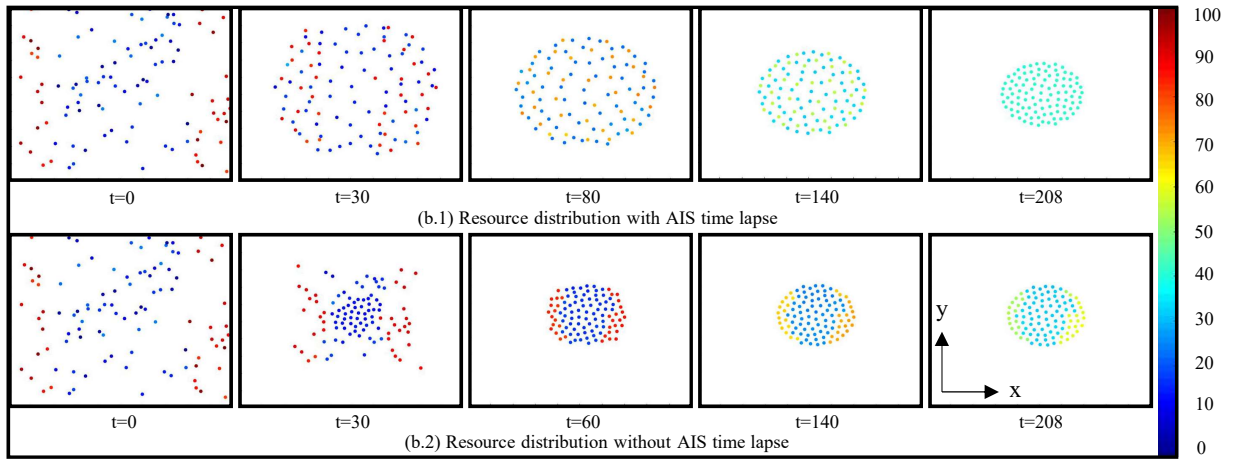
(b) S2 – Bi-modal initial resource distribution along x-axis

(c.1) Resource distribution with AIS time lapse

(c.2) Resource distribution without AIS time lapse
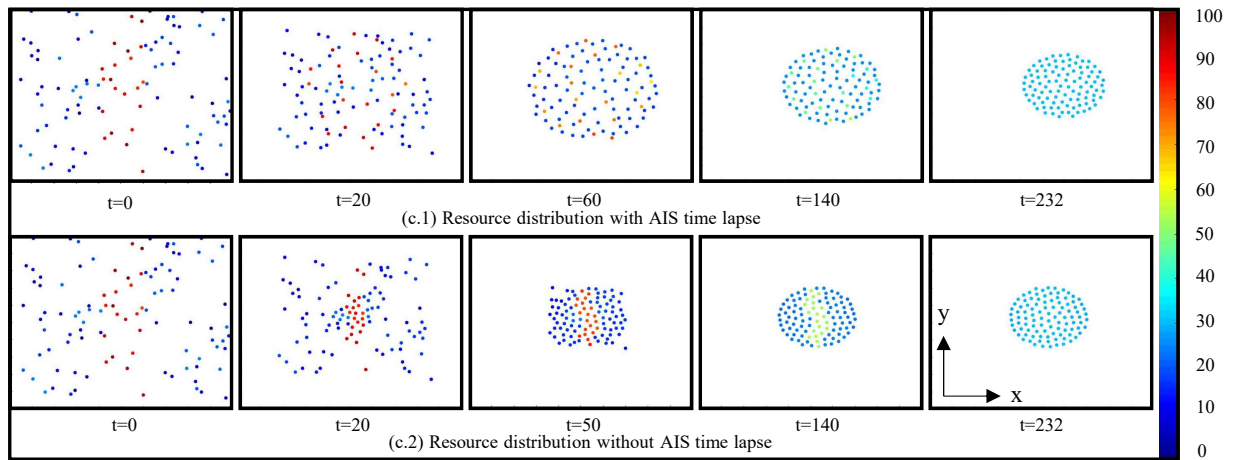
(c) S3 – Normal initial resource distribution along x-axis

Figure 2.10. Time lapse comparison of scenarios (a) S1: Skewed, (b) S2: Bi-modal, (c) S3: Normal initial energy distributions using the proposed energy distribution method and their corresponding base methods.

58
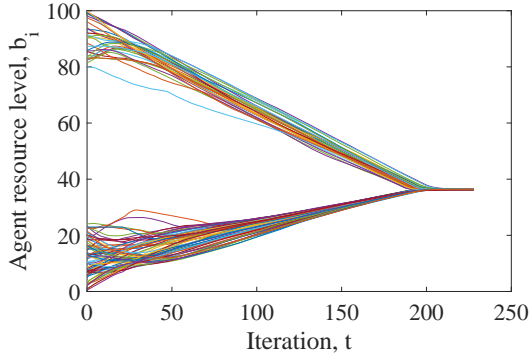
(a) S1: Skewed - convergence with AIS
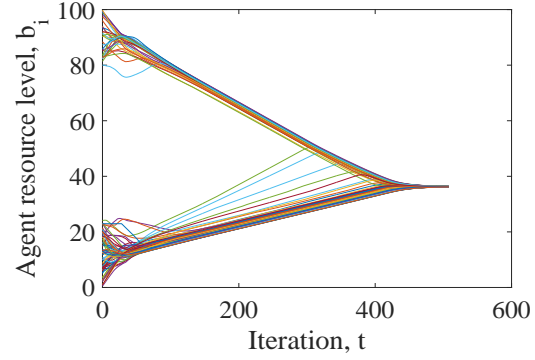
(b) S1: Skewed - convergence without AIS

Figure 2.11. S1: Skewed initial energy distribution - individual agent energy level convergence vs iteration time.
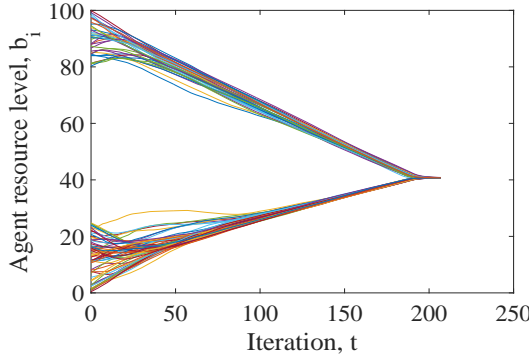
(a) S2: Bi-modal - convergence with AIS
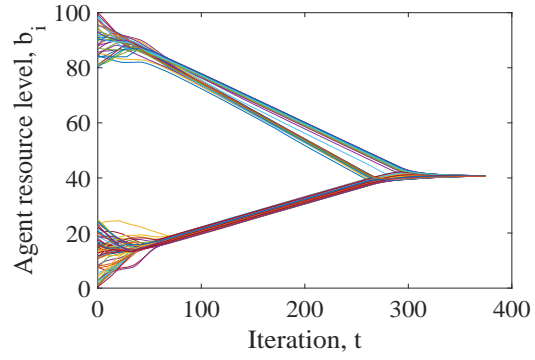
(b) S2: Bi-modal - convergence without AIS

Figure 2.12. S2: Bi-modal initial energy distribution - individual agent energy level convergence vs iteration time.

improvements in equilibrium attainment convergence time was obtained using the proposed energy distribution method over the base method.

The experiment was repeated for scenario S4 with a random initial energy distribution $5 \leq b \leq 100$ for all agents in the x-y plane. The system converged to $b_m = 57.57$ at $t = 149$ using AIS and at $t = 237$ without using AIS. Fig 2.14 plots the convergence of energy levels of each agent to the group mean energy level using the proposed and base methods. Significant performance improvement of 33% in equilibrium attainment convergence time was observed with the proposed method over the base method proving the effectiveness of the formulated d_{ij} function in efficient energy distribution in a group.
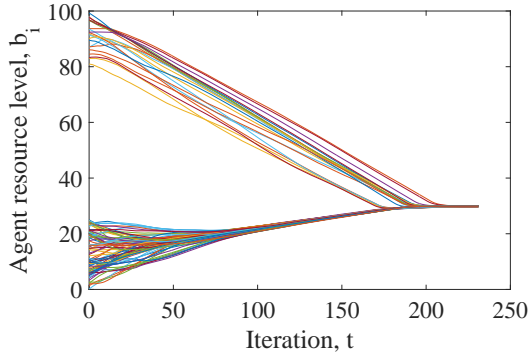
(a) S3: Normal - convergence with AIS
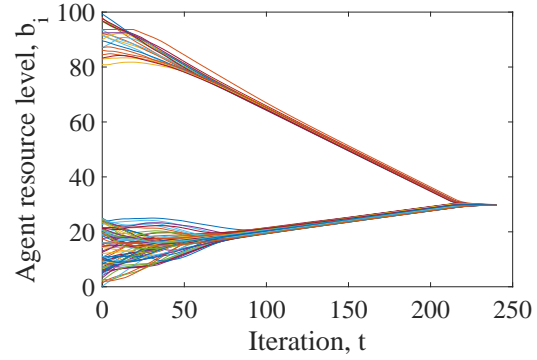
(b) S3: Normal - convergence without AIS

Figure 2.13. S3: Normal initial energy distribution - individual agent energy level convergence vs iteration time.
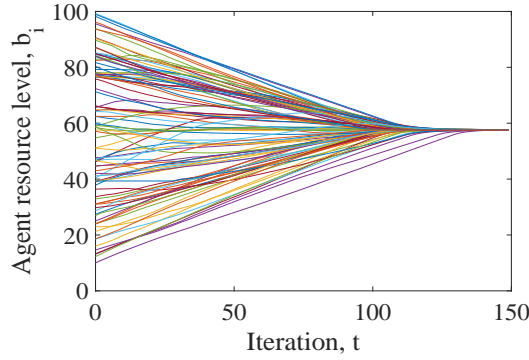
(a) S4: Random - convergence with AIS
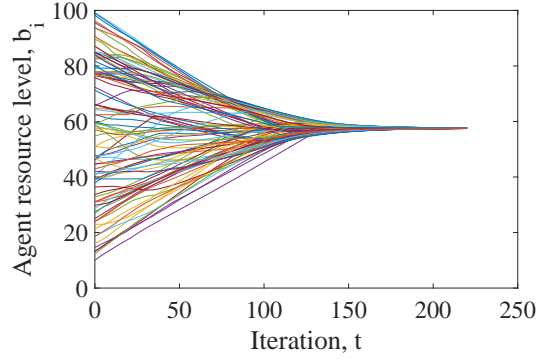
(b) S4: Random - convergence without AIS

Figure 2.14. S4: Random initial energy distribution - individual agent energy level convergence vs iteration time.

AIS Robustness & Scalability

The significance of the proposed method is that it adaptively distributes agents with higher individual energy levels throughout the entire group regardless of initial group energy distribution. The process is continuous over time and thus the optimum calculated inter-distance is always maintained throughout the group based on inter-agent energy levels at all time instances until equilibrium.

Observation 1: The proposed energy distribution method out-performed the base method in all scenarios S1, S2, S3 and S4 for $N = 100$ agents.

(a) S1: Skewed initial distribution scalability

(b) S2: Bi-modal initial distribution scalability

(c) S3: Normal initial distribution scalability

(d) S4: Random initial distribution scalability
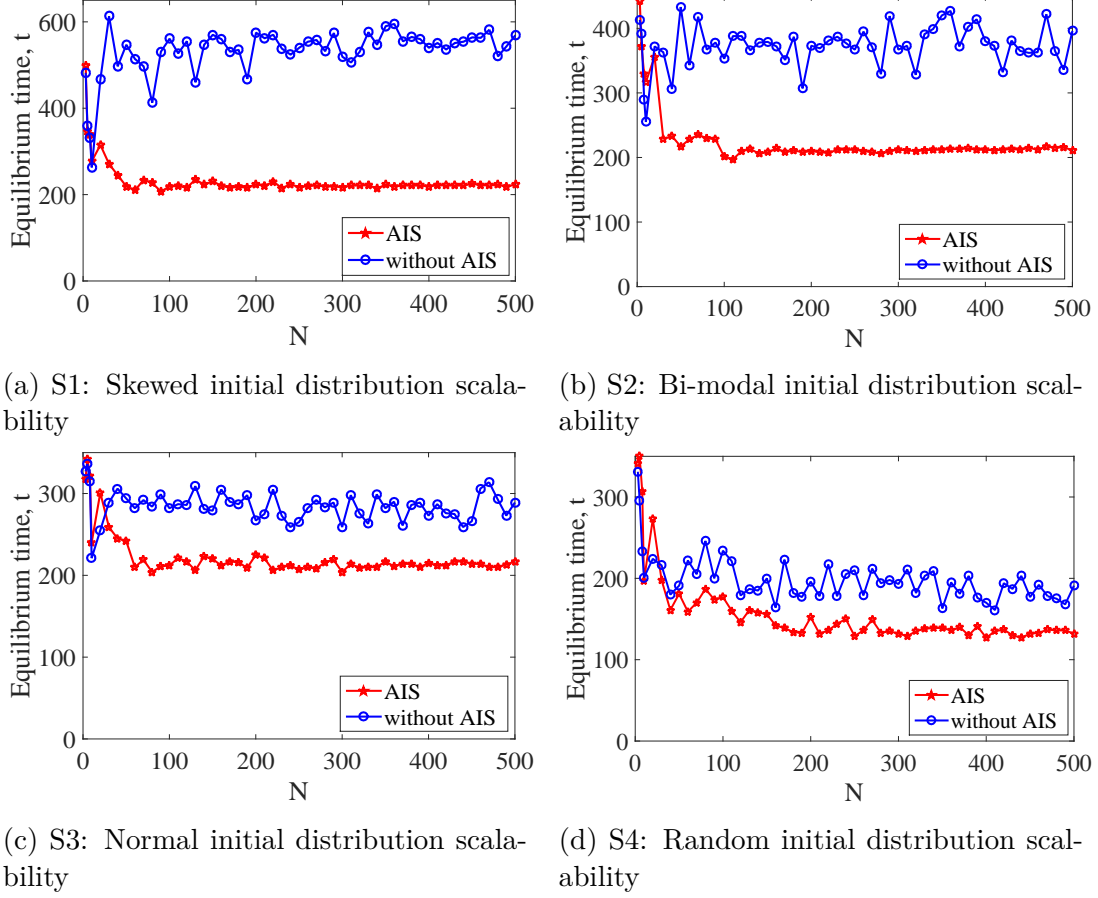
Figure 2.15. System convergence time to mean group energy level with increasing *N* for each of the four set scenarios with and without using AIS energy distribution.

Therefore, we conclude that the proposed energy distribution method using adaptive inter-agent spacing based on individual energy levels is robust to extreme initial group energy distributions.

Observation 2: At any given time, each individual agent classifies itself and others as either having an energy level above the mean or below to determine its inter-agent distance d_{ij}. For local energy distribution, it only considers agents within r_b. Therefore, the proposed method performs independent of the number of agents in the entire group at any given time.

Hence, we conclude that the proposed energy distribution method is also robust to dynamic changes in the number of agents in the group during the energy distribution process assuming no agent is incapacitated or faulty.

Observation 2 also supports scalability of the proposed method. To further investigate, we demonstrate the scalability by repeating scenarios S1, S2, S3 and S4 for $N = 3$ to 500, and plotting the time required for the system to reach the energy equilibrium for each case. Figure 2.15 plots the experiment results obtained from the proposed and base methods.

Observation 3: During the initial self-organization process where high energy bearing agents distribute themselves throughout the group, the high energy bearing agents are required to travel at relatively much higher speeds compared to the rest. As individuals get closer to the group mean energy level, the spacing between robots decreases narrowing pathways and preventing further self-organization of robots in the group.

An implementation of the proposed swarm clustering and sequential merging methodology for energy distribution in large swarms is presented in Section 2.4.4.

The proposed AIS energy distribution method consistently yielded shorter convergence times for increasing N. The most effective difference is seen in initially skewed energy distributions and the closest difference is seen with the random initial energy distribution.

At $N < 6$, inconsistent convergence times were obtained. In most cases the base method of without using AIS performed better since all robots converged together into a small enough group for fast energy distribution; whereas with AIS, larger inter-distances between robots meant larger traveling times until energy equilibrium attainment. Therefore, we conclude that the proposed AIS energy distribution method is effective for $N > 8$.

The scalability plots with increasing N shows a diminishing convergence time for small N and then gradually reaches a steady state. This is a consequence of using artificial potential functions to model the dynamics of the system. With larger N, a larger amount of energy transfer occurs resulting in longer convergence times. However, the total potential energy of the system is higher as well, with each agent experiencing larger attraction and repulsion forces resulting in faster movements in the environment. This contributes to smaller convergence times. As a result of cancelling effects of the two phenomenon, a steady convergence time is observed in all scenarios shown in Fig. 2.15 regardless of N.

2.5   Conclusion

This chapter of the dissertation presents energy sharing concepts for structured and unstructured robot groups on long-term missions. The structured robot group cyclic energy sharing concepts include an Emperor Penguin huddling-inspired position shuffling algorithm (PHS) and a gradient based energy sharing scheme. The unit robot design is described as a hexagonal structure with carefully placed inductive coils for charge sharing between agents. PHS allows individual robots equal opportunity to be at the center of the formation in turns. The unstructured robot group energy sharing and distribution concept includes an AIS control law based on energy levels of robot pairs. Based on observations of continuous merging and splitting of multiple Emperor Penguin huddles during body heat sharing and regulation, a clustering and sequential merging of small robot groups for global energy equilibrium attainment method is also proposed as a supplement to the AIS controller.

Structured case simulation results validate that formations of different sizes successfully survive longer as a group with the proposed cyclic PHS algorithm compared to the base case of individuals only relying on themselves. Unstructured case simulation results validate improved energy distribution performance with AIS for both random and extreme cases of skewed initial energy distributions in the group.

3. SURVIVING DAMAGING EXTERNAL STIMULI

The material in this chapter of the dissertation is partially based on the following previously published paper. The content has been added with the consent of all co-authors of the paper.

- "Penguin Huddling Inspired Distributed Boundary Movement for Group Survival in Multi-robot Systems using Gaussian Processes," T. Mina, B.C. Min, 2018 IEEE International Conference on Robotics and Biomimetics (ROBIO), Kuala Lumpur, Malaysia, December 12-15, 2018.

3.1 Introduction

Robots play an important role in exploring the unknown and in some of the harshest environments on Earth [56]. To survive severe damaging environments (strong directional winds, blizzards, dust storms, etc.), individual robots have traditionally required custom-built hardware to survive long-term exposure to extreme external stimuli. For instance, robots built for Antarctic explorations (such as NOMAD [57] and Cool [58]) encounter extreme cold temperatures and strong damaging winds even in the Antarctic summer [59]. In such conditions, electronic components require specially sealed, insulated, aerogel warm-housing [15] [60] for normal operation; lithium batteries despite being a popular choice, suffer severe power loss at temperatures below 0^oC [61]. Warm-up routines are often required as well to keep lubricants from stiffening. Such adaptations are expensive and in most cases specific to individuals and environmental conditions. Given the unpredictable nature of such conditions, designing individual robots that can take into account all possible scenarios is not feasible either.

As bio-inspiration of the research proposed in this chapter, we re-visit the Emperor Penguin huddling behavior presented in Section 1.1. While Emperor penguins have evolved to withstand very low temperatures on their own, they can only survive conditions as severe as Antarctic winters by being in a social group. Individual robots have been traditionally designed the same way, but we ask the question how being in a group can increase robustness in survivability. Similar to how penguins take turns being on the leeward side of the group during storms, robots could take turns settling on the leeward side to minimize damage by

physical protection from the group when no shelter is available nearby. In this chapter, we propose a distributed boundary movement methodology using Gaussian Processes Machine Learning (GPML) with a spectral mixture kernel to relocate individuals from the stimuli side to the global and an optimized health-loss-rate minima on the leeward side following two distinct settling conditions proposed in this chapter without requiring any communication or prior knowledge of group size or shape, when exposed to a damaging directional external stimuli. Fig. 1.1b shows the analogous process of Emperor Penguin huddling and boundary movement around the group in Antarctic winters.

3.2   Related Work

Body heat and the energy saving benefits of penguin huddling and shuffling has been studied in [39]. The dynamic movements in the huddle that allow an equal opportunity for all penguins to be at the center based on temperature changes within the huddle was explained in [62]. Despite numerous extensive studies, very few theoretical models of the boundary movement in a huddle has been put forward.

A theoretical model focused on the boundary movements of huddling penguins moving from the windward side to the leeward side was first proposed in [36]. Waters et al. [37] extended that work by taking into account an inviscid and irrotational wind flow and a temperature profile around the huddle. The huddle was created as a hexagonal grid based on [34] and assumed that the penguins did not displace one another and the penguin with the highest heat loss relocated to the centrally pre-computed best location in the huddle.

Previous work on robots following a boundary using machine learning include a wall-following robot that used linear regression and Support Vector Regression to predict motor commands to determine the direction of motion [63]. Programmable self-assembly of multi-robots was achieved by [64] using Kilobots [65] following the boundary of the group to form complex planar prescribed shapes. A centralized approach of robot relocation in a structured robot formation was previously studied in [66] assuming full communication and state information.

Adaptive behaviors by robots to external stimuli have primarily focused on peripheral stages of sensory perception or on peripheral motor control [67][68]. Conditioned reward-

based behavior to adapt to external stimuli using spiking neural networks was proposed by [69].

For our multi-robot system with distributed control and without communication, we build on the huddle modeling work by Waters et al. [37]. Since the robots are unaware of the size and shape of the huddle, nor have any information on a suitable safe relocation position, a machine learning approach is proposed where robots move along the boundary looking for a favorable position to relocate to, only relying on external stimuli readings and distance to neighbors. Our proposed method combines learning algorithms in artificial intelligence to multi-robot group survival decision making in extreme environments in a distributed manner.

3.3 Preliminaries

3.3.1 Robot Dynamics and Group Formation

We consider a scenario where a robot group has been deployed on a long-term mission without any human supervision and encounters a severe external stimuli without any shelter nearby. The huddling behavior of Emperor penguins involve tight packing of individuals for group survival. Therefore, we consider a closed hexagonal lattice formation for our group of robots with no empty spaces within the robot group. We let $r_i^t \in \mathbb{R}^2$ denote the position of the ith robot R_i on a planar surface with respect to a global inertial frame for i $= \{1, 2.., N\}$ at time instant t, with a neighbor detection radius of r_d. For simplicity, we model the robots as point masses with full actuation. The dynamic model of the ith robot can be written as, $\dot{r}_i = v_i$, $\dot{v}_i = u_i$; where v_i and u_i denote the absolute velocity and the control force for the corresponding robot i.

At any given time t, R_i can either be staying in formation (i $\in A$) or moving along the boundary (i $\in B$) where A is defined as the set of robots staying in formation and B the set of robots moving around the boundary. We assume every robot is equipped with distance sensors and are able to classify neighboring robots within r_d to be in A or B. We model robots in A and B to only interact with robots in their own set. This ensures that boundary moving robots do not displace robots that are currently in formation.
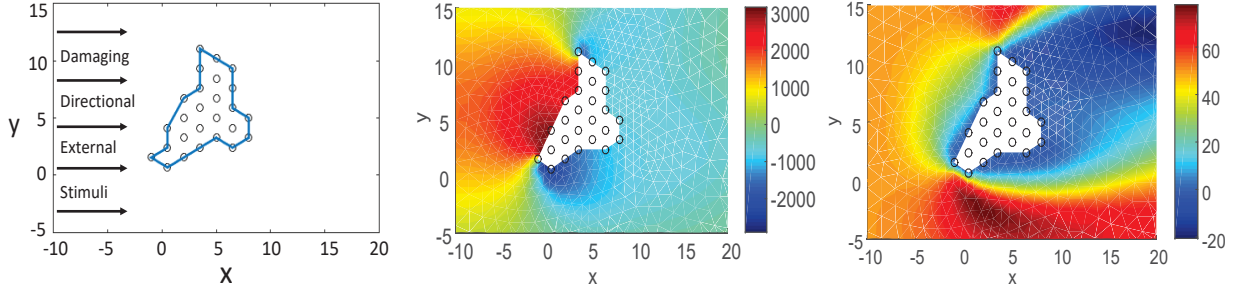
(a) N=26 robot hexagonal lattice formation with a damaging directional external stimuli along x^+.

(b) Pressure/Density $(units^4/t^2)$ distribution of modeled damaging directional external stimuli as a fluid flow.

(c) x-velocity $(units/t)$ distribution from modeling the damaging directional external stimuli as a fluid flow.

Figure 3.1. Damaging directional external stimuli as a viscous incompressible flow around the robot formation.

3.3.2 Modeling Damaging Directional External Stimuli and Robot Health Loss

For a multi-robot group on a planar surface modeled as a hexagonal lattice formation, we assume a damaging external stimuli from the left, detrimental to the set of exposed robots. The setup is illustrated in Fig. 3.1a. To maintain generality of a damaging directional external stimuli, we set the following requirements:

- A direct damaging force on the stimuli side.

- Stimuli affects flank members exposed to the outside.

- Direct protection is only available on the leeward side.

We model such a damaging external stimuli as a directional, viscous and incompressible fluid flow with an inlet on the $x = -10$ line, flow directed towards x^+ with inlet velocity, $v_x = v_f$ around our robot group. Fig. 3.1b-3.1c show the *pressure/density* distribution and v_x distribution of the fluid around the robot group respectively. We assume high *pressure/density* zones and high v_x zones as damaging elements to an exposed robot in the group. The modeled fluid flow fulfills our set requirements for a damaging directional external stimuli as follows:

- Creates a high pressure zone on the stimuli side (analogous to a direct damaging force).

- Flanks experience high fluid velocity with variations in pressure (damaging for exposed flank robots).

- A low absolute pressure zone with low fluid velocity on the leeward side (protected zone).

The illustrated fluid flow was simulated in the MATLAB QuickerSim toolbox with viscous coefficient $v = 10$. We assume that robots have negligible spacing in between such that the robot group may be considered a solid non-deformable planar object. Thus, the fluid flow model may be simplified as a flow around a single solid object.

At time t, R_i measures the external stimuli at its location r_i to determine its rate of health loss written as,

$$L_i^t = \begin{cases} \frac{\beta_P |P_i^t| + \beta_V V_i^t}{n_i^t} & \text{if } n_i^t < 6 \\ 0 & \text{else} \end{cases} \tag{3.1}$$

where β_P and β_V are scaling constants, P_i^t and V_i^t are measured pressure and fluid velocity and n_i^t is the number of neighbors detected within r_d.

R_i, $i \in A$ breaks off the formation if $L_i^t > L_{threshold}$, such that R_i for $A \leftarrow A \setminus \{i\}$, $B \leftarrow B \cup \{i\}$ starts moving along the boundary with η determined as away from the direction of the damaging external stimuli.

3.4   Methodology

3.4.1   Robot Interaction and Motion Control

The hexagonal lattice formation with robots in A is maintained using an artificial potential U_I previously established in [70] written as,

$$F_I = \begin{cases} \alpha_I (\ln(r_{ij}) + \frac{d_0}{r_{ij}}) & 0 < r_{ij} < d_1 \\ \alpha_I (\ln(r_{d_1}) + \frac{d_0}{d_1}) & r_{ij} \geq d_1. \end{cases} \tag{3.2}$$

68

where r_{ij} is the distance between robots i and j in A, α_I is a scalar control gain; d_0 and d_1 are scalar constants such that $d_0 < d_1 \leq r_d$. At equilibrium, all robots are grouped together in the hexagonal lattice formation. The hexagonal lattice formation is locally stable in the sense of Lyapunov because by design, the equilibrium is a global minimum of the total artificial potential [70]. Robots in B also interact with other members of B exclusively using Eq. (3.2)-(3.4) to prevent collision.

We assume that the robot group is initially centered at location r_c. An attractive potential is defined for a robot determined as the geometric group centroid of robots in A towards r_c where neighboring robots match this attractive potential of the initiator detected within d_{ij}. The potential function can be written as,

$$
F_c = \begin{cases} \frac{1}{2}\alpha_c r_{ic}^2 & \text{if } i \in A \text{ is the group center} \\ \frac{1}{2}\alpha_c r_{ic}^2 & \forall R_j, j \in A, \text{ if } i \in A \text{ is the group center, } j \neq i, \ 0 < r_{ij} < d_1. \end{cases} \tag{3.3}
$$

The geometric group center is determined in a distributed manner using the Barycenter Algorithm discussed in Section 3.4.3. The inter-robot interaction force for all $R_i \in A$ can therefore be written as,

$$
f_I = \begin{cases} \nabla_{r_{ij}} F_I + \nabla_{r_{ic}} F_c & 0 < r_{ij} < d_1 \\ \nabla_{r_{ic}} F_c & r_{ij} \geq d_1. \end{cases} \tag{3.4}
$$

We define an artificial potential F_d and the attractive force f_d for the tangential boundary movement of robot R_i, $i \in B$ around its closest neighbor R_j, $j \in A$ by,

$$
F_d = \frac{1}{2}\alpha_d r_{ij}^2 \qquad\qquad f_d = \nabla F_d \tag{3.5}
$$

where α_d is a scalar gain constant, $r_{ij} \leq r_d$ is the distance between R_i and R_j. We denote f_t as the tangential force vector derived with magnitude equal to $||f_d||$ and direction $\theta_t = \theta_d + \eta\frac{\pi}{2}$, where θ_d denotes the direction of f_d and $\eta \in \{1,-1\}$ depending on the direction of movement.

Therefore, the control input can be written as,

$$u_{\mathrm{i}} = \begin{cases} -\sum_{\mathrm{j}\neq\mathrm{i},\mathrm{j}\neq m}^{N} f_I(r_{\mathrm{ij}}) & \mathrm{i},\mathrm{j} \in A, m \in B \\ -f_t(r_{\mathrm{ij}}) & \mathrm{i} \in B, \mathrm{j} \in A. \end{cases} \qquad (3.6)$$

We constraint each robot with a maximum velocity v_m.

3.4.2 Distributed Robot Relocation using Gaussian Processes Machine Learning (GPML)

Once movement is initialized for R_{i}, $\mathrm{i} \in B$ the time is recorded as t^{i}. R_{i}, $\mathrm{i} \in B$ continues to move along the boundary unaware of the size and shape of the robot group, without moving backwards or displacing neighboring robots, measuring fluid pressure P_{i}^t, fluid velocity V_{i}^t at coordinates $r_{\mathrm{i}}^t = (x_{\mathrm{i}}^t, y_{\mathrm{i}}^t)$ at every time instant $t \geq t^{\mathrm{i}}$. Without any communication it is unable to determine its safest relocation position from the group where absolute pressure and fluid velocity are lowest suggesting a minimal L_{i} position from the external stimuli. We denote the current time as t_c.

Gaussian Processes (GP) are a powerful regression technique which provide Bayesian non-parametric smoothing and interpolation with a set of basis functions. We define a distribution over functions $f(x)$,

$$
\begin{aligned}
f(x) &\sim \mathscr{GP}(m(x), k(x,x)) \\
m(x) &= \mathbb{E}[f(x)] \\
k(x,x) &= \mathrm{cov}(f(x), f(x))
\end{aligned}
\qquad (3.7)
$$

where $x \in \mathbb{R}^S$ is an arbitrary input variable over space S, $m(x)$ is the mean and $k(x,x)$ is the covariance function respectively.

The properties of the likely functions under a GP are controlled by the positive definite covariance function. The choice of the kernel affects performance significantly on a given

task. A commonly used kernel function is the squared exponential kernel (3.8) where the only covariance structure learned from training data is the length scale l,

$$k_{SE}(x,x) = \exp(-0.5||x-x||^2/l^2). \tag{3.8}$$

However, by using a mixture of Gaussians that have non-zero means, a much wider range of spectral densities can be obtained [71]. Therefore, for better performance we use the spectral mixture kernel,

$$k_{SM}(\tau) = \sum_{q=1}^{Q} w_q \prod_{s=1}^{S} \exp\{-2\pi^2 \tau_s^2 v_q^{(s)}\} cos2\pi\tau_s\mu_q^{(s)} \tag{3.9}$$

where w_q are weights that specify the relative contribution of each mixture component, Q is the number of Gaussians on $\mathbb{R}^S$ with the qth component having mean $\mu_q = (\mu_q(1),...,\mu_q(S))$ and covariance matrix $M_q = \text{diag}(v_q(1),...,v_q(S))$ and τ_s is the sth component of the S dimensional vector $\tau = (x-x)$.

The advantage of GP over other learning approaches is that it provides well defined confidence intervals important to assess the predicted model. Therefore, we propose GP machine learning at time intervals of t_{int} for R_i, $i \in B$ to determine pressure and velocity models $f_i^P(t)$ and $f_i^V(t)$ as trends in P_i^t and V_i^t measurements collected as training data between $t^i \leq t \leq t_c$ respectively, and extrapolate the models to predict if a better relocation position is available ahead up to time t_{extrap}. We define a cost function $L_i^c(t)$ using weighted $f_i^P(t)$ and $f_i^V(t)$ components and determine a global minima corresponding to the safest location in the group at $t = t_{min}$. The cost function L_i^c is defined as,

$$L_i^c(t) = \lambda_1 |f_i^P(t)| + \lambda_2 f_i^V(t) \tag{3.10}$$

$$t_{min} = \arg\min_t L_i^c \tag{3.11}$$

where λ_1 and λ_2 are weights of each component. The global minima is determined by a simple exhaustive search. We present two settling conditions for robots following the boundary.

Settling at Global Minimum Health Loss Rate

In this global health loss rate minimum settling condition, robots prioritize getting to the estimated global health loss rate minimum regardless of the loss of health getting to the estimated location. The robot continues to move along the boundary until the estimated global health loss rate minimum is reached. After every GP iteration at time interval t_{int}, the determined t_{min} is compared to t_c to asses if R_i, $i \in B$ should settle or continue to move. If $t_c - t_{tol} \leq t_{min} \leq t_c + t_{tol}$, where t_{tol} is a defined tolerance constant, implying that t_{min} has been found within a certain tolerance of the current iteration time t_c, then the best location is in the immediate vicinity of $r_i^{t_c}$ and R_i settles at the current location. If not, R_i, $i \in B$ continues to move along the boundary in the same direction for $t_{min} > t_c + t_{tol}$. We ensure $t_{min} \geq t_c - t_{tol}$ is always true such that R_i, $i \in B$ does not have to move backwards by setting a small enough t_{int}. With more training data after every iteration, the predicted models improve over time providing better estimations of the global minima.

Settling at Optimized Minimum Health Loss Rate

For large robot groups, the proposed global health loss minimum settling method may not be ideal when robots lose more health during the relocating process itself due to the large distance they may have to cover to get to the estimated global health loss minimum position on the leeward side. Therefore, we propose a second settling method specifically for large robot groups. Once a local health loss rate minimum is reached, the boundary following robot evaluates the total health loss getting to the detected global health loss rate minimum from the current location, and compares it with the total health loss settling at the current local health loss minimum location for the same duration. The local current health loss rate must be below the acceptable health loss rate threshold beyond which robots decide to relocate; i.e. $L_i^c(t) \leq L_{threshold}$. The total health loss getting to the detected global health loss rate minimum can be evaluated as,

$$L_i^g = \int_{t_c}^{t_{min}} L_i^c(t). \tag{3.12}$$

The total loss of health settling at the current local health loss minimum location over the same duration can be calculated as $L_{\mathrm{i}}^l = (t_{min} - t_c)L_{\mathrm{i}}^c(t_c)$. Following this optimized health loss assessment during boundary following, the robot settles at the current local health loss rate minimum if $L_{\mathrm{i}}^l < L_{\mathrm{i}}^g$.

For both proposed settling methods, once the respective settling condition is met by R_{i}, $\mathrm{i} \in B$, the robot group is updated as $B \leftarrow B \setminus \{\mathrm{i}\}$, $A \leftarrow A \cup \{\mathrm{i}\}$.

3.4.3 Distributed Robot Group Location Maintenance

The continuous relocation of individual robots from the stimuli side to the leeward side creates a net movement of the robot group away from the initial group location. Therefore, in order to maintain the initial position of the robot group center regardless of the group shape, a counter drift strategy is proposed that pushes the robot group centroid back to the initial group location.

Under the distributed computation and limited communication constraints of the system, each robot in A must individually determine if it is the group center. We base our center maintaining solution on the distributed group center identification research using the idea of morphogen gradients by Mamei et al. in [72]. The gravitational center of a given group of robots is determined by the Barycenter algorithm briefly described in Algorithm 2. The Barycenter algorithm uses the concept of morphogen gradients to spatially identify group centers. Each robot broadcasts a message containing its unique name and an initial counter value of zero to its neighboring robots within a limited communication range. Neighboring robots re-broadcast that message incrementing the counter by one, until the gradient has been propagated to all robots in the group. The process is repeated by each robot initiating a gradient and the rest propagating the incremented counter. During this continuous process, each robot stores and forwards only the minimum gradient value it has received from a unique robot name analogous to broadcasting the shortest distance from it. Each robot may asses if it is the group barycenter by comparing its own sum of all received gradient values from its neighbors with the sum of all gradient values received by its neighbors; if a robot's sum of received gradient values is smaller than all its neighbors, it is positioned with a sum-total

---
Algorithm 2 Pseudo-code of the Barycenter Algorithm

1: *barycenter* = *FALSE*
2: *sum_of_gradients* = 0
3: Initiate own gradient
4: while (1) do
5:     *gradient* ←gradient from all neighbors
6:     *sum_of_gradients* = ∑ *gradient*
7:     *count* = 0
8:     for all neighbor robots do
9:         if *neighbor*[i].*sum_of_gradients* > *sum_of_gradients* then
10:            *count* + +
11:    if *number_of_neighbors* == *count* then
12:        *barycenter* = *TRUE*
13:    else
14:        *barycenter* = *FALSE*
---

shortest distance from all other robots in the group. Therefore, the identified robot is the group barycenter.

Variants of the Barycenter algorithm have been widely used in several other applications including leader election [73], region selection using multiple gradients [74] and communication [75] in large swarms etc.

Once the group center is determined, the robot determined to be the group barycenter moves towards the group initial location following the attractive artificial potential presented in Eq. 3.3. Neighboring robots match their velocity to the detected motion of the initiator. Neighbors of these neighbors follow the same process of velocity matching until the initiator motion towards the initial goal location is propagated throughout the robot group consisting of robots in *A*. A 1D implementation of this velocity matching method has been previously used to model the travelling waves phenomenon in huddled groups of penguins with a time delay constant [76]. Given the tightly packed hexagonal lattice structure of our proposed robot group, we assume velocity matching occurs without any delay in any direction on the plane.

Table 3.1. Validation Scenarios for Surviving Damaging Directional External Stimuli

Simulation scenario	Conditions for robot relocation
S1	GP estimated global minima settling
S2	Local minima settling with $L_i^{t_c} < L_i^{t_i}$
S3	Optimized settling with group location maintenance
S4 (control)	Robots do not relocate

Table 3.2. Validation Parameters for Surviving Damaging Directional External Stimuli

Parameter	Value	Parameter	Value
d_0	$\sqrt{3}$ units	β_P/β_V	2.05
d_1	$d_0\sqrt{3}$ units	α_I	4
λ_1/λ_2	2.05	α_d	8
t_{tol}	$2ts$	v_m	0.25 units/ts
t_{int}	$5ts$ for $(t_c - t^i) > 30ts$	r_d	d_1
$L_{threshold}$	0.01		

3.5   Validation

3.5.1   Setup

To validate the two proposed GPML based relocation methods, we show that R_i, i $\in$ $\{1, 2.., N\}$ on the exposed side of the group is successfully able to move from the stimuli-side to the leeward side health-loss-rate minima of the group, using external stimuli measurements only, without any communication requirements or prior knowledge of the group size or shape. Detailed comparison studies of robot health loss are presented for the proposed global and optimized health loss rate minima settling with local minima settling and a no-relocation case as the control scenario. Scalability analysis of the proposed settling methods are also investigated.

The validation process is set up with four scenarios to establish the need and effectiveness of the proposed GPML estimated distributed relocation methods as presented in Table 3.1. We compare S1 and S2 to show the importance of using a relocation by health-loss-rate global minima approach in comparison to local minima; the use of a learning algorithm is also justified. We compare S1 with S3 to assess the need of the optimized settling method

weighing predicted health loss during the relocation process. S1, S3 and S4 are finally compared to show the extent of improved survivability of individual robots and the group as a whole with the proposed settling methods in comparison to a control group where robots do not relocate or seek safety.

We consider groups of N robots in a closed hexagonal lattice formation on a plane as previously shown in Fig. 3.1a. The group is exposed to a damaging directional external stimuli modeled as a viscous incompressible fluid flow from the left with $v_f = 1$ *units*$/t$ and $v = 10$ as shown in Fig. 3.1b - 3.1c. We assume the following:

- Robots do not communicate with each other during relocation.

- Robots do not displace each other.

- Robots can measure distance to neighbors within r_d.

- Robots can measure external stimuli.

- All robots are identical in shape and size.

For demonstration purposes, we track and present the progress of five randomly picked robots from the stimuli side at t_0 denoted as R_i, $i \in G_N$ where G_N is the set of the five randomly picked robot indices. For all scenarios, we initialize the simulation at time t_0 with sampling time $\partial t = 0.1$ and time step unit written as (ts). At t_0, $\forall R_i$, $i \in A$. At every time instant t, R_i determines its L_i^t using (3.1). For comparison between the scenarios, we denote the final health-loss-rate for R_i, $i \in G_N$ when settling under S1 as $(L_i^t)_{S1}$, S2 as $(L_i^t)_{S2}$, S3 as $(L_i^t)_{S3}$ and S4 as $(L_i^t)_{S4}$. The simulation parameters used are exaggerated for brevity and are listed in Table 3.2. r_d is chosen to be the minimum distance to possible immediate neighbors to show the effectiveness of the proposed algorithm even with limited sensing. The proposed concept of relocating individuals to the leeward side is a continuous process in the group; for presentation and analysis purposes the simulation is stopped at $t = 55$.
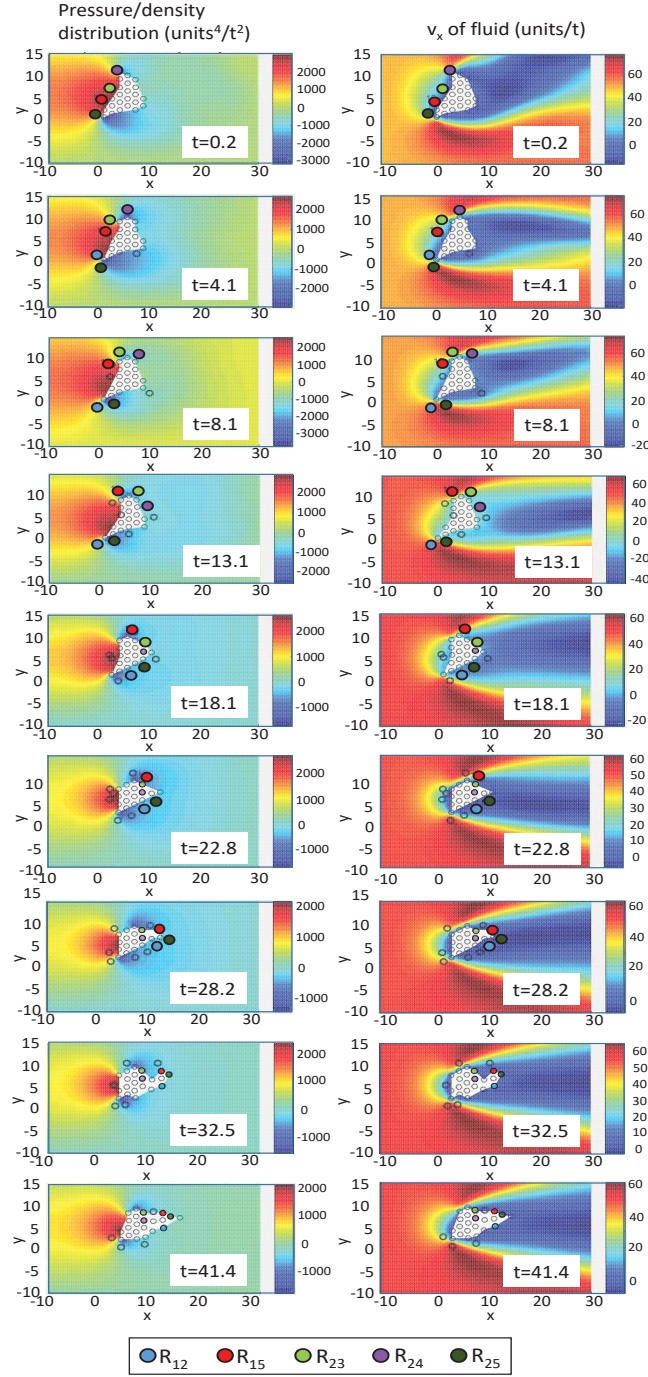
Figure 3.2. Simulation time-lapse for $N = 26$ in S1, showing the progress of five randomly picked robots (R_{12}, R_{15}, R_{23}, R_{24}, and R_{25},) in G_{26} exposed to a damaging directional stimuli along the x^+ direction. The robots successfully move along the boundary from the damaging stimuli side to the leeward side of the group and settle at the health-loss-rate global minima determined by the proposed GP estimated global minima methodology.

Figure 3.3. L_i^t for i $\in G_{26}$ in S1 decreases with time as the robots move from the damaging stimuli side to the leeward side using the proposed GP estimated global minima method.

3.5.2 Relocation using S1 vs. S2

Fig. 3.2 shows the progress of the boundary movement of R_i, i $\in G_{26}$, where $G_{26} = \{12, 15, 23, 24, 25\}$ along with the fluid pressure and velocity distribution around the robot group with changing boundary at specific time intervals. Fig. 3.3 tracks the corresponding L_i^t for robots R_i, i $\in G_{26}$ following their boundary movements.

At t_0, R_{15}, R_{23}, R_{24} and R_{25} are directly exposed to the external stimuli and start to move along the boundary as shown at time $t = 0.2$. At $t = 0.6$, R_{12} becomes exposed as R_{15} and R_{25} moved away; therefore, R_{12} starts to move along the boundary as well, as shown at time $t = 4.1$. R_{24} was successfully able to determine its global minima on the leeward side at $t = 13.1$, followed by R_{23} at $t = 14.7$. R_{25} reached a minima close to zero at $t = 13.2$ but continued to move based on its estimation of a global minima being further ahead. R_{25} finally settled at $t = 29.7$. R_{15} and R_{12} settled around the same time at $t = 29.5$ and $t = 29.6$.

L_{24}^t reached zero after $t > 12$ as it was surrounded on all sides by neighbors; L_{12}^t, L_{15}^t, L_{23}^t and L_{25}^t get very close to zero since the corresponding robots stay on the boundary of the robot group even at $t = 41.4$. L_{avg}^t plots the average health loss rate of the five tracked robots in Fig 3.3.

While moving around the flanks and extrema of the group boundary, all robots experienced a sudden increase in L_i^t. In this region, v_x is at its peak along with very low pressure. Since L_i^t considers the absolute value of the pressure component, the robots experienced the
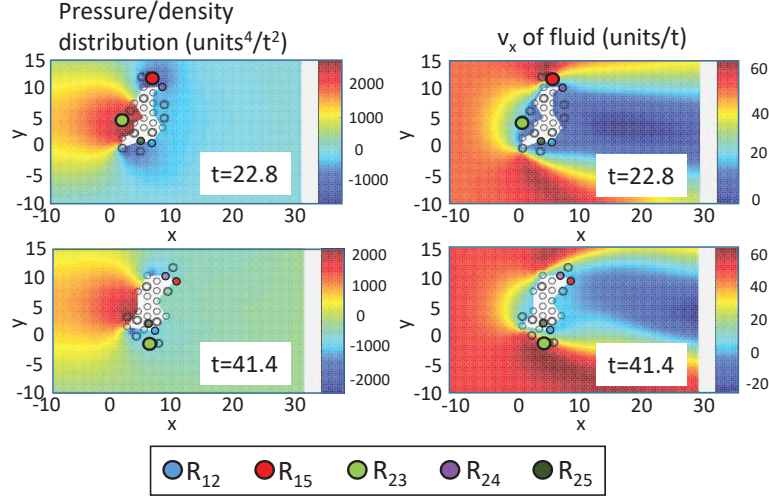
Figure 3.4. Simulation time instances for $N = 26$ in S2, showing the progress of five randomly picked robots in G_{26} exposed to a damaging directional stimuli along the x^+ direction. The robots settle along the group flank boundary using the local minima methodology.

highest health loss rate here modeled by (3.1) as opposed to the stimuli-side where v_x is low with very high pressure. Regardless, Gaussian Processes estimation was able to cope with such extreme fluctuations to determine the overall trend in the measurements; the global minima in terms of health loss rate was determined to be further ahead for each robot. No communication was necessary at any time between the robots for relocation.

The relocation process continued for other robots as well and over time as more and more robots successfully relocated to the leeward side, an aerodynamic group boundary was obtained as shown at $t = 41.4$. The protruding flanks of the initial robot group boundary gave away creating a streamlined shape and the initial high pressure zone on the stimuli side shrank considerably over time. With this continuous relocation process, the robot group was observed to drift away from the stimuli as expected with the proposed group location maintenance method.

The simulation was repeated with the same robot group setup of $N = 26$ and damaging external stimuli model with robots measuring P_i^t and V_i^t at every time instant and relocating to L_i^t local minima. As R_i moved with time, the change in the calculated L_i^t was checked continuously for a local minimum. Upon determining the local minimum at time t_{min}, if $t_c - t_{tol} \leq t_{min} \leq t_c + t_{tol}$, R_i settled at t_c if $L_i^{t_c} < L_i^t$.
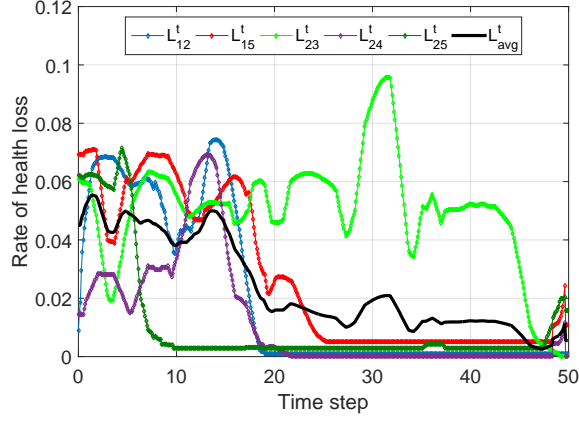
Figure 3.5. L_i^t for $i \in G_{26}$ in S2 decreases with time for some individuals as the robots move along the boundary to relocate using the local minima methodology.

The simulation progression of S2 at time instants $t = 22.8$ and $t = 41.4$ is shown in Fig. 3.4 and the corresponding L_i^t, $i \in G_{26}$ is plotted in Fig. 3.5. Comparing the progress of S2 with S1 at $t = 22.8$ and $t = 41.4$ in Fig. 3.4 and Fig. 3.2 respectively, we make the following observations:

- R_{12}, R_{15}, R_{24} and R_{25} settled at boundary extrema in the local minima case with final $(L_i^t)_{S2} > (L_i^t)_{S1}$ at the end of $t = 41.4$.

- R_{23} was unable to follow the same path as before because of frequently changing group boundary in the local minima case and was still moving after $t = 41.4$.

In the local minima case, individual robots moved short distances to a local minimum and settled for short periods of time before moving again. With this method of moving, individuals are constantly moving and settling and may eventually reach a rate of health loss global minima at a certain time and position around the fast changing boundary, but it is not guaranteed. The local minima method was chaotic in comparison and did not allow individuals an equal opportunity to reach the best available position around the group boundary for survival. The global minima methodology also created an aerodynamic group boundary over time as opposed to the local minima methodology where the flanks expanded as seen at time $t = 41.4$ in Fig 3.4. Such observations prove that the proposed GP estimated health-loss-rate global minima method is essential for group survival of individuals in the long run.

(a) L_i^t for i $\in G_{35}$ with time.   (b) L_i^t for i $\in G_{70}$ with time.   (c) L_i^t for i $\in G_{107}$ with time.

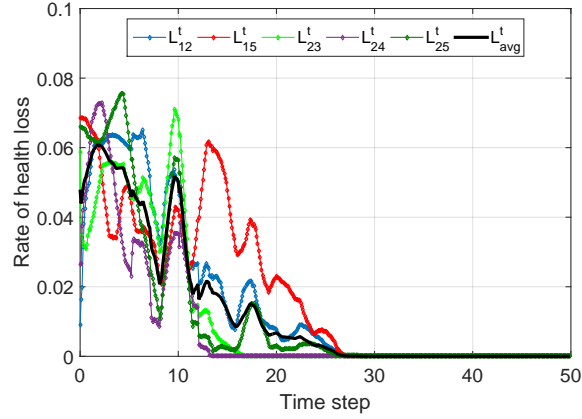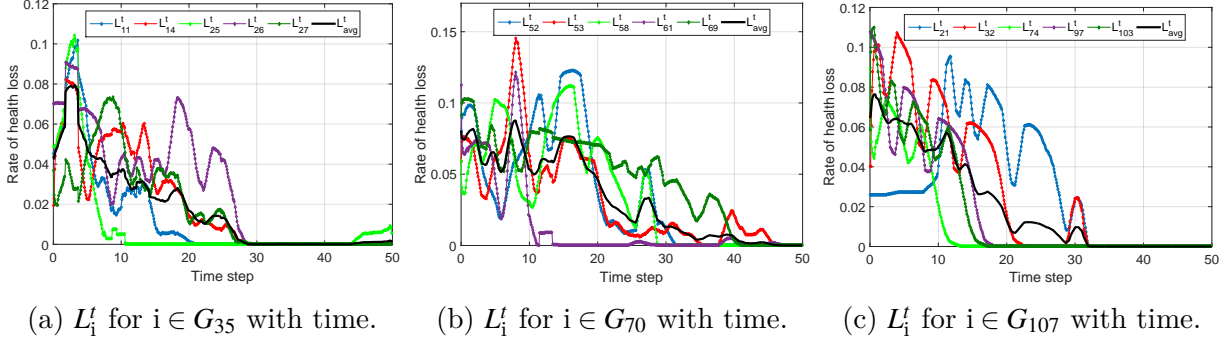Figure 3.6. L_i^t for the tracked robots in each of the $N = 35$, $N = 70$ and $N = 107$ cases for S1 decreases with time as the robots move from the damaging stimuli side to the leeward side using the proposed GP estimated global minima method.

Scalability Analysis of S1

To verify that the conclusions from S1 hold true over a range of N, the simulation was repeated for $N = 35$, 70 and 107 with arbitrary formation shapes against the same modeled fluid flow as external stimuli. For each N case, five randomly picked robots R_i on the stimuli side of the group were tracked; i $\in G_{35}$ for $N = 35$, i $\in G_{70}$ for $N = 70$ and i $\in G_{107}$ for $N = 107$ where $G_{35} = \{11, 14, 25, 26, 27\}$, $G_{70} = \{52, 53, 58, 61, 69\}$ and $G_{107} = \{21, 32, 74, 97, 103\}$, respectively. Their health loss rate L_i^t with time corresponding to movement around the boundary is shown in Fig. 3.6a-3.6c. The simulations were allowed to run up to $t = 50$.

In each case, all tracked robots were able to successfully move from the stimuli side to the estimated best location on the leeward side. For $N = 35$ and $N = 70$, all tracked robots were able to move at $t = t_0$. For $N = 107$, R_{21} regardless of having $L_{21}^t > L_{threshold}$ at $t = t_0$ was unable to move without displacing a neighbor. The sudden increase in L_{21}^t between $9 < t < 12$ is as a result of its neighbors moving away for relocation leaving R_{21} with a higher L_{21}^t and able to move.

We denote the average time required for convergence of L_{avg}^t to the health-loss-rate global minima as t_{min}^{avg}. t_{min}^{avg} for $N = 26$ is significantly smaller than t_{min}^{avg} for $N = 107$ because of the large difference in group size. However, t_{min}^{avg} for $N = 70$ is greater than t_{min}^{avg} for $N = 107$. This is because the initial shape of the $N = 70$ robot group had larger protruding flanks than $N = 107$. As a result, robots on the stimuli side for $N = 70$ had to travel longer distances

in comparison to reach the health loss global minima on the leeward side. This observation suggested that t_{min}^{avg} for different N cases has a strong correlation with the size and shape of the robot group. Regardless, the scalability of the proposed GP estimated global-minima method was established without any effects on the outcome due to group size or shape.

3.5.3 Relocation using S3 with Group Location Maintenance

The GPML based optimized health loss rate robot relocation process is specifically designed for robots to assess the health loss during the relocation process in determining whether to settle at a current local minimum under the acceptable health loss rate threshold or keep moving forward towards the GPML estimated global health loss minima.

The local health loss rate minima settling method in S2 resulted in robots continuously settling along shielded pockets within the flanks of the robot group, which in turn caused the robot group shape facing the stimuli to eventually elongate. The method was concluded to be significantly worse for smaller robot groups where the elongation took place within a shorter time span. Therefore, the optimized health loss rate settling method where robots may settle at local health loss rate minima around the flanks is investigated for smaller and larger N robot groups with the same fluid pressure and velocity external stimuli model around the robot group. Time lapse illustrations of the implemented optimized health loss rates settling method for $N = 35$ and $N = 70$ robot groups are shown in Fig. 3.7 for comparison purposes.

For the smaller robot group, the time lapse images show the progress of the boundary movement of R_i, $i \in G_{35}$, where $G_{35} = \{14, 26, 27, 31, 34\}$ along with changing boundary at specific time intervals. Fig. 3.8a tracks the corresponding L_i^t for robots R_i, $i \in G_{35}$ following their boundary movements. All tracked robots were successfully able to relocate following the optimized health loss rate minima settling method; the individual health loss rate of all robot is observed to reach close to zero after a single relocation cycle within the simulation time frame. L_{avg}^t plots the average health loss rate of the five tracked robots. The same conclusion could be made following similar observations for the larger robot group of $N = 70$ robots. The time lapse images show the progress of the boundary movement of R_i, $i \in G_{70}$, where $G_{70} = \{52, 53, 58, 61, 69\}$ along with changing boundary at specific time intervals. Fig. 3.8b tracks the corresponding L_i^t for robots R_i, $i \in G_{70}$ following their boundary movements.
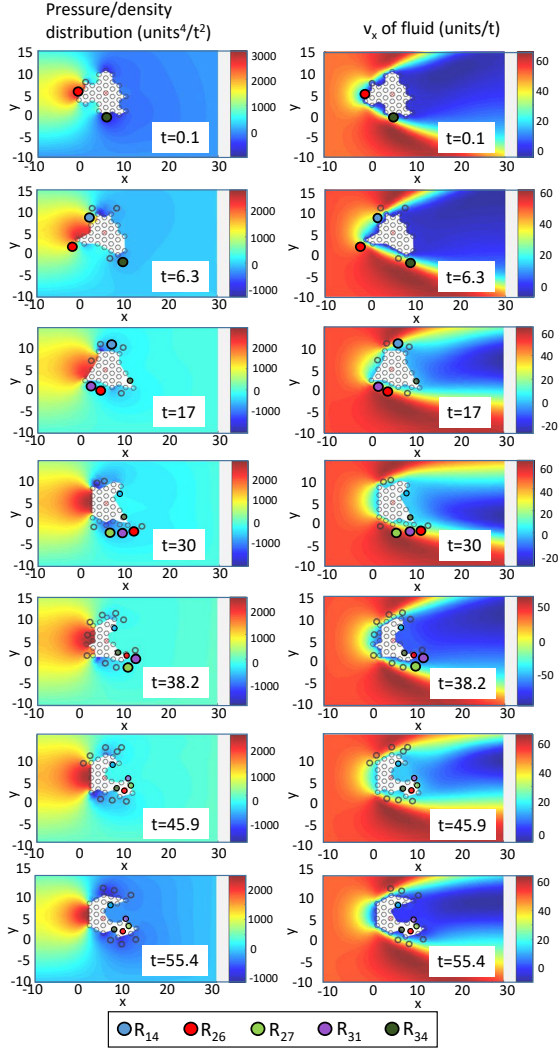
(a) Simulation time-lapse for $N = 35$ in S3, showing the progress of five randomly picked robots (R_{14}, R_{26}, R_{27}, R_{31}, and R_{34},) in G_{35} exposed to a damaging directional stimuli along the x^+ direction.
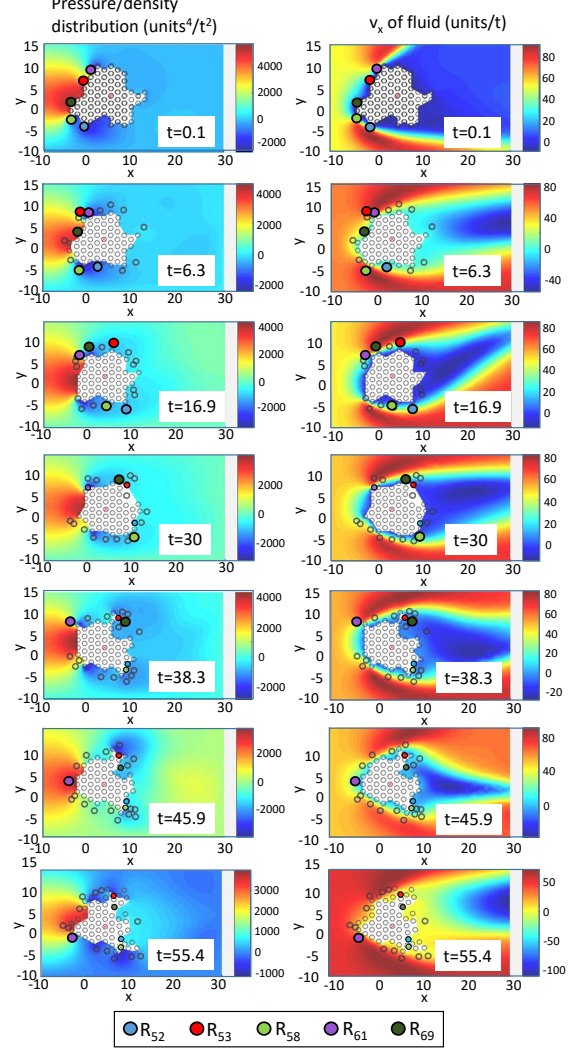
(b) Simulation time-lapse for $N = 70$ in S3, showing the progress of five randomly picked robots (R_{52}, R_{53}, R_{58}, R_{61}, and R_{69},) in G_{70} exposed to a damaging directional stimuli along the x^+ direction.

Figure 3.7. Optimized method comparison for small and large robot group
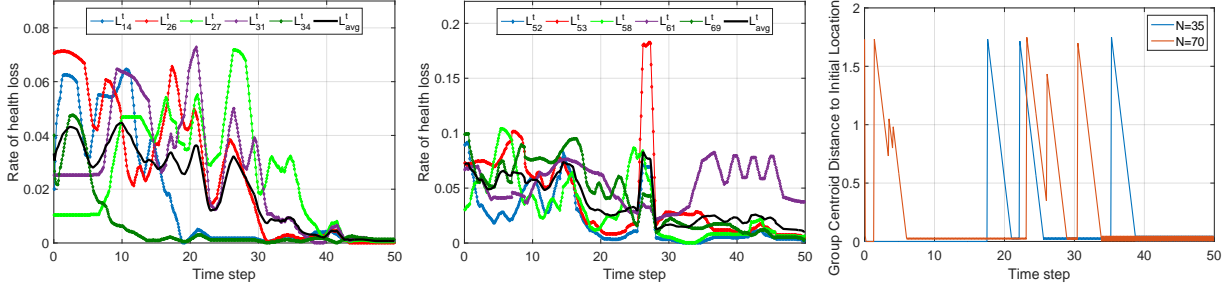
(a) L_i^t for $i \in G_{35}$ with time using the optimized settling method. (b) L_i^t for $i \in G_{70}$ with time using the optimized settling method. (c) Group center from initial location

Figure 3.8. Optimized method comparison of health loss for small and large robot group.

Comparing the time lapse progression of the $N = 35$ and $N = 70$ robot group cases, the following observation could be made. While moving around the flanks and extrema of the group boundary, all robots experienced a sudden increase in L_i^t similar to the observation made in S1. In this region, v_x is at its peak along with very low pressure. The robots experienced the highest health loss rate L_i^t here modeled by (3.1) as opposed to the stimuli-side where v_x is low with very high pressure. As the robots continued to move along the flank, they assessed the optimized settling method condition $L_i^l < L_i^g$ at every local health loss minima encountered to determine if it should settle. For the smaller robot group, the boundary following robots are observed to settle around the trailing ends of robot group corners on the leeward side. As a result, lobe like structures are observed to form at the trailing edges creating a horse-shoe like robot group shape over time. In contrast, the larger robot group of $N = 70$ is observed to create multiple lobes throughout the leeward side as more and more robots settled; the robots are not concentrated on the leading edges on the leeward side suggesting that the optimized settling condition of $L_i^l < L_i^g$ at these locations were not fulfilled. The significant number of the boundary following robots were able to move beyond this local health loss minima towards the estimated global health loss minima. The robot group did not result in an aerodynamic shape over time as observed in S1. The robot group shape remained random with several observable trailing edges forming on the leeward side with the in-between pockets being occupied by the continuously relocating robots.

The trade-off of the proposed optimized settling method not yielding the favorable aerodynamic shape from S1 lies in individual robots losing less health during the relocation

process as some assess the journey to the estimated global health loss minima to be too expensive and settle at a local health loss minimum, i.e. individually robots are able to save health over time. The health saving grows substantially with increasing robot group size that in turn increases the distance to be travelled to the estimated global health loss minima. The effectiveness of this health loss saving trade-off over S1 is substantiated in Section 3.5.4.

With this continuous relocation process, the robot group tended to drift away from the stimuli; an observation consistent with S1 and S2. With the implementation of the distributed robot group center determination and initial location maintenance method from Section 3.4.3, the robot group is observed to return its geometric centroid to the original location of the group. The group center robot is continuously assessed and determined that initiates a group motion towards the original location, while the neighbors match their velocity with the detected initiator. Fig. 3.8c plots the robot group center distance to group initial location distance with time step over the duration of the simulation; with newly determined group center robots, the group center distance to the original location was observed to return to zero every time for both the $N = 35$ and $N = 70$ robot cases. The robot group shape was maintained throughout the process as observed from the time lapse images.

Scalability Analysis of S3

This optimized health loss minima settling method relies on a good estimation of the global health loss rate minima location in order to effectively determine whether to settle or keep moving forward. Therefore, similar to the S1 scenario, S3 yields improved result in the global health loss minima estimation for larger robot groups allowing it to utilize a larger training data set for the estimation process. The relocation process with the optimized health loss rate settling method was repeated for $N = 26$, 57 and 107 in addition to previously presented $N = 35$ and $N = 70$ robot cases with arbitrary formation shapes against the same modeled fluid flow as external stimuli. For each N case, five randomly picked robots R_i on the stimuli side of the group were tracked; $i \in G_{26}$ for $N = 26$, $i \in G_{57}$ for $N = 57$ and $i \in G_{107}$ for $N = 107$ where $G_{26} = \{12, 15, 23, 24, 25\}$, $G_{57} = \{42, 30, 55, 56, 57\}$ and $G_{107} = \{21, 32, 74, 97, 103\}$ respectively. Their health loss rate L_i^t with time corresponding to movement around the boundary is shown in Fig. 3.9a-3.9c.

(a) L_i^t for i $\in G_{26}$ with time.   (b) L_i^t for i $\in G_{57}$ with time.   (c) L_i^t for i $\in G_{107}$ with time.
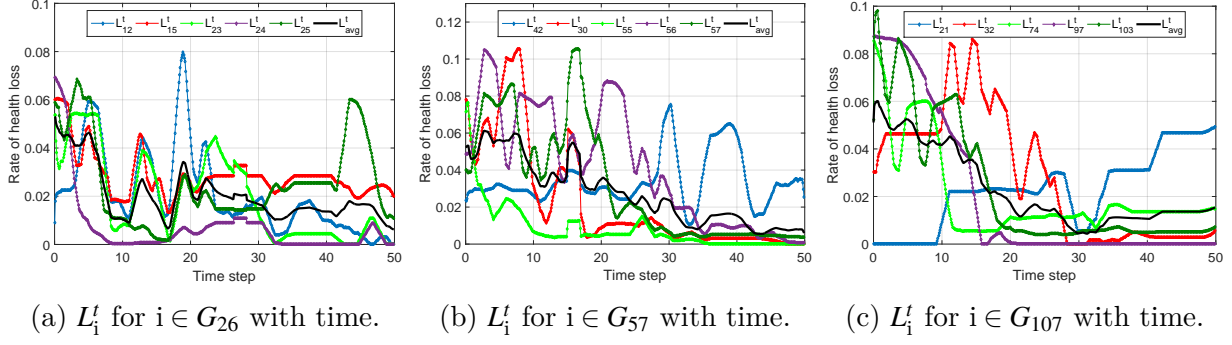
Figure 3.9. L_i^t for the tracked robots in each of the $N = 26$, $N = 57$ and $N = 107$ cases for S3 decreases with time as the robots move from the damaging stimuli side to the leeward side using the proposed GP estimated optimized minima method.

In each case, some of the robots are observed to settle in their optimized settling locations while some remained in the relocation process. However, as the tracked robots made their way from the stimuli side to the leeward side, their respective average health loss rate was observed to decrease over time for all cases of N.

3.5.4   Effectiveness of the Proposed GPML Estimated Settling Methods: S1 vs. S3 vs. S4

The effectiveness of the proposed settling methods is established by comparing the average robot health of the five randomly picked robots in the same robot groups in S1 and S3 with control scenario S4, when encountering the same modeled damaging directional external stimuli. For all the simulation cases of $N = 26$, 35, 70 and 107 in all scenarios, each of the five tracked robots started with full health. We denote the robot health at every time step when allowed to relocate with the global health loss minima as $_gH_i^t$, the optimized health loss minima as $_hH_i^t$ and when not allowed to move as $_nH_i^t$. At every time step for all cases, $_gH_i^t$, $_hH_i^t$ and $_nH_i^t$ deteriorates by the corresponding L_i^t for each robot. The average robot health for the five tracked robots for each N case in S1, S3 and S4 are denoted as $_gH_{avg_N}^t$, $_hH_{avg_N}^t$ and $_nH_{avg_N}^t$ respectively. The results of the comparison are shown in Fig. 3.10.

In S4, $_nH_{avg_N}^t$ for all cases of N deteriorated linearly with time depending on individual L_i^t measurements. For S1, $_gH_{avg_N}^t$ leveled out over time with 12.6%, 5.3%, 16.7% and 14.2% more health than the control case S4 with $_nH_{avg_N}^t$ at $t = 50$, for $N = 26$, 35, 70 and 107 respectively. As more robots relocate behind the initially moved robots in S1 in a continuous process, every

86
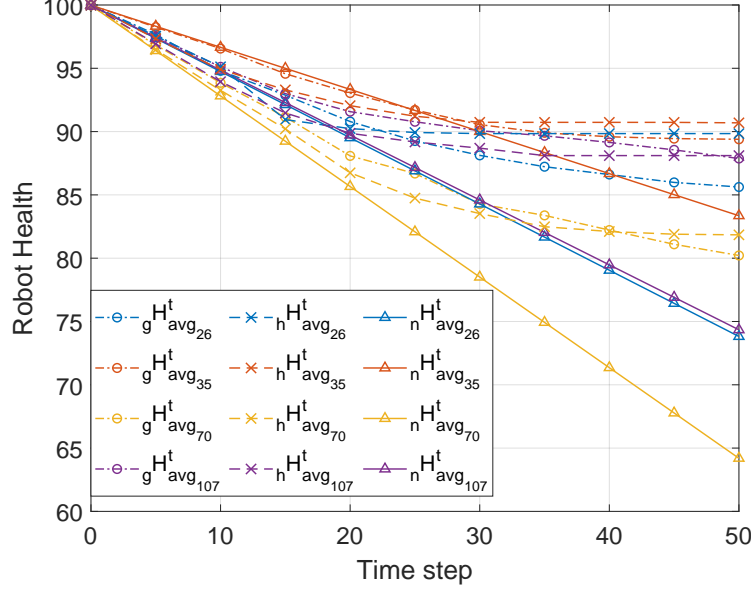
Figure 3.10. The average robot health of tracked robots in all N cases was consistently better for S1 (proposed GP estimated global minima settling) and S3 (proposed GP estimated optimized minima settling) than control scenario S4 over time. The average robot health for all N cases was higher with S3 at time step 50.

robot in the group gets an opportunity to reduce their rate of health loss by relocating to the safest available position behind the group. As a result, the whole group is able to survive together for a longer period of time in the field. However, for S3, $_hH^t_{avg_N}$ leveled out over time with 3.9%, 1.9%, 1.7% and 0.6% more health than the S1 case with $_gH^t_{avg_N}$ at $t = 50$, for $N = 26$, 35, 70 and 107 respectively suggesting further improved average health loss for relocating robots in the long run. However, it must be noted that the optimized health loss rate minima settling method resulted in more frequent relocations by robots in many of the trials depending on the shape of the robot group compared to the global health loss rate minima settling method.

3.6 Conclusion

In this chapter, an Emperor Penguin huddling-inspired multi-robot group survival methodology of surviving a directional damaging external stimuli is proposed. A distributed boundary movement control method is presented that allow robots to move from the stimuli-side to the safest available position on the leeward side without requiring any communication

with each other or prior knowledge of group size or shape. GPML with SM kernel is used to determine the best relocating position for the moving robot based on only stimuli measurements. With this continuous relocation process, the robot group as a whole ensures that no robot remains exposed to the damaging external stimuli for too long; individuals are able to seek safety and shelter behind the group in turns benefiting the entire group in the long run.

4. COLLABORATIVE SHAPE FORMATION

4.1 Introduction

Self-organizing shape formation in multi-robot systems have a wide range of applications ranging from multi-robot navigation, exploring, escorting, rescue missions to developing programmable matter. Mora et al. [26] identified the fundamental problems of the multi-robot shape formation task as, 1) assigning an arbitrary number of robots to goal positions that define the shape and 2) control the robots (positioning, collision avoidance) to establish that formation.

Over the years, a substantial amount of work has been proposed on self-organization in multi-robot systems. We summarize all relevant works from literature in Section 4.2. Most of these studies have assumed individual to be fully aware of either their immediate surroundings or the complete environment of operation using a combination or a variety of sensors; individuals capable of communicating either within a specified radius or throughout the robot group over a communication network. Validation with small robot groups has been achieved with convincing results on commercially available multi-robot platforms such as the E-puck [77], R-One [78], Colias [79] etc. to name a few.

However, when dealing with a large scale robot group (numbering thousands), the complexity of the fundamental problems in multi-robot shape formation identified by Mora et al. [26] and the difficulty of real world implementation of such systems increases exponentially. Individuals suffer from heavy on-board computation processing data from a variety of sensors, increased weight and slow response times [80]. Frequent delays in the required communication network slows down the entire system even further [81]. Additionally, due to their increased individual cost, using thousands of such robots on swarm robot applications has thus remained far from reality [64].

Therefore, the design of a self-organizing shape formation system for a large scale robot group must include the following properties:

- A robust shape representation: The shape to be formed must not dictate the exact location of specific agents within the shape

- Achievable by simple, low cost, low to no overhead bearing agents following simple rules

- Achievable by local communication.

A lot of work in literature has successfully addressed the shape representation requirement, but almost all still falls considerably short on the rest. In this chapter, a fully distributed shape formation methodology is proposed for a large scale multi-robot system consisting of simple individual agents with limited sensing and communication for coordination. By design, inter-robot cooperation allows guiding of neighboring robots towards the shape forming frontier lined with beacon robots that help robots settle to continue the shape formation process, as opposed to a central controller-based robot formation control or search based inefficient methods where robots search for a place to settle in forming the required shape.

4.2 Related Works

Typical work on shape formation has focused on positioning robots in a specified shape and measuring the accuracy of the shape achieved [82]. Oh et al. categorized multi-robot shape formation as either a position, displacement or distance based control problem in [83]. Potential field based approaches using global parameters have been a popular method on directing robots to goal locations over collision-free trajectories [84], [85]. Ikemoto et al. proposed a distributed gradual pattern formation algorithm based on the Turing diffusion-driven instability theory in [86]. Assuming the associated network of a multi-agent system is jointly connected, Zhang et al. showed that collective motion patterns can be obtained without any global beacon or guidance in [87]. Artistic pattern formation with attention to visually appealing trajectories was achieved by Mora et al. in [26]. Numerous other distributed shape/pattern formation approaches have been proposed in literature following consensus control [87]–[99].

Formation control strategies based on relative positions of robots (distances and directions to neighbors) to maintain a shape has been proposed in [84], [85], [100]–[104]. Formation control exclusively using range only distance sensors were considered in [105]–[109].

Approaches assuming the usage of wide-directional camera, laser range finders for local sensing have also been studied in [110]–[114].

A substantial gap exists between large-scale multi-robot conceptual systems and system realization, due to complex individual robot design requirements by most proposed works in literature and their associated costs. Rubenstein et al. proposed the Kilobot platform in [65] to mitigate the problem of high cost of swarm robotics with design simplicity. The design utilized vibration motors to allow translation and rotation over 3 pin legs; an infrared transmitter and receiver mounted under the belly to measure the distance to neighbors and communicate by varying the intensity. Programmable self-assembly of complex two-dimensional shapes with a thousand Kilobot swarm was successfully shown in [64].

4.3 Preliminaries

4.3.1 Shape Representation

We assume an arbitrary geometric shape made up of unit nodes arranged as a structure and represented by a connected graph $\mathscr{G} = (V, E)$, where V represents the set of N nodes and E represents the set of edges connecting neighboring nodes without any self-connectivity following [115]. We represent node connections from node $D_k \in V$ to node $D_e \in V$, $\forall \{k, e\} \in E$ as $_k^e\{r, \theta, \psi\}$, defined as the distance, elevation and azimuth respectively of D_e from D_k relative to the parent node of D_k. The structure of the arbitrary shape can therefore be represented by a modified adjacency matrix X with entries,

$$X(m,n) = \begin{cases} _m^n\{r, \theta, \psi\} & \{m,n\} \in E \\ 0 & \text{else} \end{cases} \tag{4.1}$$

where $m \in \{1, .., N\}$ and $n \in \{1, .., N\}$ denote row and column numbers respectively.

4.3.2 Robot Group Setup

We assume that at time t_0, robot R_i, $i \in \{2, .., N\}$ is randomly placed in a closed 3D environment. All robots are given the shape structure representation matrix X and the

91
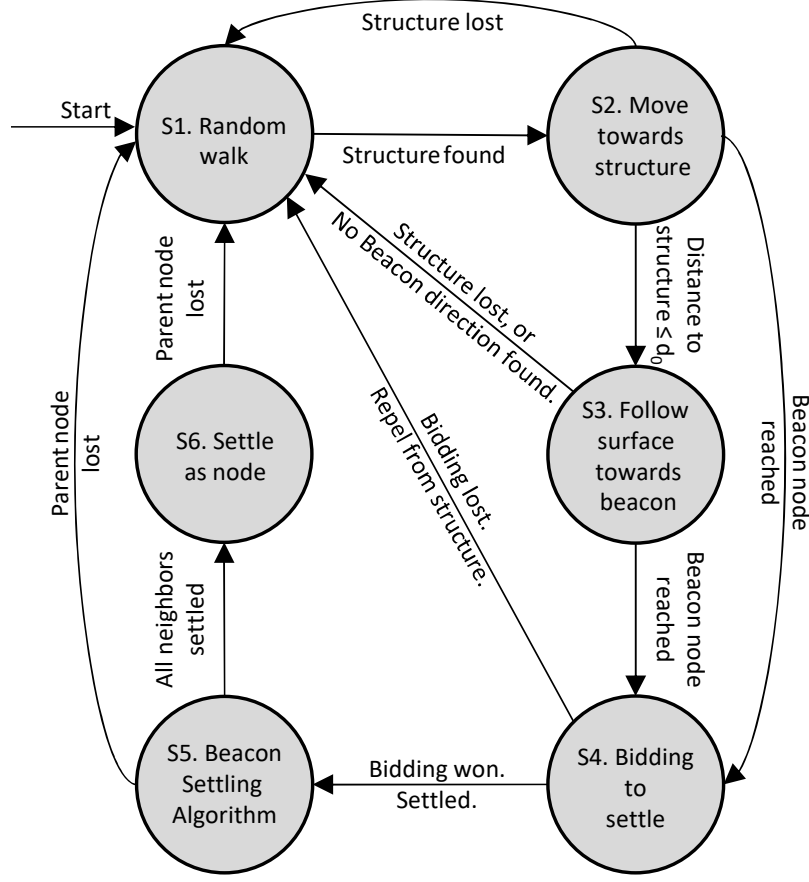
Figure 4.1. Finite State Machine controller. Robot initial state is S1.

distributed self-organizing control law proposed in this paper. Each robot is assumed to have a spherical detection and communication region of radius r_d and r_c respectively. The self-organizing process is started by placing robot R_1 at the starting location of the to-be-formed structure.

At time t, R_i can either be staying in formation ($i \in A$), having detected the formation and moving towards it or moving along the structure surface ($i \in B$) or on random walk ($i \in C$), where A is defined as the set of robots staying in formation, B the set of robots moving towards the formation or along the structure surface, and C the set of robots on random walk.

4.4 Methodology

4.4.1 Finite State Machine for Shape Formation

The shape formation process following the initial robot setup can be implemented as a finite state machine as shown in Fig. 4.1. A description of the operation of this state machine is as follows.

- State S1: Search for shape structure. $R_i, i \in C$ performs random walk in the environment looking for settled robots $R_j, j \in A$. Transitions:

  - $S1 \longrightarrow S2$: if $R_j, j \in A$ found.

- State S2: Move towards structure. $C \leftarrow C \setminus \{i\}$, $B \leftarrow B \cup \{i\}$. The nearest robot $R_j, j \in A$ from R_i is set as the parent robot O_i of R_i with position denoted as o_i. $R_i, i \in B$ is attracted towards O_i. Transitions:

  - $S2 \longrightarrow S4$: if $R_i, i \in B$ reaches surface following distance $||r_i o_i|| \leq d_0$ from parent O_i, where d_0 is the set surface following distance and the surface gradient value of O_i is $b_{O_i} = 0$, suggesting O_i is a beacon.

  - $S2 \longrightarrow S3$: if $R_i, i \in B$ reaches surface following distance $||r_i o_i|| \leq d_0$ from parent O_i, where d_0 is the set surface following distance.

  - $S2 \longrightarrow S1$: if O_i lost for time T_l.

- State S3: Follow surface towards beacon. Robot $R_i, i \in B$ receives surface gradient values from all robots in structure within r_d, $R_j, j \in A$. It moves along the surface towards the direction of minimum decreasing gradient from O_i towards the nearest beacon maintaining distance d_0 from the structure surface. Transitions:

  - $S3 \longrightarrow S4$: if the surface gradient value of O_i is $b_{O_i} = 0$, suggesting O_i is a beacon.

  - $S3 \longrightarrow S1$: if O_i lost for time T_l.

- State S4: Bidding to settle. Robot $R_i, i \in B$ receives its possible node number k from its beacon robot O_i serving as node p and communicates its bidding value ε_i to all other robots within r_d, $R_j \in B$ bidding for node k. Transition:
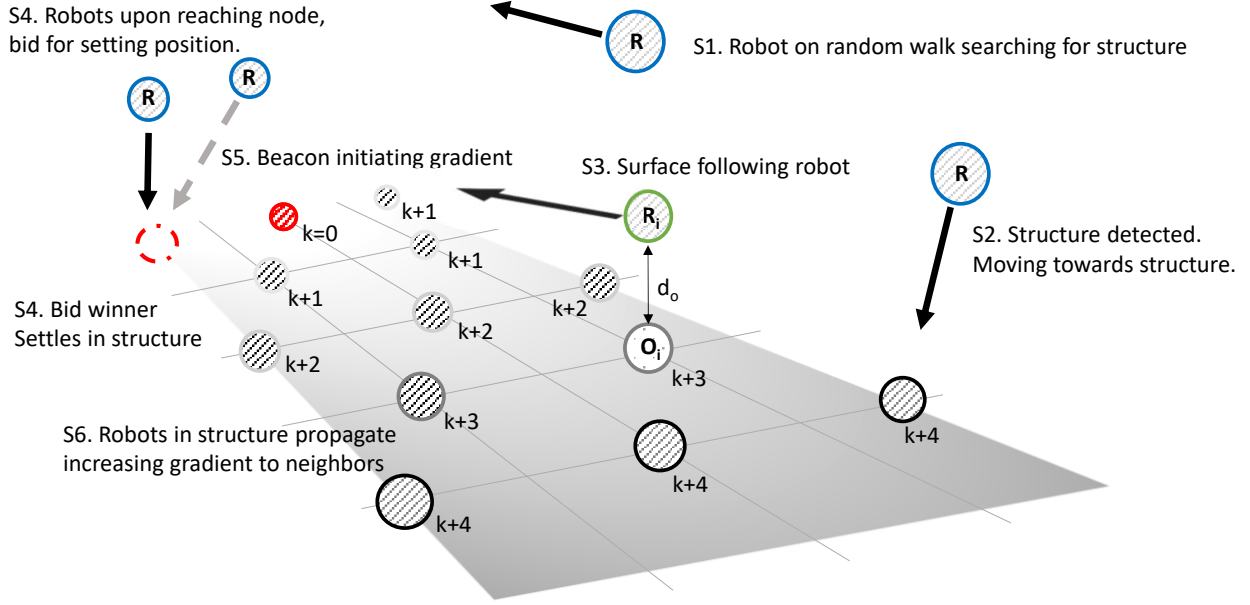
Figure 4.2. Shape structure formation in progress showing surface following motion and node-neighbor interaction.

- $S4 \longrightarrow S5$: if $\varepsilon_i > \varepsilon_j$, $\forall R_j \in B$ within r_d of R_i bidding for node k, communicates to O_i that node k has been settled.

- $S4 \longrightarrow S1$: if $\varepsilon_i <= \varepsilon_j$, $\forall R_j \in B$ within r_d of R_i bidding for node k, or O_i lost for time T_l.

- State S5: Settle neighbors. $B \leftarrow B \setminus \{i\}$, $A \leftarrow A \cup \{i\}$. R_i moves to location ${}_p^k\{r, \theta, \psi\}$ relative to the position of O_i and executes Algorithm 3 to act as beacon for its neighboring robots to settle. Once all neighbors are settled, transitions:

  - $S5 \longrightarrow S6$: all neighbors settled.

  - $S5 \longrightarrow S1$: if O_i lost for time T_l.

- State S6: Settle as node. R_i, $i \in A$ settles in formation. Transitions:

  - $S6 \longrightarrow S1$: if O_i lost for time T_l.

Figure 4.2 illustrates the proposed shape formation strategy with robot state and the surface gradient initiated by a beacon robot.

4.4.2 Surface Gradient Propagation

Robots in S3 move along the surface of the structure towards a beacon robot looking to settle a neighbor. In order to attract surface following robots towards them, beacon robots initiate a gradient that incrementally propagates throughout the structure. The surface gradient generating method is a variant of the previously discussed Barycenter Algorithm in Chapter 3.

We denote the gradient value of robot $R_i, i \in A$ as b_{R_i}. A beacon robot broadcasts its robot ID and an initial gradient value of 0 within its limited spherical communication range with radius r_c. Having received the beacon robot gradient value of zero, all immediate neighbors re-broadcast their robot ID and an incremented gradient value of 1. For multiple propagating gradients received, the minimum gradient value of all neighbors less than or equal to the current broadcast gradient value is incremented and broadcast as the new gradient value in the next time step. The process continues to propagate the incrementing gradient by subsequent neighbors. The continuous gradient propagation process where each robot broadcasts its gradient value in the next time step assessing the gradient values of all its immediate neighbors, can be formulated as,

$$b_{R_i} = \min b_{R_j} + 1, \quad \{j \in A | b_{R_j} < b_{R_i}^{prev}, r_{ij} \le d_0\}, \tag{4.2}$$

where $b_{R_i}^{prev}$ is the gradient value broadcast by R_i in the previous time step, and r_{ij} is the Euclidean distance between robots $i, j \in \{A\}$. This distributed process of generating a surface gradient does not require any fully connected communication network of robots; robots within the forming structure maintaining a set distance of d_0 are able to broadcast and receive gradient values to create the surface gradient that the surface following robots use to navigate along the surface of the forming structure and reach potential beacon robots currently following Algorithm 3 to settle its neighbors. An illustration of the surface propagated gradient from a beacon robot is shown in Fig. 4.2. The controller for surface following robots in S3 are described in Section 4.4.5.

Algorithm 3 Beacon Settling Algorithm

1: procedure (X, k, p)
2:     Communicate to O_i of successful settlement as node k
3:     Set beacon gradient value $b = 0$
4:     for e $= 1 \rightarrow N$ do
5:         if $X(k, e) \neq 0$ then
6:             while Neighbor node e settlement confirmation not received do
7:                 Broadcast $\{i, k, e, b\}$
8:                 if Neighbor node e settled then
9:                     Break

4.4.3 Beacon Settling Algorithm

Upon moving to S5, a robot R_i is aware of its parents and its own node number on the shape structure mapping matrix X denoted as p and k respectively. R_i sequentially settles each of its neighbors following row k of the shape structure mapping matrix having non-zero entries and ignoring column p. The neighbor settling process is summarized in Algorithm 3. R_i sets itself as the beacon ($b = 0$) to propagate its own gradient over the forming structure surface. For every non-zero entry in row k of the matrix X, R_i broadcasts the message $\{i, k, e, b\}$ where i is its own robot index, k and e are its own node ID and the neighbor's node ID on the shape structure mapping matrix respectively, and $b = 0$ is its initiating gradient value that surface following robots may read to detect it has a beacon. Once a robot settles as structure node ID e and communicates that it has settled, R_i moves on to settle its next neighbor following the shape structure mapping matrix X.

4.4.4 Bidding for Node k

Robot R_i in S3 having detected O_i as a beacon receives the broadcasted beacon node and neighbor node number p and k respectively from the beacon. At any given time, more than one robot may reach a beacon. Each robot trying to occupy node k of the structure bids for

the position based on the distance travelled so far and its current distance to the location of node k. The bidding value may be calculated as,

$$\varepsilon_i = \kappa_1 \sum_{t_0+1}^{t} |r_i(\tau) - r_i(\tau-1)| + \kappa_2 ||r_i r_k|| \qquad (4.3)$$

where κ_1 and κ_2 are scalar constants and r_k is the location of the node k determined from the shape structure mapping matrix X and relative position of the beacon node p. All bidding robots within r_d of one another broadcast and receive each other's bids. Robot R_i individually evaluates its own bidding value against the rest to determine if the bid is won or lost. The robot with the winning bid moves in to occupy the node k of the structure by setting constant $\eta = 1$ while the rest return to random walk on the finite state machine after an initial repulsion with $\eta = -1$. Implementation details of η are included in Section 4.4.5 of this chapter.

4.4.5   Robot Interaction and Motion Control

For modeling simplicity, we assume point mass dynamics for all robots without any maneuvering constraints. Robots in sets A and B maintain inter-robot distances using artificial potential U_{ij}, $i,j \in \{A,B\}$ previously established in [70] with an additional attraction term written as,

$$\underset{\forall i,j \in \{A,B\}}{U_{ij}} = \begin{cases} \alpha_{ij}(\frac{1}{2}(r_{ij}-d_0)^2 + \ln(r_{ij}) + \frac{d_0}{r_{ij}}) & 0 < r_{ij} < d_1 \\ \alpha_{ij}(\frac{1}{2}(r_{ij}-d_1)^2 + \ln(r_{ij}) + \frac{d_0}{d_1}) & r_{ij} \geq d_1 \end{cases} \qquad (4.4)$$

where r_{ij} is the Euclidean distance between robots $i,j \in \{A,B\}$, α is a scalar control gain; d_0 and d_1 are scalar constants such that $d_0 < d_1 \leq r_d$. We define d_0 as,

$$d_0 = \begin{cases} d_{AA} & \forall i,j \in A \\ d_{AB} & \forall i \in A, j \in B \end{cases} \qquad (4.5)$$

such that $d_{AA} \leq d_{AB}$, where d_{AA} and d_{AB} are scalar constant parameters defining the inter-robot distances between robots in set A, and inter-robot distances in sets A and B. For State S4, robots are attracted to or repelled from a given relative node location based on bidding that can be formulated as,

$$
U_{r_i r_k} = \begin{cases} \frac{\eta}{2} \alpha_a |r_i r_k|^2 & R_i \text{ in S4} \\ 0 & \text{else} \end{cases} \tag{4.6}
$$

where $r_i r_k$ is the Euclidean distance between R_i and the relative location of the bidding node k in the structure, α_a is a scalar constant and $\eta \in \{-1, 1\}$ for attraction or repulsion of R_i from node location k depending on the bidding outcome. The corresponding control input to maintain the desired distance between robots in sets A and B and in states S2, S4, S5 and S6 is defined as,

$$
\underset{R_i \in \{S2,S4,S5,S6\}}{u_i} = \begin{cases} -\sum_{j \neq i} \nabla_{r_{ij}} U_{ij}(r_{ij}) + \nabla_{r_i r_k} U_{r_i r_k} & 0 < r_{ij} < d_1 \\ 0 & r_{ij} \geq d_1. \end{cases} \tag{4.7}
$$

Robots currently in state S3 of the finite state machine and part of set B move along the structure surface in the direction of detected minimum surface gradient following the control law,

$$
\underset{R_i \in S3}{u_i} = \frac{1}{2} \sum_{\forall (b_{R_j} - b_{O_i}) < 0} |b_{R_j} - b_{O_i}| |r_i \vec{o}_i| \hat{O_i R_j}, \quad \{j \in A | r_{ij} \leq r_d\}. \tag{4.8}
$$

For robots in set C or state S1, random walk is achieved by setting a constant velocity v_r at safe and bounded random elevation and azimuth orientations θ_r and ψ_r without path overlap and avoiding collision.

4.5   Inter-robot Collision and Stagnation Point Avoidance

Robots in sets A and B avoid collision with one another throughout the shape formation process following Eq. 4.4. The safe equilibrium distance of robots already settled is set as d_{AA} and boundary following robots maintain a distance of d_{AB} with robots already in structure.

Boundary following robots have an attractive potential beyond the set safety distance to maintain the safe surface following distance.

Artificial potential based motion control is susceptible to stagnation points where the summation of all affecting potentials is zero resulting in no net movement of the robot. Robots already settled in structure (set *A*) are exempt from this problem. We note the following strategies by robots in set *B* to escape possible stagnation points. Robots in random walk generate a new possible path after a set translation distance. Stagnation points can be escaped over a number of iterations as long as there is an escape path available. Surface following robots on the other hand are prone to stagnation points in a number of unique situations. Eq. 4.8 sums the gradient difference of neighboring robots from the closest node which may result in a net zero control input if the closest node is equidistant from two beacons on opposite sides. In such cases, the surface following robot returns to random walk to generate a new path that allows it to escape the stagnation point. The robot follows the finite state machine to reacquire the structure and follow the surface gradient to the closest beacon.

The proposed surface following method is also robust to robot failures. Robots in structure failing to broadcast their gradient values to surface following robots are treated as not in structure. Therefore, surface following robots move around them following the available gradient values from neighboring robots. In unique failure cases where all neighbors of the closest node robot within the detection range of a surface following robot have failed, the robot is unable to determine a direction of motion. In such cases, the resulting zero potential forces the surface following robot to return to random walk and reacquire the structure following the finite state machine. Therefore, the motion of surface following robots is concluded to be always in the direction of the nearest beacon even in the presence of possible stagnation points that may arise within the forming structure of the given shape.

By design the surface following process requires a continuously differentiable surface. The system is unable to move around sharp edges where the minimum gradient direction maybe aligned with an opposing force from the nearest robot. However, we note here that the system may still be applicable follow discontinuous surfaces with small exterior angles

around the edge. Simulation results verifying this assessment has been included in Section 4.6.

4.6   Validation

The proposed shape formation strategy is validated by forming shapes with continuously differentiable and discontinuous surfaces with small exterior angles, both in 2D and 3D forms. The proposed method utilizing surface gradient propagation allows surface following robots to independently identify their motion direction towards the nearest beacon. All robots are randomly placed in a $400 \times 400 \times 400$ 3D space for all simulation cases with an initial height of 10 in the z direction. Robots are assumed to follow point mass dynamics and free to move in any direction with the simulation parameters set as $r_d = 40$, $d_1 = 40$, $d_{AA} = 30$, $d_{AB} = 30$, $\alpha = 0.1$ and $\alpha_a = 0.6$, and random walk bound parameters as $v_r = 0.8$, $\theta_r = 0$, $\psi_r = \frac{\pi}{2}$. The formation process is started by placing the first node of the shape structure at the initializing location which acts as the first beacon.

4.6.1   2D Shape Formation: Circle and Pentagon

For analysis purposes, we consider simple shapes such as a circle (continuously differentiable boundary) and a pentagon (discontinuous boundary with small exterior angle) for the validation of the proposed strategy forming 2D shapes. The time-lapse simulation results for a system of $N = 30$ robots forming the circle and pentagon shapes are shown in Fig. 4.3.

At initial time $t = 0$, the initiating node is placed that acts as the first beacon following Algorithm 3 attracting neighboring robots on random walk to settle and start the shape formation process. With more and more robots settling, the circle and pentagon shapes are observed to form over time from two ends until the last robot is attracted in place connecting the two ends to form the closed shape. Robots acting as beacon are highlighted with red circles. Robots detecting the forming shape are attracted to the nearest robot already in the formation; boundary following robots follow the generated gradient from the beacon robots along the length of the formed structure. The color scheme of the robots currently in structure illustrate their broadcasted gradient values; beacon robots highlighted in red

circles have a gradient value of zero while the propagated gradient reached as high as 15 and 16 on the far end of the forming structure towards the end of the simulation for the two cases respectively.
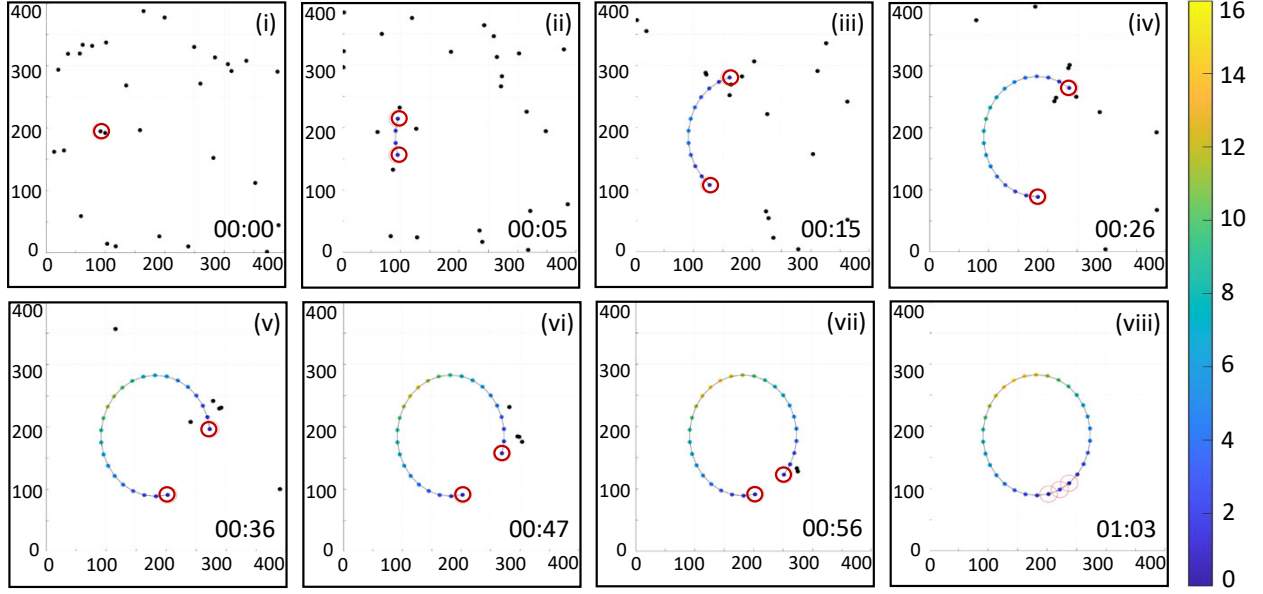
(a) 2D circle shape formation with $N = 30$ robots.
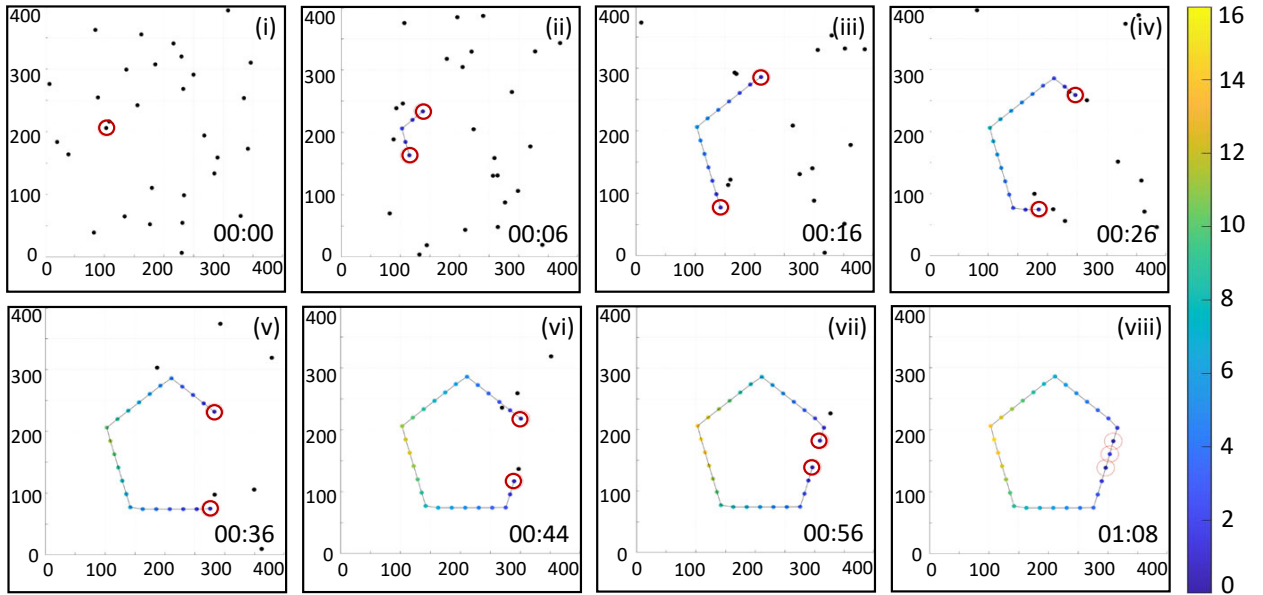
(b) 2D pentagon shape formation with $N = 30$ robots.

Figure 4.3. 2D shape formation using $N = 30$ robots.
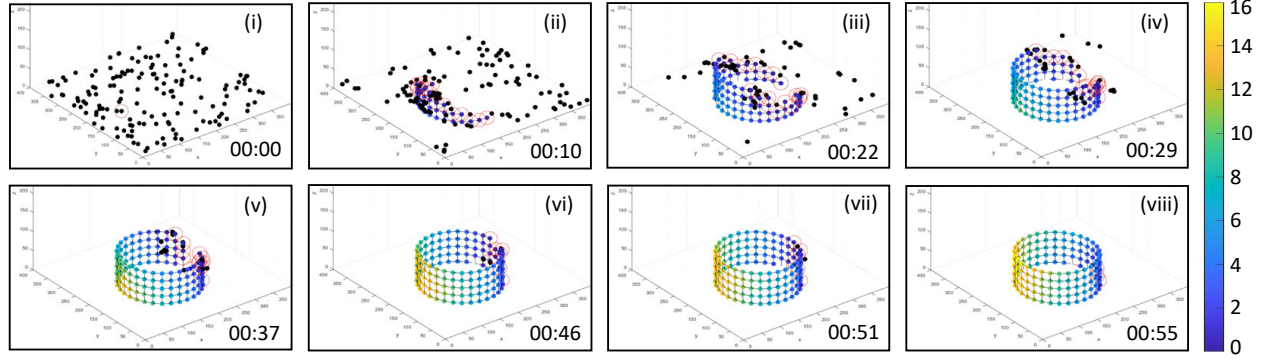
(a) Cylindrical shape formation with $N = 150$ robots.
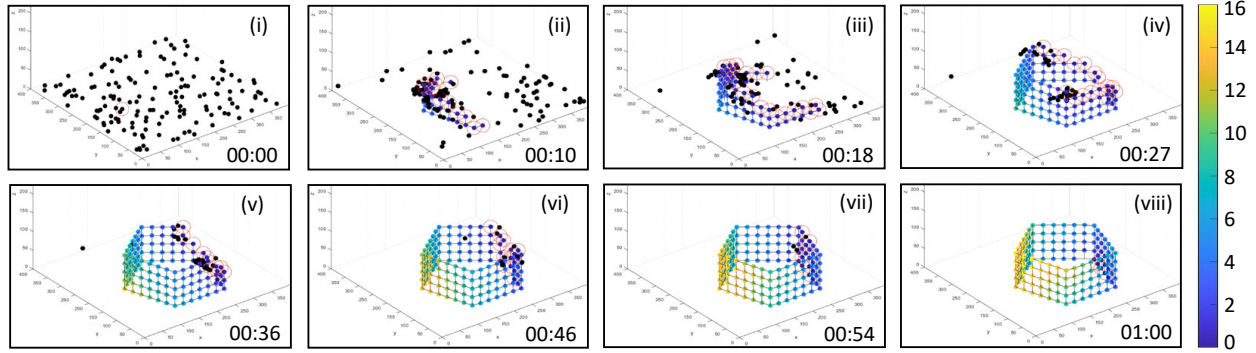
(b) Pentagonal prism shape formation with $N = 150$ robots.

Figure 4.4. 3D shape formation using $N = 150$ robots assuming point mass dynamics. The proposed method successfully constructed shapes with convex continuously differentiable and discontinuous surfaces.

4.6.2   3D Shape Formation: Cylinder and Pentagonal Prism

The same initial simulation setup was repeated for $N = 150$ robots to create a cylinder and a pentagonal prism having a circular base and a pentagonal base with 30 robots respectively to validate the 3D shape formation process. The time lapse images of the shape formation process are shown in Fig. 4.4. With the initiating robot placed as the first beacon for each case, neighboring robots on random walk were attracted to start the shape's structure formation process similar to the 2D simulation cases. After subsequent bidding rounds robots are observed to settle at neighboring nodes and the corresponding structures are observed to take shape over time. The propagated gradient along the surface of the forming structure is visualized by the color scheme where the beacon robots are seen in blue with a gradient value of zero while the robots in structure on opposite ends reached a gradient value as high

(a) Top view

(b) Isometric view
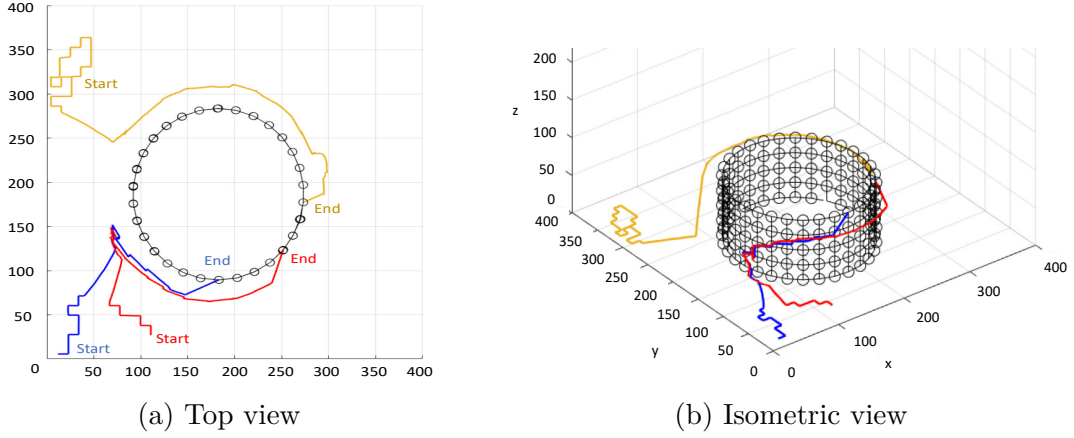
Figure 4.5. Surface following paths of **3** randomly picked robots forming the 3D cylindrical shape.

as **16** over time shown in yellow. All robots successfully followed the proposed distributed finite state machine controller to form the respective 3D shapes.

Figures 4.5 and 4.6 plot the paths taken by **3** randomly picked robots in their corresponding cylinder and pentagonal prism shape formation process. The robots are initially on random walk and are attracted to a robot detected to be in formation broadcasting a gradient value. Once within surface following distance, the robots are observed to successfully follow in the minimum surface gradient direction to reach their respective beacons. Since surface following is a dynamic process where the surface is constantly changing with more and more robots settling, robots are observed to move inside the enclosed structure at times as seen in the pentagonal prism formation case and successfully follow the concave boundary to reach its settling node. Paths observed to be present over the structure robots (blue and yellow) in top view of the pentagonal prism formation were taken by robots before levels **4** and **5** were formed in the structure.

4.6.3 Discussion

The proposed distributed shape formation process includes: 1) individually assessing the surface gradient to determine the direction of the forming structure, 2) individually determining node settling consensus in structure after receiving all bids, 3) systematically guiding one neighbor at a time as a beacon to form the structure with local communication

(a) Top view   (b) Isometric view
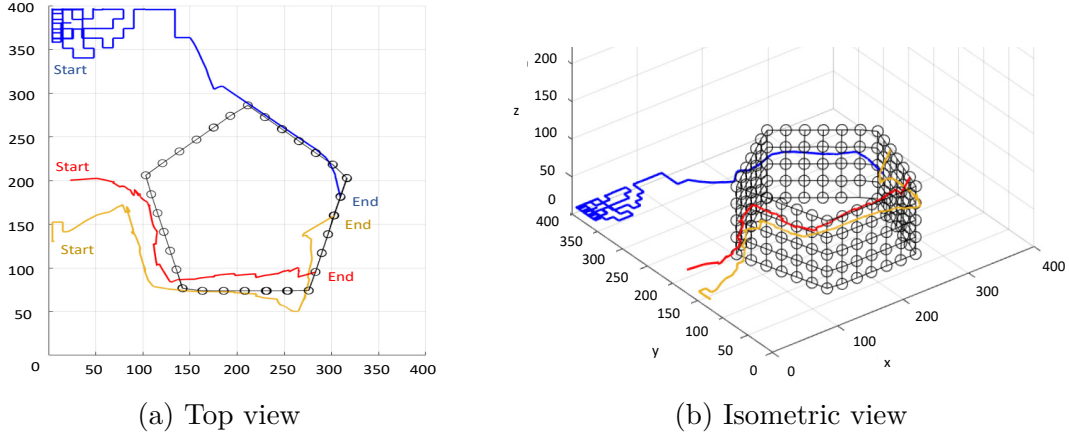
Figure 4.6. Surface following paths of 3 randomly picked robots forming the 3D pentagonal prism shape.

only. The simulation results presented conclude the validity of the proposed strategy in effectively forming simple 2D and 3D shapes. The proposed method is scalable to form the structure of a given shape assuming adequate number of robots are available in the system.

The surface following process in the shape formation strategy is specifically designed for continuous surfaces without any sharp edges in the structure. However, the system was observed to be robust to edges with small exterior angles; shapes such as the pentagon and pentagonal prism were successfully formed in all trials. We note here that the system failed to form structures for shapes such as rectangles and rectangular prisms, where the direction of minimum gradient either could not be determined or could not be followed by surface following robots with their nearest structure robot being the edge. Even if the edge continued on the other side with the minimum gradient attracting the surface following robot, the nearest node at the edge repelled the robot to remain stuck at a stagnation point in such cases. We conclude here that further investigation must be made in determining the maximum allowed exterior angle of surface edges. The proposed methodology could be improved by formulating the motion of surface following robots to independently move around sharp edges to the other side. For our current design, we conclude that shapes with structures requiring sharp edges or corners must be rounded with a higher robot density such that a continuous surface could be achieved for the surface following process.

104

Following the simulation results presented, a large number of robots were observed at times to bid for specific nodes during the shape formation process. The proposed method was successfully able to coordinate distributed robot settling without any failure cases. The proposed system yielded fairly efficient paths taken by each robot during their motion along the structure surface following the minimum gradient to reach the beacon robots. We stress here the importance of this gradient following method as opposed to fixed motion patterns such as raster scanning along aligned robots, helical motion of surface following robots in the vertical direction or random motion to eventually reach a beacon robot looking for a neighbor to settle; although, the fixed motion methods may require minimal computation and less or no communication in determining motion direction, the paths taken by the robots would likely be highly inefficient in comparison without a sense of how and where the structure is currently forming.

Since the proposed system utilizes a completely distributed process where each robot determines its own action based on received communication and observations of neighbors, the system is concluded to be robust to robot motion failures; since any position in the structure may be taken by any robot, the shape formation process will proceed and complete with the remaining robots as long as their paths are not blocked by disabled robots. Robots in motion would simply avoid collision with the disabled robot and continue the shape formation process. The simulation was repeated for a special case where clusters of robots in structure broadcasting their propagated gradient values were disabled to simulate their failure cases. Surface following robots were observed to simply move around these failed robot clusters without any broadcasted gradients; the failed robots were treated as robots not in structure and therefore no surface was present to follow. Special cases of stagnation points were also validated where a surface following robot was unable to find a motion direction when its nearest node was broadcasting but all its neighbors were simulated to fail. Following the stagnation point avoidance criteria in Section 4.5, the surface following robot simply repelled away from the node to random walk to escape and find another surface robot still broadcasting. However, we note here that the proposed system is unable to account for beacon robot failures to settle a neighbor that is not accounted for by any other beacons in the vicinity.

4.7   Conclusion

In this chapter, we present a local communication based cooperative self-organizing strategy in multi-robot systems to form complex prescribed shapes. A finite state machine with potential field based motion control is proposed depending on the states of robots. Simulation results forming 2D and 3D shapes validate the proof of concept.

5. COLLABORATIVE OBJECT TRANSPORTATION

The material in this chapter of the dissertation is partially based on the following submitted paper currently under review. The content has been added with the consent of all co-authors of the paper.

- "Distributed Multi-robot Arbitrary Object Transportation with Pushing Surface Identification and Model-based Pushing Effort Regulation," T. Mina, S. S. Kannan, W. Jo, S. Luo, G. B. King and B.C. Min, IEEE Transactions on Systems, Man and Cybernetics: Systems. (Under Review)

5.1 Introduction

Object transportation by robotic systems has a rich potential for application in warehouse logistics, bomb disposal, path clearing of obstacles in search and rescue, evacuation scenarios, and the construction industry etc. Given the variety of objects involved in these applications in terms of size, shape, and properties, multi-robot teams benefit the system in such cases providing redundancy in enabling reconfiguration, distributed sensing and action at scales that would be impractical or expensive with a single unit [116]. Multi-robot strategies on the other hand introduce its own set of challenges of coordinating multiple units in the application process. The object transportation method proposed in this chapter is designed to be salable for any number of robots, but also presents the advantages of cooperation between agents in improving efficiency of the transportation process.

Multi-robot object transportation proposed in literature can be broadly classified into caging/grasping, towing and pushing strategies. Caging involves the object being trapped within a multi-robot formation and transported by controlling the robot formation [117], [118]; robotic manipulator based object grasping has been proposed based on the caging principle of trapping the object within the end-effector prongs for transportation and/or manipulation [119]–[121]. Object manipulation by a single robotic agent have also been proposed in [122]. Caging and grasping strategies suffer from a minimum number of robot requirement to trap the object, often requires graspable features for manipulation and are limited to convex shapes. Towing requires attachable points on the object and involves
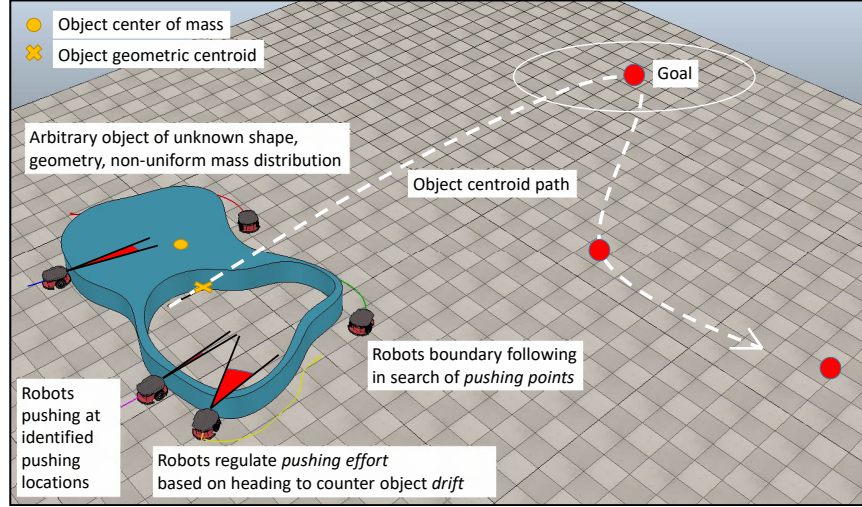
Figure 5.1. Proposed multi-robot arbitrary object transportation.

the object being pulled for manipulation usually by cables [123]–[125]. In this chapter of the dissertation, we are interested in the pushing strategy that involves robots collectively exerting pushing forces on the object without being physically attached to the object or constrained within any formation. The process involves a significant amount of physical interaction to align applied forces and is significantly more challenging if the object of interest is of unknown shape, size, mass, and mass distribution. However, we emphasize that pushing strategies do not require attachable points on the object and allows versatility and robustness in terms of robot coordination, object motion correction, and computation requirements.

Although a substantial amount of research on pushing-based multi-robot object transportation has been proposed over the years, most of these studies have remained confined to transporting simple convex shapes, assuming known object properties. Furthermore, robot contact with object to initiate pushing without any physical damage to the object have never been considered in the strategy formulation. A representative summary of all relevant work from literature on multi-robot object transportation is provided in Section 5.2.

The underlying inspiration of the proposed collective object pushing method lies on observations made in how two or more human beings coordinate transporting an object by pushing. Pushers individually identify possible pushing surfaces and engage in pushing. Effort or force applied is regulated either by direct communication or balancing the applied effort with others as a reaction to the resulting motion of the object, such that the resultant

motion of the object is towards the intended direction with minimal rotation. This cooperation between multiple pushers allow the object to maintain a steady and fairly efficient path towards its goal. We note here that in certain situations individuals may be pushing with a much higher effort or force over the rest, but the process is continued for the benefit of the overall team's performance in transporting the object as efficiently as possible.

Analogous to this cooperative behavior in humans, we propose a scalable multi-robot pushing-based strategy of transporting an object of unknown and/or changing shape, size, mass, and center of mass properties to a predefined goal location without any prior knowledge about the object or the number of robots involved in the transportation process, that is robust to imprecise contact and non-uniform friction between contacting surfaces. Robots rely on individual assessments in order to:

- identify potential pushing surfaces on the perceived object boundary within its field-of-view (FOV) and initiate pushing without damaging the object, and

- regulate their pushing effort based on a proposed model relying on resulting object behavior such that their combined action creates a resultant motion of the unknown object in the intended direction,

without any prior knowledge of the object. Each individual actively reacts to changes in the object's behavior, ensuring it is not lost from its FOV, unintended collision with the object is avoided, and robots do not obstruct the object's motion towards the goal; inter-robot collisions are also avoided, and robots currently in the act of pushing are not affected by robots still searching for a potential pushing location. A rendition of the proposed object transportation method is presented in Fig. 5.1.

5.2   Related Work

One of the pioneering object transportation studies by pushing was proposed in [126] showing that a box could be transported by a group of robots without differentiating between each robot; stagnation point recovery strategies were later included in [127]. Goal occlusion has been identified as one of the fundamental problems in pushing-based object transportation [128] method. A watcher-pusher heterogeneous robot group approach was

109

initially proposed in [129] as a solution, where watcher robots track object and goal locations coordinating the pushing robots. Transport strategies based on exclusively the pushing method have since been proposed in [130]–[133] that suffers from goal occlusion when robots position themselves behind objects to push. An alternative approach to object pushing specifically taking advantage of goal occlusion was recently proposed in [134], where e-puck robots push with a constant force when the object occludes its vision of the goal. This simple method allowed object transportation towards a set goal without using any form of communication and was later extended to transporting objects to moving goal locations in [135]. Goal occlusion-based methods can produce relatively efficient object paths for simple shaped objects with relatively perpendicular boundary regions to the direction of the occluded goal; however, its path efficiency can drastically fall for complex shapes on the goal occluded side of the object, where the robots may start to push resulting in the object drifting wide away from the goal location. Therefore, identification of correct pushing surfaces on the goal occluded side of the object is of significant importance in maintaining an efficient path for objects with complex shapes.

Pushing strategies have often incorporated force feedback in their object manipulation process. Alkilabi et al. proposed a multi-robot group each equipped with optic-flow sensors whose readings were used to distinguish whether a robot's pushing force contributed to object motion [130]. Position and force control for object path keeping has also been proposed in [136]. Manipulator systems making use of force control in object manipulation include [137], where force control provides the benefit of preventing accumulation or application of large forces that could potentially damage the object or the robots themselves. Centralized methods of multi-robot coordination have also been proposed in [131], where a central computer directs robots to pushing locations and determines the pushing force magnitude. Centralized approaches suffer from lack of fault tolerance characteristics and limited field implementation. A decentralized leader-follower approach of object transportation with force feedback has been proposed in [138] requiring no communication, where the follower robots synchronize their applied force direction with the leader who guides the fleet towards the goal. Numerous purely analytical approaches to object pushing have been proposed, including a contact-preserving push plan for a point-sized pusher and a disk-shaped object [139],

[140], a hierarchical approach to planning sequences of non-prehensile and prehensile actions [141], and a rapidly-exploring random tree for planning pushing actions on a polyhedron by a robot [142]. Data-driven approaches have also been investigated in literature including estimation of friction centers based on object motion observations by a robot [143], perception of everyday objects by robotic systems for manipulation [144], and development of planar pushing models to predict the most likely outcome of a push and its expected variability [145]. However, purely analytical approaches are limited by their own assumptions and often do not take into account the stochastic nature of pushing [146], and data-driven learned models are specific to objects and materials [147]. Although numerous other prior works have been proposed in force control in object transportation, very little work has been done to address force application requirements in tandem with a fully distributed robot coordination strategy for object transportation [148].

Our proposed work bridges the gap in identifying viable pushing surfaces given an unknown object of arbitrary shape, size, mass, and center of mass based on individual assessment of the object within the limited FOV of any robot, and developing a model-based pushing force regulation method to ensure the object transportation heading is directed towards the goal regardless of object mass distribution and external disturbances. Although the robots operate over a fully connected communication network sharing their heading error during pushing, we stress the distributed nature of our proposed method as pushing surface identification and individual pushing effort regulation are designed to be based on individual assessments of each robot only.

5.3   Methodology

We define the object transport problem as follows. A bounded planar environment contains an arbitrary shaped object O of unknown mass and mass distribution that is to be transported to a set goal location $g \in \mathbb{R}^2$. N identical robots are placed within the environment to transport the object by pushing. Each robot $R_i, i \in \{1, .., N\}$ with position and orientation/heading defined as $r_i \in \mathbb{R}^2$ and $\pi \geq \theta_i > -\pi$, is assumed to have a circular FOV with a detection radius of r_d and is aware of the direction towards the goal location g defined as $\theta_{i,g}$ relative to the local frame of robot R_i at all times.

Definition 5.3.1 Pushing effort of a robot is defined as a unit-less measure of applied pushing force relative to the pushing ability of the robot platform. It is regulated based on individual and the collective heading error of all robots during pushing to ensure the object is pushed in the intended direction.

Robots relocate to a new pushing location if the required pushing effort exceeds its own ability. Details of the proposed model-based pushing effort regulation method are provided later in Section 5.3.2.

5.3.1 Finite State Machine for Object Transportation

The object transportation process following the initial robot setup can be implemented as a finite state machine as shown in Fig. 5.2 with a conceptual illustration shown in Fig. 5.3. At initial time, all robots search for the object with random walk at state $S1$. A description of the operation of this state machine is as follows.

- State S1: Search for object. R_i in $S1$ performs random walk in the environment avoiding collision and looking for the object O. The set of detected boundary points of object O within the FOV of R_i is recorded as set V_i as ordered pairs of the distance and its relative direction from R_i. The nearest boundary point of O from R_i is therefore determined as $\{o_i, \theta_{i,o}\}$, where o_i is the minimum detected distance in V_i and $\theta_{i,o}$ is the relative direction of o_i from R_i. Transition:

  - $S1 \longrightarrow S2$: if o_i found.

- State S2: Move towards object O. R_i in $S2$ translates towards o_i to reach a defined boundary following distance d_s. Transitions:

  - $S2 \longrightarrow S3$: if $|\overrightarrow{r_i o_i}| \leq d_s$ for R_i in $S2$.
  - $S2 \longrightarrow S6$: if o_i lost from FOV.

- State S3: Follow object boundary until a pushing surface is detected. Robot R_i in $S3$ determines the collective heading angle error of all robots in $S5$ as, $\theta_{net} = \sum_{i=1,R_i \text{ in } S5}^{N} \theta_{i,g}$, where $\theta_{i,g}$ is the heading angle error of R_i when pushing in $S5$, to set $\eta = \text{sign}(\theta_{net})$.

112
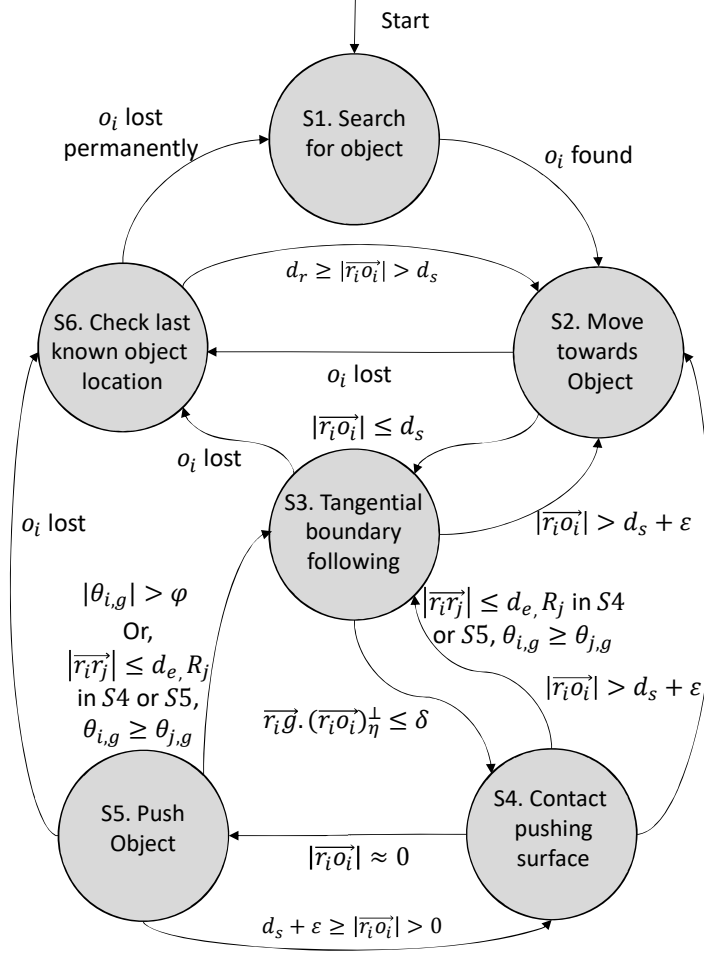
Figure 5.2. Finite state machine controller with initial state $S1$.

η determines the direction of tangential boundary motion at a distance d_s from the nearest detected point on the object o_i defined as $(\widehat{\overrightarrow{r_i o_i}})^{\perp}_{\eta}$. During boundary following, R_i assesses $\widehat{\overrightarrow{r_i g}} \cdot (\widehat{\overrightarrow{r_i o_i}})^{\perp}_{\eta}$ looking for a pushing surface point, where $\widehat{\overrightarrow{r_i g}}$ is the unit vector from R_i to the goal g. Transitions:

- $S3 \longrightarrow S2$: if $|\overrightarrow{r_i o_i}| > d_s + \varepsilon$ where ε is a defined small tolerance distance.

- $S3 \longrightarrow S4$: if $\widehat{\overrightarrow{r_i g}} \cdot (\widehat{\overrightarrow{r_i o_i}})^{\perp}_{\eta} \leq \delta$ detected for $\delta \approx 0$ with g obstructed from R_i by O, a viable pushing surface point is reached.

- $S3 \longrightarrow S6$: if o_i lost from FOV.

- State S4: Contact pushing surface at $\boldsymbol{o_i}$. Robot R_i in $S4$ rotates towards the object and approaches the object surface at the determined pushing point o_i and makes a perfectly

inelastic collision with the object; i.e. collision with a coefficient of restitution, $e = 0$.
Transition:

- $S4 \longrightarrow S2$: if $|\overrightarrow{r_i o_i}| > d_s + \varepsilon$.

- $S4 \longrightarrow S3$: if $|\overrightarrow{r_i r_j}| \leq d_e$, R_j in $S4$ or $S5$ with $|\theta_{i,g}| \geq |\theta_{j,g}|$, where d_e is a set inter-robot safety distance.

- $S4 \longrightarrow S5$: if $|\overrightarrow{r_i o_i}| \approx 0$.

- State S5: Push object at $\boldsymbol{o_i}$ regulating effort. Robot R_i in $S5$ pushes the object at the determined pushing point o_i with a pushing effort magnitude defined as $\rho_5 = f(\theta_{net}, \theta_{i,g})$, (see Section 5.3.2) in the direction of the object goal position g, while $\theta_{i,g}$ is bounded within $[-\phi, \phi]$. Transition:

  - $S5 \longrightarrow S3$: if $|\theta_{i,g}| > \phi$ or $|\overrightarrow{r_i r_j}| \leq d_e$ R_j in $S4$ or $S5$ with $|\theta_{i,g}| \geq |\theta_{j,g}|$ or no net motion of object with $\theta_{net} \approx 0$ (possible stagnation point).

  - $S5 \longrightarrow S4$: if $d_s + \varepsilon > |\overrightarrow{r_i o_i}| > 0$.

  - $S5 \longrightarrow S6$: if o_i lost from FOV.

- State S6: Check last known direction for object O. In each state $S2$, $S3$ and $S5$ robot R_i records the last known direction of o_i as $\theta_{i,o}^{prev}$. R_i in $S6$ rotates towards the last known direction $\theta_{i,o}^{prev}$ and translates up to distance r_d to reacquire the lost object O. Transition:

  - $S6 \longrightarrow S1$: if o_i lost permanently.

  - $S6 \longrightarrow S2$: if $r_d \geq |\overrightarrow{r_i o_i}| > d_s$.

During boundary following in $S3$, if R_i encounters a robot in $S5$ on its path, it treats the robot in $S5$ as part of the object and continues to follow around its boundary. However, the transition to $S4$ is temporarily disabled until o_i is reacquired.

When object O is far away from g, $\theta_{i,g}$ remains small with changes in $||r_i - g||$. Closer to g, $\theta_{i,g}$ changes rapidly and hence its defined bounds $[-\phi, \phi]$ determine how frequently robots will relocate. The constant ϕ must be chosen as small as possible such that θ_{net} remains close
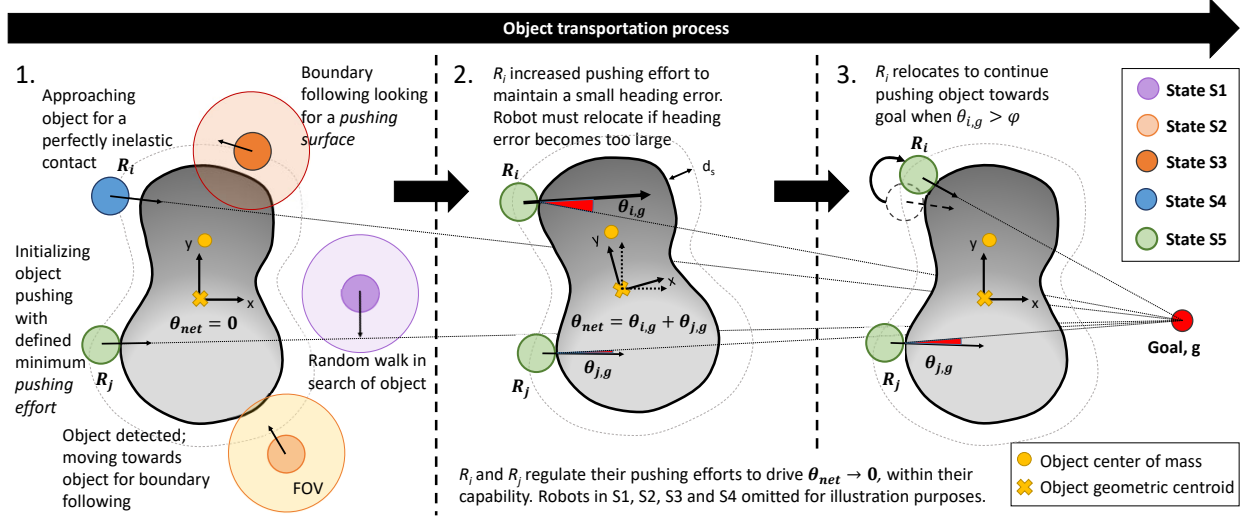
Figure 5.3. Conceptual image of the proposed multi-robot object transportation process for objects with unknown geometric centroid and center of mass (heavy and light ends illustrated by darker and lighter shade). Robots identify pushing points with zero heading error ($\theta_{i,g} \approx 0$) and continue to regulate their individual pushing efforts and relocate if necessary to keep their collective heading error within predefined bounds.

to zero after transient. Robot anti-wheel slip capabilities in achieving calculated pushing effort must also be considered when choosing ϕ.

5.3.2   Robot Interaction and Motion Control

A potential field approach [149] is used to generate the movement vectors of robot R_i at each defined state of the proposed finite state machine controller. The set of control inputs u for each robot R_i in each state is defined as follows:

$$u_{S1} = \rho_1 v_m \widehat{\overrightarrow{r_{i,rand}}} \tag{5.1}$$

$$u_{S2} = \rho_2 |\overrightarrow{r_i o_i}| \widehat{\overrightarrow{r_i o_i}} \tag{5.2}$$

$$u_{S3} = \rho_3 (|\overrightarrow{r_i o_i}|)(\widehat{\overrightarrow{r_i o_i}})^{\perp}_{\eta} + \frac{\rho_2}{2}(|\overrightarrow{r_i o_i}| - d_s)\widehat{\overrightarrow{r_i o_i}} \tag{5.3}$$

$$u_{S4} = \rho_4 (|\overrightarrow{r_i o_i}|)\widehat{\overrightarrow{r_i o_i}} \tag{5.4}$$

$$u_{S5} = \rho_5 v_m \widehat{\overrightarrow{r_i g}} \tag{5.5}$$

115

where $\overrightarrow{r_{i,rand}}$ is a random unit vector with direction defined within $\pm 45^o$ of θ_i and updated every 2 s of operation; $0 < \rho_1 \leq 1$, ρ_2, ρ_3 and ρ_4 are constants. The control input for $S6$ may be defined as a constant attractive potential in the direction of $\theta_{i,o}^{prev}$ with gain constant ρ_6 for a travel distance of up to r_d.

u_{S2} and u_{S4} are based on attractive potentials to drive robot R_i towards the detected nearest boundary point o_i. In $S2$, R_i must reach the defined boundary following distance faster than the translation of the object such that the detected boundary point of the object within its FOV is not lost; and in $S4$, R_i must move faster than the translation of the object and make contact with the identified pushing point on its surface before it is lost following any resultant motion of the object due to the collective effort of other pushing robots. Therefore, the system must be tuned to reflect $\rho_4 > \rho_2 > \rho_5$.

u_{S3} sets the motion of R_i on a tangential path around the object boundary in the direction of η. The first term represents tangential boundary following, while the second term allows distance correction from the object boundary to maintain the set distance of d_s. We set $\rho_2 \geq \rho_3 > \rho_5$ for smooth boundary traversing in non-convex boundary regions. We constraint each robot with a maximum linear velocity v_m and rotational velocity ω_m.

Pushing Effort Regulation

When a robot transitions from state $S4$ to $S5$, it is initially positioned in contact with the object with its heading aligned with the goal location. Without any prior knowledge of the object centroid or center of mass, it starts to push with a minimum defined effort in the hopes that other robots are present or will position themselves to balance the rotational moment of object O. Individuals constantly monitor their individual heading error from the goal location $\theta_{i,g}$ and the collective heading error of all robots in $S5$ defined as θ_{net}. If $\theta_{i,g}$ and the collective heading error are either both positive or both negative, robot R_i linearly increases its pushing effort with its heading error $\theta_{i,g}$ in the hope of driving the collective error to zero. The proposed pushing effort model defined in terms of ρ_5 can therefore be written as,

$$\rho_5 = \max(0, \text{sign}(\theta_{net}) \frac{2\alpha}{\pi} \theta_{i,g}) + \frac{\alpha}{2} \tag{5.6}$$
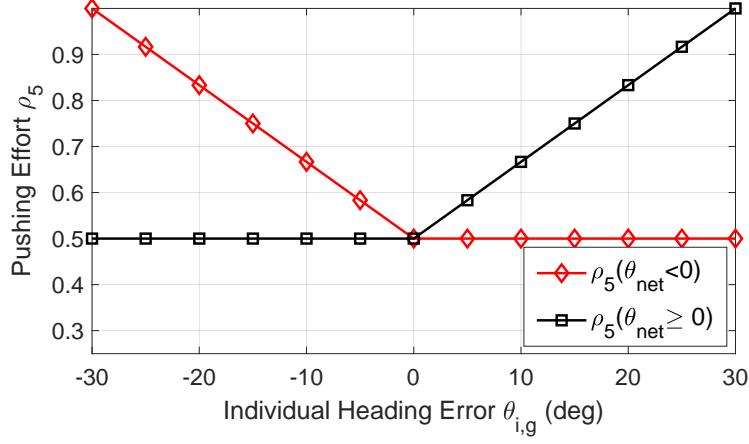
Figure 5.4. Pushing effort ρ_5 model for robots in state $S5$ based on $\theta_{i,g}$ and $\text{sign}(\theta_{net})$ for $\phi = 30^o$, $\alpha = 1$ following Eq. 5.6.

where α is a constant, and $0 < \alpha \leq 1$.

Acknowledging that in reality, individual robots are constrained by their pushing capabilities without any wheel slip and may be unable to drive the collective heading error to zero. This maximum pushing capability of each robot is reflected by the choice of α in Eq. 5.6. Once the pushing effort saturation is exceeded, i.e. $\rho_5 > 2\alpha$ for $|\theta_{i,g}| > \phi$, the robot transitions back to state $S3$ in search of another pushing location. This ensures that the collective heading error of all robots in $S5$ is always bounded within $[-n\phi, n\phi]$, where n is the number of robots in $S5$ at any given time. A visual illustration of the proposed model-based linear pushing effort regulation for $\phi = 30^o$ and $\alpha = 1$ is shown in Fig. 5.4.

Inter-robot Collision Avoidance

Free moving robots in the system must repel one another to maintain a safe distance and prevent collision. Therefore, robots in states $S1$, $S2$, $S3$ and $S6$ actively repel neighboring robots in states $S1$, $S2$, $S3$, $S4$, $S5$ and $S6$ using a repulsive potential within safety distance d_e:

$$u_{repel} = -\frac{\rho_r}{|\overrightarrow{r_i r_j}|^2} \widehat{\overrightarrow{r_i r_j}} \text{ for } |\overrightarrow{r_i r_j}| \leq d_e \tag{5.7}$$

where ρ_r is a repulsion constant, and R_i is in state $S1$, $S2$, $S3$ or $S6$, and R_j is in $S1$, $S2$, $S3$, $S4$, $S5$ or $S6$. R_i in state $S4$ or $S5$ prioritizes object pushing and relies on the repulsion set by other robots in its vicinity to maintain a safe distance from it; it transitions to $S3$ to

avoid collision and relocates if a nearby pushing robot R_j in $S4$ or $S5$ comes too close with an impending collision while pushing with a smaller heading angle error, i.e. $|\overrightarrow{r_i r_j}| \leq d_e$ for R_i, R_j in $S4$ or $S5$ and $|\theta_{i,g}| \geq |\theta_{j,g}|$.

The proposed finite state machine implementation along with the motion control method allows robots to only settle at identified pushing surfaces on the goal occluded region and push the object regulating their effort trying to correct their individual heading angle error within the bounded angle ϕ avoiding any inter-robot collision. Stagnation points where the sum of all pushing efforts equal zero are avoided by pushing robots in $S5$ by robots returning to boundary following in $S3$ to determine a new set of pushing surfaces. The process repeats until the object starts to move again and the stagnation point is overcome. Therefore, the motion of the object is concluded to be always in the direction of the goal by the pushing robots only, assuming that the object is placed on a flat surface with zero gradient. The proposed method may still be applicable for objects placed on a gradient if the static friction between the object and the floor is enough to oppose any resultant motion of the object by itself.

5.4   Validation

We present the validation results of the proposed multi-robot arbitrary object transportation method over three sets of experiments. Experiment sets A and B present object transportation results of simple shapes such as a disk and a rectangular box for analysis purposes. The effectiveness of the proposed model-based pushing effort regulation is presented comparing transportation performance with and without the proposed method; the robustness of pushing effort regulation is also investigated with dynamically changing object weight and center of mass of the object. Experiment Set C presents the effectiveness and robustness of the proposed method in transporting a general arbitrary shaped object having convex and non-convex boundary regions, and non-uniform weight distribution using a larger number of robots. Effects of initial object pose on transportation time and path efficiency results are presented along with scalability analysis. All robots in all experiments were assumed to be capable of pushing the sample objects individually within their abilities. In all cases, robots
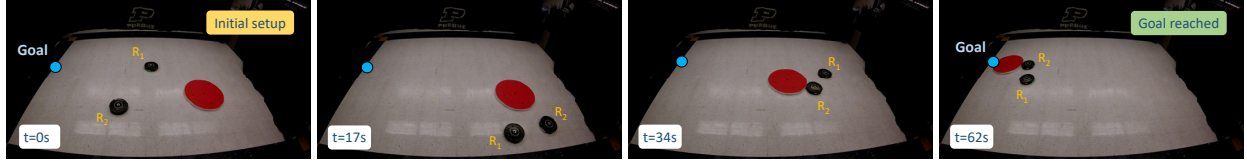
(a) Trial 1 time lapse illustration of the 2 robots transporting a disk-shaped object of uniform weight distribution towards the goal.
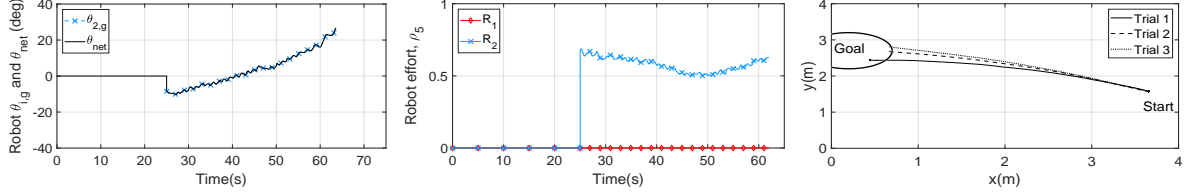
(b) Individual robot and net heading angle error while pushing, confined within $[-\phi, \phi]$ and $[-2\phi, 2\phi]$ respectively.

(c) Pushing effort ρ_5 in response to individual and collective heading angle error to push object towards the goal location.

(d) Object centroid path to goal, showing object path converging towards the goal region successfully for all independent trials.

Figure 5.5. Experiment A.1: Transporting a $0.04\,\mathrm{kg}$ disk with diameter $0.83\,\mathrm{m}$ and uniform weight distribution using 2 robots. With only one potential pushing location, the object was transported by one robot as expected.

were unaware of the object shape, size, weight, center of mass, or the total number of robots involved in the transportation process.

For object transport performance analysis purposes, we define a required object transportation time metric as the time elapsed from the start of a trial until the object centroid reaches the defined goal region. A path efficiency metric is also defined based on the shortest distance from the object centroid location at initial time to the nearest point on the goal region l_{min}, and the actual total distance travelled by the object centroid in the transportation process l, evaluated as $\frac{l_{min}}{l}$.

5.4.1 Experiment A: Disk and Rectangular Box Transportation

In Experiment Set A, experimental results of transporting simple shapes with uniform weight distribution such as a disk and a large rectangular box with two iRobot Create robots are presented over repeated trials. The disk was weighed at $0.04\,\mathrm{kg}$ with a diameter of $0.83\,\mathrm{m}$, and the rectangular box was weighed at $3.5\,\mathrm{kg}$ with dimensions of $1.27 \times 0.78\,\mathrm{m}$. Experiments

(a) Trial 1 time lapse illustration of the 2 robots transporting a rectangular box of uniform weight distribution towards the goal.
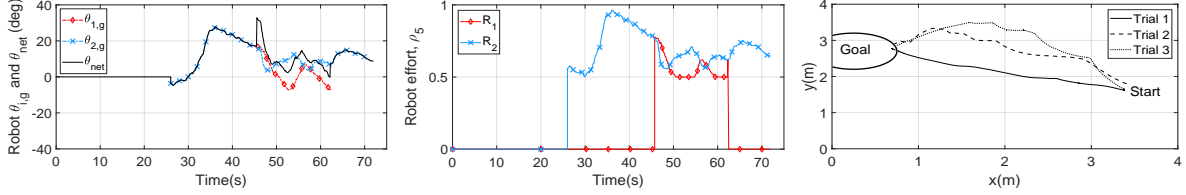
(b) Individual robot and net heading angle error while pushing, confined within $[-\phi, \phi]$ and $[-2\phi, 2\phi]$ respectively.

(c) Pushing effort ρ_5 in response to individual and collective heading angle error to push object towards the goal location.

(d) Object centroid path to goal, showing object path converging towards the goal region successfully for all independent trials.
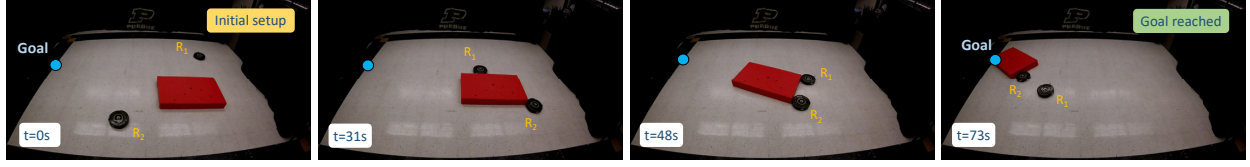
Figure 5.6. Experiment A.2: Transporting a 1.27×0.78 m, 3.5 kg rectangular box with uniform weight distribution using 2 robots. Due to its shape, two pushing locations are available when a side is perpendicular to the goal direction; at other times, the box must be pushed at the corners. The robots are observed to collaboratively transport the object to the goal.

were conducted on a 4×4 m planar surface with two iRobot Create robots assumed to be capable of detecting the object boundary and other robots within a limited FOV. The front bumpers are considered the pushing surfaces of the iRobot Create robots. Robot and object position data recording, and robot and object detection capabilities were simulated using a VICON tracking system. Given the size of these objects, the disk shape (Experiment A.1) potentially has a single pushing point while the rectangular box (Experiment A.2) has two at certain orientations at any given time.

Figures 5.5a and 5.6a show the time lapse illustration of the object transportation process. Time instant $t = 0$ s shows the initial setup of the object's relative position from the goal with the iRobot Create robots randomly placed around it. The goal location is set at a horizontal distance of approximately 3.30 m from the initial object geometric centroid position. In each case, the object transportation method was considered successful if the geometric centroid of the object reached within a 0.5 m radius of the set goal. The motion control parameters are set as $\rho_1 = 1$, $\rho_2 = \rho_3 = \rho_6 = 0.56$, $\rho_4 = 0.6$, $\rho_r = 0.003$ with $v_m = 0.3$ m/s and $\omega_m = 2.2$ rad/s,

the distance parameters are set as $r_d = 2\,\text{m}$, $d_e = 0.3\,\text{m}$ and $d_s = 0.3\,\text{m}$, the pushing effort parameter is set as $\alpha = 1$ and the finite state machine parameters are set as $\delta = 0.2$ and $\phi = 30^o$.

In Experiment A.1, the robots are observed to follow the boundary at $t = 17\,\text{s}$. The disk shape potentially having a single pushing point was transported by a single robot (R_2) over $t = 34\,\text{s}$ and $t = 62\,\text{s}$ having successfully detected the pushing location. With no prior knowledge of the object shape, the other iRobot Create (R_1) continued to follow the boundary looking for a pushing location. Fig. 5.5b and 5.5c plots the measured individual heading angle error of each robot and the net heading error governing η determining the boundary following direction, and the resulting pushing effort. Without R_1 ever pushing the object, θ_{net} was equal to $\theta_{2,g}$, and R_2 is observed to regulate its pushing based on the heading angle error. Since R_1 was never involved in pushing, its pushing effort remained at zero throughout.

Several trials were run of the disk transportation process. The object centroid path from the start to the goal location for the first 3 trials are shown in Fig. 5.5d; the disk was successfully transported in all trials with the lowest path efficiency recorded to be $96\,\%$. The disk-shaped object was transported with a mean time of $65.4\,\text{s}$ with a standard deviation of $6.02\,\text{s}$.

Similar observations were made for the rectangular box transportation in Experiment A.2. The measured individual heading angle error of each robot and the net heading error along with the resulting pushing effort are plotted in Fig. 5.6b and 5.6c. R_2 initially identified the corner of the box as a potential pushing location at $t = 26\,\text{s}$. It continued to push regulating its pushing effort based on θ_{net} equal to $\theta_{2,g}$ until the resultant change in orientation of the box allowed a second pushing location of the object to become available to R_1 at $t = 47\,\text{s}$. The two robots were then observed to successfully transport the rectangular box collaboratively to the set goal location. R_2 was continuously observed to exert a larger pushing effort to generate a net clockwise rotation of the object around its unknown center of mass as θ_{net} remained positive throughout as a result of the goal location placed on the opposite end of the center of mass of the box. R_1 was observed to correct any overshoots in the clockwise rotation of the object by balancing it with an increasing counterclockwise motion when its

own heading angle error became the same sign as θ_{net}. As a result, a fairly straight efficient path of the object was observed to the goal location in Trial 1 as shown in Fig. 5.6d.

The rectangular box transportation process was repeated over several independent trials. Although the object was successfully transported to the goal location in all trials, some of the observed paths resulted in a large standard deviation of required transport time, due to the shape of the rectangular box. For a majority of the time, the robots could push the object from corner locations only; for more than one pushing location to be used, one of the boundary surfaces of the object needed to be perpendicular to the goal vector from a robot currently following this side of the object boundary; which only happened in rare instances with the **2** robot setup. The process could therefore be improved with redundant robots available. Regardless, the lowest path efficiency was observed to be as low as **71.2%** with reference to the shortest distance. Paths recorded from trials **2** and **3** are shown in Fig. 5.6d. The rectangular box shaped object was transported with a mean time of **69.7** s with a standard deviation of **46** s. We also note here that an increased path efficiency could be obtained with a transportation time trade-off by setting a smaller ϕ; with a smaller bound on allowed heading angle error robots will tend to relocate more often increasing the transportation time, but the object centroid will remain closer to the shortest path to the goal during the transportation process.

5.4.2 Experiment B: Robustness study of Model-based Pushing Effort Regulation

Experiment Set B is a special case of Experiment A.2 that investigates the effectiveness of the proposed pushing effort regulation, where the rectangular box is required to be transported along a straight line along with robustness studies of dynamically changing weight and center of mass of the rectangular box using two iRobot Create robots. Following the same experiment setup as Experiment A, the object is positioned such that the longest edge is perpendicular to the object centroid to goal vector; the two robots are initially positioned such that both identify a pushing point on the goal occluded side on opposite sides of the object rotational pivot point around the same time. Experiment B.1 presents the straight line motion showing the two robot regulating their balanced pushing efforts to keep the object on a straight line path towards the goal robust to any robot wheel slip effects from the
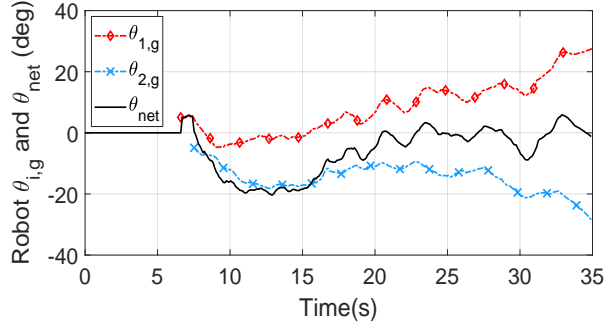
(a) Individual robot and net heading angle error while pushing, confined within $[-\phi, \phi]$ and $[-2\phi, 2\phi]$ respectively.
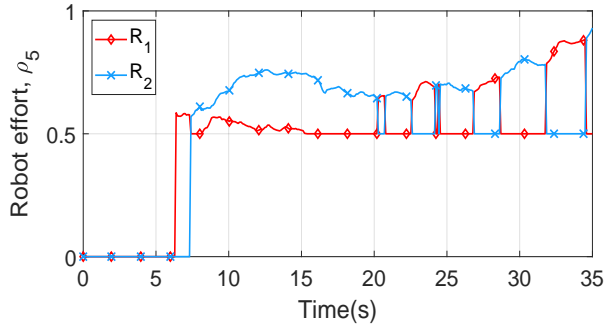
(b) Pushing effort ρ_5 in response to individual and collective heading angle error to push object towards the goal location.
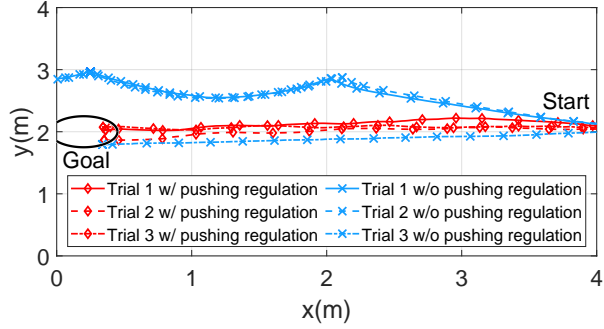
(c) Object centroid path to goal, showing object path to the goal region for all trials with and without pushing effort regulation.

Figure 5.7. Experiment B.1: Two robots carefully placed to find two pushing locations simultaneously; the rectangular box is initially positioned such that the object center to goal vector is perpendicular to its longest edge.
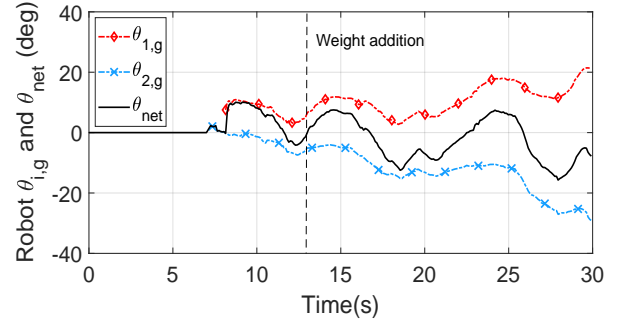
(a) Individual robot and net heading angle error while pushing, confined within $[-\phi, \phi]$ and $[-2\phi, 2\phi]$ respectively.
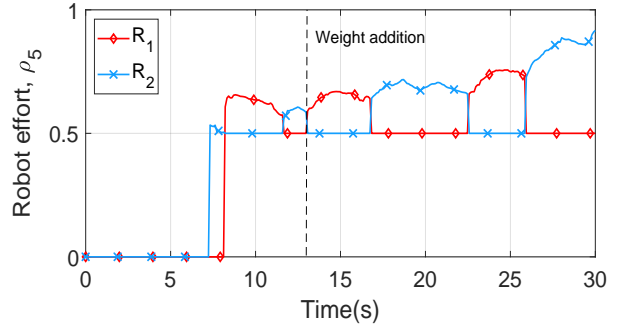
(b) Pushing effort ρ_5 in response to individual and collective heading angle error to push object towards the goal location.
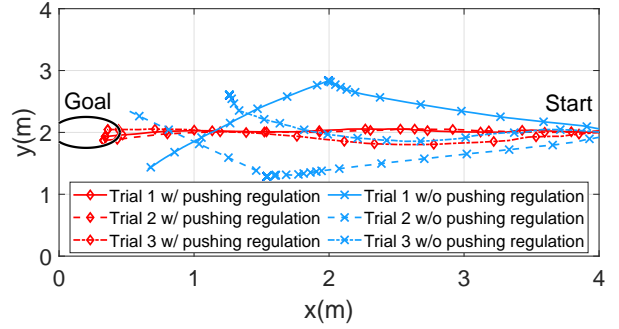
(c) Object centroid path to goal, showing object path to the goal region for all trials with and without pushing effort regulation.

Figure 5.8. Experiment B.2: An additional weight of $2.2\,\mathrm{kg}$ added on one end of the object during the straight line transportation process as in Experiment B.1, to mimic dynamically changing weight and weight distribution of object.

robot and irregular frictional effects between the object and the floor, and the object and the robot pushing surface. Experiment B.2 presents the results of the pushing effort regulation robustness study with a $2.2\,\mathrm{kg}$ weight added to one end of the rectangular box during the transportation process.

Pushing points were identified by both the robots within the first $10\,\mathrm{s}$ in both experimental cases. The measured individual heading angle error of each robot and the net heading error along with their resulting pushing efforts by each robot for Experiment B.1 are plotted in Fig. 5.7a and 5.7b. The heading angle error $\theta_{1,g}$ remains positive and $\theta_{2,g}$ remains negative after initial pushing location identification as the robots positioned themselves on opposite sides of the rotational pivot point of the object. As a result, the collective heading error θ_{net} remained bounded within $[\theta_{2,g}, \theta_{1,g}]$ for the remainder of the transportation process. The two robots are observed to continuously regulate their pushing effort one at a time to drive θ_{net} towards zero countering the effects of any object drift due to wheel slip or irregular friction. ρ_5 always remained within the maximum pushing capability of the robots with $\theta_{i,g}$ for $i \in \{1,2\}$ remaining within $\pm\phi$; therefore, no robot relocation was required during the transportation process. The path traced by the geometric centroid of the object during transportation in Experiment B.1 shows a fairly straight line with minor deviations over 3 presented trials as shown in Fig 5.7c. The cross-track error of the object centroid path with the shortest distance path from the initial position to the goal remained within $0.12\,\mathrm{m}$ at all times with the lowest path efficiency recorded to be at $93.5\,\%$.

For comparison purposes, Experiment B.1 was repeated without the proposed model-based pushing effort regulation; both robots detected the pushing locations and were allowed to push with a constant pushing effort of 0.5 within a heading angle error of $[-\phi, \phi]$. Three resulting object paths from three independent trials are also presented in Fig. 5.7c. A relatively straight path was obtained from Trial 2 with a maximum cross tract error of $0.22\,\mathrm{m}$, while Trials 1 and 3 produced significantly inefficient object transportation paths to the goal. Due to initial minor contact time differences for pushing, and object and floor surface irregular frictional effects, the object drifted off the goal heading direction; without any correction in object rotation by pushing effort regulation, the robots continued to push within the defined heading angle error of $[-\phi, \phi]$. Robot relocation took place at two

instances where heading angle error exceeded $[-\phi, \phi]$; however, the object continued to drift far from the set goal. Based on the observations, it was concluded that the object will eventually converge within the defined goal region following a spiraling path around the goal region requiring several robot relocations, creating a far inefficient path compared to the proposed model-based pushing effort regulation case. Due to space limitations in the experiment setup and the given size of the object, most of the trials including 1 and 3 were stopped without reaching the goal when the object centroid x-position turned negative.

Similar observations were made in Experiment B.2 where an additional weight of $2.2\,\text{kg}$ was added on the right end of the rectangular box during the transportation process at $t = 13\,\text{s}$. The measured individual heading angle error of each robot and the net heading error along with the resulting pushing effort are plotted in Fig. 5.8a and 5.8b. With the dynamic weight addition, the lighter end of the object started to rotate clockwise as expected between time $14 \leq t \leq 17\,\text{s}$ with θ_{net} turning negative for a longer duration between time $16 \leq t \leq 23\,\text{s}$. As $\theta_{2,g}$ decreased as a result of this rotation, the pushing effort for R_2 increased its pushing effort to $\rho_5 = 0.7$ with $\theta_{2,g} < 0$ to counter the drift effect of the non-uniform weight distribution of the object, while R_1 remained at the minimum of $\rho_5 = 0.5$ with $\theta_{1,g} > 0$. The additional effort by R_2 rotated the object back in the clockwise direction to correct the object's heading towards the goal. As a result, θ_{net} returned to being close to zero. As the object got closer to the goal, the individual heading angle errors increased due to their relative location; as a result, both robots regulated the object heading with an increasingly higher pushing effort over time. However, R_2 was observed to apply larger pushing efforts than R_1 over longer time durations due to the center of mass offset placing it closer to its pushing end on the object. The path traced by the geometric centroid of the object during transportation with the dynamically added weight shows a fairly straight line with minor deviations over 3 presented trials as shown in Fig 5.8c with a maximum cross-track error of $0.3\,\text{m}$ and the lowest recorded path efficiency of $87.7\,\%$.

The proposed system is therefore concluded to be robust to dynamically changing weight and center of mass. For comparison purposes, the experiment was repeated without the proposed pushing effort regulation and the observed path of 3 independent trials are shown in Fig 5.8c. In both Trials 1 and 3, the object started drifting to the right with a net

clockwise rotation due to the center of mass offset as expected before requiring robots to relocate and continue pushing. Trial 2 produced a path where the object drifted to the left; this was due to an unexpected case where both robots determined their pushing locations and settling on the same end of the object relative to the object center line to the goal location. Regardless, in all 3 trials the paths obtained without the proposed pushing effort regulation were significantly less efficient and the transportation process was stopped being deemed irrelevant, when the object was within $1\,\text{m}$ of the goal region with an inaccurate heading and requiring robot relocation.

5.4.3   Experiment C: Robustness to Object Shape, Weight Distribution and Initial Pose

A $20 \times 15\,\text{m}$ planar confined area with Pioneer P3-DX robots was considered on the physics-based 3D robotic simulator V-Rep [150] for the setup of Experiment Set C. The stretched bumpers of the P3-DX robots on the front were considered the pushing surfaces and the array of ultrasonic sensors available were used for distance measurements. A representative sample object of arbitrary shape having convex and non-convex boundary regions weighing $10\,\text{kg}$ and having its center of mass at an offset from its geometric centroid on the *xy* plane was created for the experiment. The goal location was set at a horizontal distance of $13.42\,\text{m}$ from the object geometric centroid closer to the lighter end of the object, such that with a uniform pushing profile on the goal occluded region of the object, the object was expected to have a net counter-clockwise rotation drifting it away from the set goal. Five Pioneer P3-dx robots were considered to transport the sample object of non-uniform weight distribution at initial orientation $\theta_o = 30^o$, to the set goal region. Fig. 5.9a shows the time lapse illustration of the object transportation process.

The object path was observed to drift towards the heavier end of the object and following the proposed object transport method more robots relocated to the heavier end as a consequence, to push the object back towards the goal. Robots continued to accumulate behind the heavy end of the object to push it towards the goal. The goal region was reached in around 4.5 minutes. The path traced by the geometric centroid of the object during transportation shows a fairly straight line with minor deviations closer to the goal and the object orientation goes to zero over time with the lighter end of the object eventually pushed to the
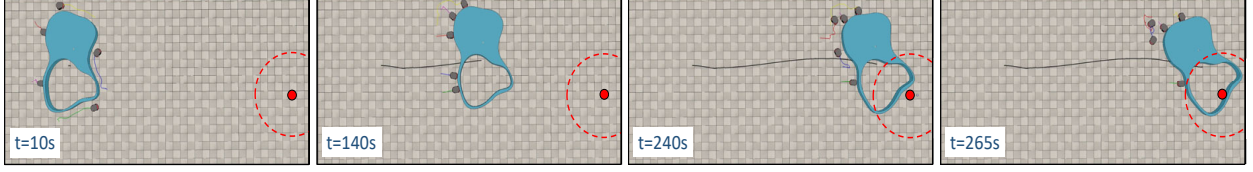
(a) Time lapse illustration of Trial 1 of the **5** Pioneer robot arbitrary shaped object transportation process towards the goal (red).
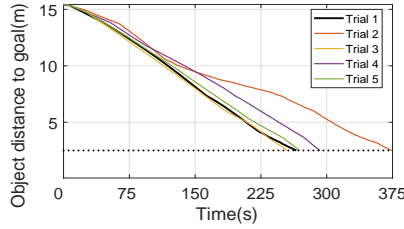
(b) Object centroid distance to goal with time showing object moves to goal location in finite time for all trials.
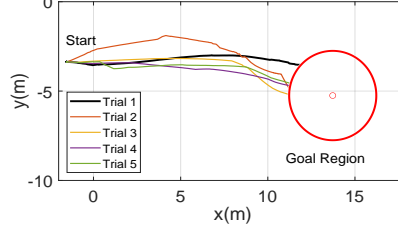
(c) Object centroid path to goal showing object path converging towards the goal region successfully for all trials.
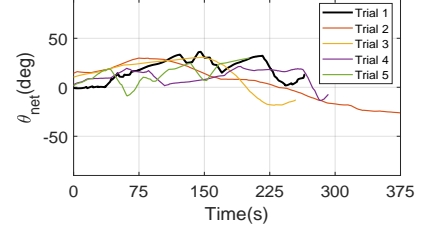
(d) Collective heading error for all trials remained within their specific bounds throughout the transport process.

Figure 5.9. Experiment C: Object with arbitrary shape having convex and non-convex boundary regions, and non-uniform weight distribution at $\theta_o = 30^o$ transported to the goal location by **5** Pioneer robots regulating their pushing effort and relocating if necessary in response to object behavior.

front as shown in the final time step of Fig. 5.9a. Several independent trials of the arbitrary object transportation process were conducted and the resulting object centroid distance to goal, path to goal and the net heading angle error θ_{net} of the first **5** trials are shown in Fig. 5.9b, 5.9c and 5.9d respectively. Similar observations were recorded in all trials. The mean and median of the transport times obtained were **291** s and **268** s.

Experiment sets A and B concluded that the number of pushing surfaces available on the object boundary at any given time, their utilization depending on initial robot deployment, and even minor differences in the initial object orientation can have a significant impact on the object transportation performance. Therefore, Experiment C was repeated for initial object orientation $\theta_o = 0^o$ to 330° at increments of 30° with **5** independent trials run at each orientation for random initial distributions of robots. Since object detection by random walk is not the focus of our study, for every trial all robots positioned randomly around the object were ensured to have the object at least partially visible within their FOV. The performance of the proposed object transport method was analyzed in terms of the required transportation

127
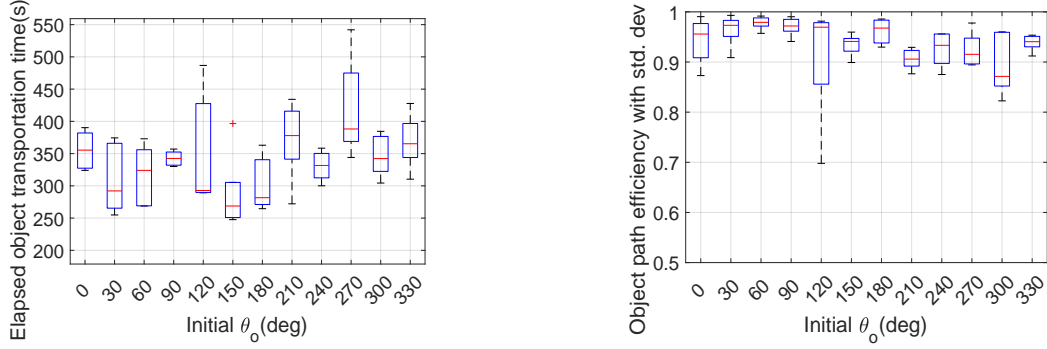
(a) The median and variability of object transportation elapsed time for 5 trial sets for each $\theta_o = 0^o$ to 330°.

(b) The median and variability of path efficiency for 5 trial sets for each $\theta_o = 0^o$ to 330°.

Figure 5.10. The object of non-uniform weight was successfully transported to the defined goal location with 5 randomly placed robots around the object, for all trials of initial object orientation 0° to 330° with increments of 30°.

time and the efficiency of the path taken by the multi-robot object transportation for each initial orientation and trial.

For all $\theta_o = 0^o$ to 330°, the object was successfully transported to the goal location within finite time. The median elapsed time for all initial orientations were recorded between 250 and 400 s with the minimum and maximum of 247 and 543 s at $\theta_o = 150^o$ and $\theta_o = 270^o$ respectively. The variability in the recorded data remained more or less consistent as expected, except for $\theta_o = 120^o$ and 270°. By design of the object and the experiment setup, at these object orientations, robots were either pushing only the heavier end or the lighter end of the object at a time. Due to the less number of pushing points available at these orientations and the imbalanced nature of the load along this pushing line because of the non-uniform weight distribution, a larger variability in the object transportation time was observed. A box and whisker plot of elapsed time for all 5 trial sets for each $\theta_o = 0^o$ to 330° is shown in Fig. 5.10a.

A path efficiency box and whisker plot for all 5 trial sets for each $\theta_o = 0^o$ to 330° is shown in Fig. 5.10b. The path efficiency for most trial sets for $\theta_o = 0^o$ to 330° showed small variability and the median for all were recorded higher than 90 % except for one instance of 87 % at $\theta_o = 300^o$. The minimum path efficiency was recorded 69 % at one instance for $\theta_o = 120^o$ and the maximum was recorded to be 99 %. The object was therefore pushed in a more or less straight path for the majority of the trials. For the rest, that showed minor
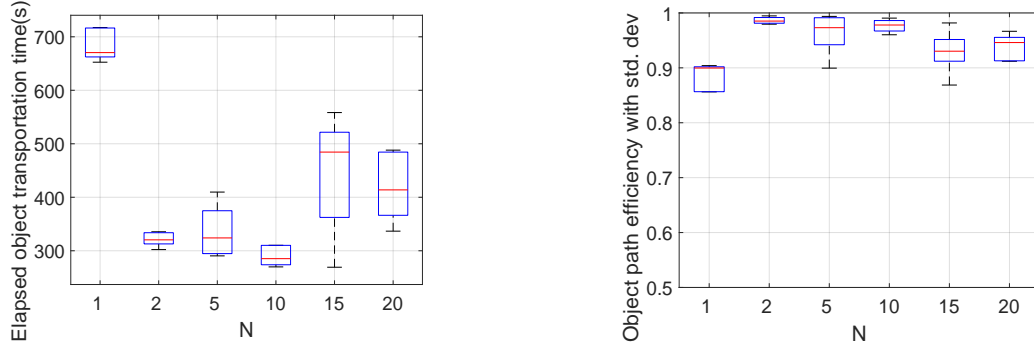
(a) The median and variability of object transportation elapsed time for 10 trial sets for each N.

(b) The median and variability of path efficiency for 10 trial sets for each N.

Figure 5.11. Scalability: The object of non-uniform weight with $\theta_o = 30^o$ was successfully transported to the defined goal location with $N = 1$, 2, 5, 10, 15 and 20 randomly placed robots around the object over 10 trials each.

deviations from the shortest distance path, the actual path was eventually corrected to reach the goal. The object was transported to the goal location successfully for all trials.

5.4.4 Scalability Analysis

A larger robot group may provide a potentially larger net pushing effort to push an object towards the goal. However, pushing is limited to the number of available pushing surfaces on the object boundary that depends on the size, shape, and orientation of the object at any given time of the transportation process. Pushing is also limited by the inter-robot safety distance that affects how many robots are able to push at a time safely without any collision with one another. Experiment C of transporting the arbitrary shaped object initially at $\theta_o = 30^o$ was repeated with an increasing number of $N = 1$, 2, 5, 10, 15, and 20 Pioneer P3-DX robots each with 10 independent trials with random robot placement around the object. The median and variability of the object transportation elapsed time and path efficiency obtained are shown in Fig. 5.11a and 5.11b respectively. The $N = 1$ robot case yielded the longest transportation time as expected. The object was transported increasingly quickly with $N = 2$, 5 and 10 robots; however, given the size of the object relative to the robots, the elapsed time is observed to increase for larger N values beyond that. This was due to robots constantly relocating to avoid collision with other nearby pushing robots by maintaining

their set safety distance as their pushing surface slide along the object boundary during its motion. The analysis was confirmed with the scalability experiment repeated for the same arbitrary object 3 times the current size where the lowest elapsed time was obtained for $N = 20$. The median path efficiency for all scalability experiment cases remained over 90% with the lowest observed for $N = 1$ as expected, and the highest observed for $N = 2$ closely followed by $N = 10$ and $N = 5$ for similar reasons as the analyzed object transportation time.

5.4.5 Discussion

The proposed multi-robot object transport process includes: 1) robots relying on individual assessment for identification of potential pushing points based on their perceived boundary of the object of interest within its FOV, 2) zero coefficient of restitution collision with object during initial contact for pushing, 3) model-based pushing effort regulation within capabilities based on changing individual heading while pushing, and 4) potential field-based motion coordination with passive and active collision avoidance based on robot state. Experiment sets A, B and C demonstrated the effectiveness of the proposed multi-robot arbitrary object transportation method including robustness to dynamically changing weight distributions and external disturbances such as non-uniform friction between contacting surfaces and robot wheel slip. Scalability analysis revealed that the proposed system performance in terms of transportation time is dependent on the number of pushing surfaces available which in turn depends on the object size, shape and set inter-robot safety distance. The proposed system yielded fairly efficient paths of the object transportation process with consistent elapsed time requirement over several trials. All robots successfully avoided inter-robot and robot-object collisions in all experiment and simulation trials.

The applicability of our method can be extended to path following of an object to move around obstacles. Experimental results verified successful path following implementation of the designed object by 5 robots as shown in Fig. 5.12.

Given the complexity of different shapes including discontinuous boundary surfaces, system parameter δ must be adjusted based on the application scenario for ensuring that a pushing surface is always found for any arbitrary shape. Pushing surface locations on the disk-shaped object was successfully determined every time by robots for $\delta = 0.1$. However,
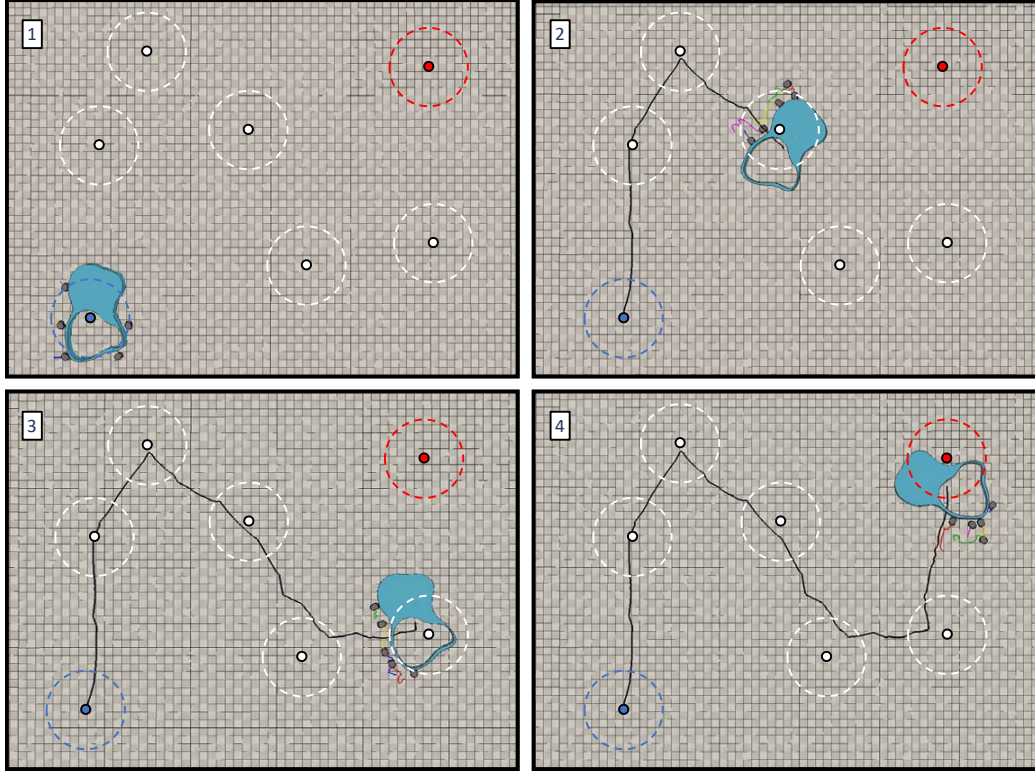
Figure 5.12. Object transportation to goal locations extended to path following with acceptable cross-track error. Blue, red and white markers denote starting, end and intermediate path positions.

at certain orientation of the rectangular box when a corner is the only pushing location available, δ was increased to 0.2 to obtain the same success rate. Allowing the robots to boundary follow at slower speeds also improved the success rate of determining pushing surface identification.

In spite of the robustness of our approach to arbitrary object shapes and weight distributions, our method does not consider wheel slip effects on the pushing effort regulation. We admit that it limits the applicability of our method to robots with traction control; design parameter α must be tuned based on the robot's pushing capability of objects. The system is therefore currently limited to objects being light enough for each robot to push. We leave incorporating anti-wheel slip considerations in pushing effort regulation as future work of our proposed method.

The proposed transportation method is robust to robot failures assuming at least one robot remains functional and a disabled robot does not block the path of the object. Push-

ing location identification and effort regulation are dynamic processes; failed robots during pushing are replaced by other robots since the pushing frontier is continuously changing with the object's motion.

5.5   Conclusion

In this chapter, a multi-robot object transportation strategy is presented for objects of arbitrary shape and geometry, mass and mass distribution based on observable coordination strategies employed by human beings in object transport processes. A finite state machine design with specific motion control formulation for distributed pushing point identification, collision avoidance, and dynamic model-based pushing effort regulation has been proposed. Experimental results validated the effectiveness and robustness of the proposed methods in presence of dynamically changing object weight and weight distribution of the object and external disturbances such as non-uniform friction between contacting surfaces and robot wheel slip to drive the object towards the goal. Detailed analysis on object transportation performance based on initial object pose and availability of pushing points has been presented in terms of required transportation time and path efficiency for a number of trials. Scalability analysis of the proposed method suggests that elapsed transport time and path efficiency of objects are significantly improved for two or more robots cooperating in the transport process over single robots.

6. CONCLUSION

Numerous living organisms found in nature have learnt to be self-sustainable as a group through the proven method of evolution; schools of fish have developed fruitful methods of predator detection and evasion as a group and flocks of birds flying in shapes have developed methods of relying on one another to maintain flight over long distances without tiring. In both these examples, individuals are observed to take turns being in positions that are detrimental to them; individuals on the outside of the school are most exposed to predators and birds on the front of the V-shape formation require more effort to fly. But the continuous process benefits the group as a whole. Numerous other examples are available in nature that have allowed individuals capable of feats as part of a cooperating group otherwise impossible. Human beings have also learnt to live as a society relying on one another for protection and livelihoods. Certain social conducts such as cooperation, and altruistic behavioral traits have emerged with time that have allowed individuals to support one another that benefits the group as a whole. Although the field of multi-robot systems have come a long way since its initiation, we believe the true potential of connected robotic systems is yet to be realized. The research presented in this dissertation is a step towards such group based improved capabilities in multi-robot systems that can only be achieved by relying on one another. To that end, a number of group dependent multi-robot self-organization and application specific strategies have been proposed in this research work.

Group survival strategies proposed in this dissertation include self-organization methods for internal resource sharing and/or distribution in structured and unstructured robot groups, and surviving damaging external stimuli as a group by taking turns on the leeward side. The cyclic energy sharing method in structured convoying robot groups allowed groups of increasing numbers of robots and various sizes to consistently travel much larger distances over the control case of no relocation, while maintaining a small variance in battery levels between all robots. In all simulation cases, robot groups were able to travel over 4 times the distance with the proposed method as tested. The AIS controller proposed for the unstructured energy sharing and distribution process yielded 55%, 42%, 23% and 33% performance improvements in equilibrium attainment convergence time for skewed, bi-modal, normal

and random initial agent resource level distributions respectively on a 2D plane using the proposed energy distribution method over the control method of no adaptive spacing. Scalability analysis for both energy sharing concepts confirmed their application with consistently improved performances different sized groups of robots.

In addition to internal energy sharing classified as self-organization based in internal stimuli, the proposed group survival methods in this dissertation also presented a distributed strategy of surviving damaging directional external stimuli as a group. Partially inspired by the Huddling behavior of Emperor Penguins in the Antarctic, simulation results verified that groups of robots were able to survive longer in the field exposed to extreme conditions using the proposed relocation strategies in the group. The distributed global health loss rate minima estimation allowed the development of two settling conditions. The global health loss rate minima settling method yielded 12.6%, 5.3%, 16.7% and 14.2% improvement in average robot health over the control case of no relocation, while the optimized health loss rate minima settling method further improved on the global health loss rate settling method by 3.9%, 1.9%, 1.7% and 0.6% for robot group sizes 26, 35, 70 and 107 respectively.

Group survival is a fundamental requirement of functioning groups of robots that becomes significantly relevant in long term applications where field deployed multi-robot systems do not have access to human assistance or supervision. The proposed self-organizing methodologies for group survival present enormous opportunities for application in a number of research areas. The resource distribution method could be utilized for energy management for a large robot swarm on large area exploration where recharging methods are sporadically available in certain areas. Specific examples include cloud cover or low light hampering solar based recharging of robot units in the field, where robots from other areas may dynamically self-organize from time to time to distribute total accumulated energy to the group. The proposed method is generalized to be applicable for any on-board resource that could be shared within a close proximity without overcrowding one another, e.g. exchange of information for continuous map building, surveillance etc. The damaging external stimuli survival method using GPML could be directly applied to multi-robot groups in the field exposed to a directional external stimuli. This cyclic self-organization method could also be applied in self-healing material research where nano or micro-size building units cycle

134

to the damaging side of the material layer while taking turns on the leeward side to heal. Self-healing materials with such advanced capabilities could one day be applied on space crafts as protection during re-entry into the atmosphere or even on deep sea diving robots reaching extreme low temperatures and pressures to cycle outer damaged material layers continuously for protection.

As part of the research on application specific cooperation based self-organization case studies, a distributed shape formation strategy with cooperative robots relying on one another is also proposed in this research work. The distributed shape formation method relies on robots that have already settled as part of a forming structure to guide others towards the structure forming frontier. This form of cooperation in providing guidance implemented as a propagating gradient from beacon robots, allows searching robots to follow efficient paths along the structure surface to reach the next required structure forming location and settle. Simulation results validated the successful formation of 2D and 3D shapes using the finite state machine-based shape formation process. The proposed methodology could be applied in a number of application areas ranging from programmable matter [151] to the construction and manufacturing industry. The proposed method does not require any external control or human supervision; robots cooperate with one another to guide neighbors to required positions. The system is also concluded to be robust to robot failures during the shape formation process.

The second case study on application specific cooperation based self-organization in multi-robot systems include an arbitrary object transportation strategy for objects of irregular shape, size and weight distribution. The system is robust enough to ensure that a given object can be transported by a single robot assuming the robot is capable of pushing it on its own. However, experimental results with two iRobot Create robots validate that an efficient object path can only be achieved with two or more cooperating robots pushing at the same time. Individual robots start to push the object regulating their effort, with hope that another robot finds a pushing location on the other end of the center of mass to balance the moment and ensure no unintended object rotation occurs during its transportation. Applications of this research work include direct implementation in the construction industry transporting heavy building blocks, warehouse logistics, path clearance for evac-

135

uation in disaster scenarios etc. Efficient paths of object transportation are a necessity in all such applications often with multi-robot systems unaware of object shape, size or weight distribution. The current method is confined to planar operations of object transport. As future work, the proposed method could be adapted for usability in 3D space in presence of external disturbances resulting in object motion for applications including targeted drug delivery [152] and deep sea rescue operations [153].

The research presented in this dissertation effectively demonstrates how certain multi-robot system characteristics such as chances of survival or application performance can be greatly improved by altruistic and cooperative behaviors by individual robotic systems. Given the variety of ways inter-robot support can be implemented, each chapter is concluded with its own analysis and discussion on current shortcomings and future work on the topic.

The research presented in this dissertation directly impacts how robots may one day interact with one another. More importantly, it changes human perception of robots from machines to social entities capable of exhibiting prosocial behaviors in a society for the greater good of the group. With promising results, the work presented here opens new doors on multi-robot self-sustainability research in the future.

REFERENCES

[1] H. Asama, A. Matsumoto, and Y. Ishida, "Design of an autonomous and distributed robot system: Actress," in Proceedings. IEEE/RSJ International Workshop on Intelligent Robots and Systems'.(IROS'89)'The Autonomous Mobile Robots and Its Applications, IEEE, 1989, pp. 283–290.

[2] P. Caloud, W. Choi, J.-C. Latombe, C. Le Pape, and M. Yim, "Indoor automation with many mobile robots," in EEE International Workshop on Intelligent Robots and Systems, Towards a New Frontier of Applications, IEEE, 1990, pp. 67–72.

[3] T. Fukuda, T. Ueyama, Y. Kawauchi, and F. Arai, "Concept of cellular robotic system (cebot) and basic strategies for its realization," Computers & electrical engineering, vol. 18, no. 1, pp. 11–39, 1992.

[4] L. E. Parker, "Alliance: An architecture for fault tolerant, cooperative control of heterogeneous mobile robots," in Proceedings of IEEE/RSJ International Conference on Intelligent Robots and Systems (IROS'94), IEEE, vol. 2, 1994, pp. 776–783.

[5] S. C. Botelho and R. Alami, "M+: A scheme for multi-robot cooperation through negotiated task allocation and achievement," in Proceedings 1999 IEEE International Conference on Robotics and Automation (Cat. No. 99CH36288C), IEEE, vol. 2, 1999, pp. 1234–1239.

[6] B. P. Gerkey and M. J. Mataric, "Murdoch: Publish/subscribe task allocation for heterogeneous agents," AAAI/IAAI, vol. 1070, 2000.

[7] F. Tang and L. E. Parker, "Asymtre: Automated synthesis of multi-robot task solutions through software reconfiguration," in Proceedings of the 2005 IEEE international conference on robotics and automation, IEEE, 2005, pp. 1501–1508.

[8] J. Wawerla and R. T. Vaughan, "A fast and frugal method for team-task allocation in a multi-robot transportation system," in Robotics and Automation (ICRA), 2010 IEEE International Conference on, IEEE, 2010, pp. 1432–1437.

[9] W. Burgard, M. Moors, D. Fox, R. Simmons, and S. Thrun, "Collaborative multi-robot exploration," in Robotics and Automation, 2000. Proceedings. ICRA'00. IEEE International Conference on, IEEE, vol. 1, 2000, pp. 476–481.

[10] S. I. Roumeliotis and G. A. Bekey, "Distributed multirobot localization," IEEE Transactions on Robotics and Automation, vol. 18, no. 5, pp. 781–795, 2002.

[11] A. Prorok, A. Bahr, and A. Martinoli, "Low-cost collaborative localization for large-scale multi-robot systems," in Robotics and Automation (ICRA), 2012 IEEE International Conference on, Ieee, 2012, pp. 4236–4241.

[12] D. Portugal and R. Rocha, "Msp algorithm: Multi-robot patrolling based on territory allocation using balanced graph partitioning," in Proceedings of the 2010 ACM symposium on applied computing, ACM, 2010, pp. 1271–1276.

[13] W. Sheng, Q. Yang, J. Tan, and N. Xi, "Distributed multi-robot coordination in area exploration," Robotics and Autonomous Systems, vol. 54, no. 12, pp. 945–955, 2006.

[14] C. Luo, A. P. Espinosa, D. Pranantha, and A. De Gloria, "Multi-robot search and rescue team," in Safety, Security, and Rescue Robotics (SSRR), 2011 IEEE International Symposium on, IEEE, 2011, pp. 296–301.

[15] L. Ray, A. Price, A. Streeter, D. Denton, and J. H. Lever, "The design of a mobile robot for instrument network deployment in antarctica," in Robotics and Automation, 2005. ICRA 2005. Proceedings of the 2005 IEEE International Conference on, IEEE, 2005, pp. 2111–2116. doi: 10.1109/ROBOT.2005.1570425.

[16] L. Pedersen, D. Wettergreen, D. Apostolopoulos, C. McKay, M. DiGoia, D. Jonak, S. Heys, J. Teza, and M. Wagner, "Rover design for polar astrobiological exploration," Robotics Institute, p. 25, 2005.

[17] S. Russell and P. Norvig, "Artificial intelligence: A modern approach," 2002.

[18] Z. Yan, N. Jouandeau, and A. A. Cherif, "A survey and analysis of multi-robot coordination," International Journal of Advanced Robotic Systems, vol. 10, no. 12, p. 399, 2013.

[19] M. Olaifa, T. Mapayi, and R. Van Der Merwe, "Multi ant la: An adaptive multi agent resource discovery for peer to peer grid systems," in Science and Information Conference (SAI), 2015, IEEE, 2015, pp. 447–451. doi: 10.1109/SAI.2015.7237180.

[20] C. W. Reynolds, "Flocks, herds and schools: A distributed behavioral model," ACM SIGGRAPH computer graphics, vol. 21, no. 4, pp. 25–34, 1987.

[21] R. Salhab, R. P. Malhamé, and J. Le Ny, "A dynamic game model of collective choice in multi-agent systems," IEEE Transactions on Automatic Control, 2017. doi: 10.1109/TAC.2017.2723956.

[22] C. Breazeal, K. Dautenhahn, and T. Kanda, "Social robotics," in Springer handbook of robotics, Springer, 2016, pp. 1935–1972.

[23] C. D. Batson, "Addressing the altruism question experimentally," Altruism and altruistic love: Science, philosophy, and religion in dialogue, pp. 89–105, 2002.

[24] K. S. Cook and R. M. Cooper, "Experimental studies of cooperation, trust, and social exchange.," 2003.

[25] L. E. Parker, "Decision making as optimization in multi-robot teams," in International Conference on Distributed Computing and Internet Technology, Springer, 2012, pp. 35–49.

[26] J. Alonso-Mora, A. Breitenmoser, M. Rufli, R. Siegwart, and P. Beardsley, "Multi-robot system for artistic pattern formation," in 2011 IEEE International Conference on Robotics and Automation, IEEE, 2011, pp. 4512–4517.

[27] X. Jia and M. Q.-H. Meng, "A survey and analysis of task allocation algorithms in multi-robot systems," in 2013 IEEE International Conference on Robotics and biomimetics (ROBIO), IEEE, 2013, pp. 2280–2285.

[28] D. Fox, W. Burgard, H. Kruppa, and S. Thrun, "A probabilistic approach to collaborative multi-robot localization," Autonomous robots, vol. 8, no. 3, pp. 325–344, 2000.

[29] I. Rekleitis, G. Dudek, and E. Milios, "Multi-robot collaboration for robust exploration," Annals of Mathematics and Artificial Intelligence, vol. 31, no. 1-4, pp. 7–40, 2001.

[30] J. S. Jennings, G. Whelan, and W. F. Evans, "Cooperative search and rescue with a team of mobile robots," in 1997 8th International Conference on Advanced Robotics. Proceedings. ICAR'97, IEEE, 1997, pp. 193–200.

[31] T. D. Williams, The penguins: Spheniscidae. Oxford University Press, USA, 1995, vol. 2.

[32] R. Kirkwood and G. Robertson, "The occurrence and purpose of huddling by emperor penguins during foraging trips," Emu, vol. 99, no. 1, pp. 40–45, 2001. doi: https://doi.org/10.1071/MU99006.

[33] J. Prévost, Écologie du manchot empereur Aptenodytes forsteri Gray. Hermann, 1961, vol. 1291.

[34] D. P. Zitterbart, B. Wienecke, J. P. Butler, and B. Fabry, "Coordinated movements prevent jamming in an emperor penguin huddle," PLoS one, vol. 6, no. 6, e20260, 2011. doi: 10.1371/journal.pone.0020260.

[35]   Y. Le Maho, "The emperor penguin: A strategy to live and breed in the cold: Morphology, physiology, ecology, and behavior distinguish the polar emperor penguin from other penguin species, particularly from its close relative, the king penguin," American Scientist, vol. 65, no. 6, pp. 680–693, 1977.

[36]   G. Stead, "Huddling behaviour of emperor penguins," Master's thesis, University of Sheffield, United Kingdom, 2003.

[37]   A. Waters, F. Blanchette, and A. D. Kim, "Modeling huddling penguins," PLoS One, vol. 7, no. 11, e50277, 2012. doi: 10.1371/journal.pone.0050277.

[38]   M. Canals and F. Bozinovic, "Huddling behavior as critical phase transition triggered by low temperatures," Complexity, vol. 17, no. 1, pp. 35–43, 2011. doi: 10.1002/cplx.20370.

[39]   C. Gilbert, S. Blanc, Y. Le Maho, and A. Ancel, "Energy saving processes in huddling emperor penguins: From experiments to theory," Journal of Experimental Biology, vol. 211, no. 1, pp. 1–8, 2008.

[40]   W. Wcislo and V. Gonzalez, "Social and ecological contexts of trophallaxis in facultatively social sweat bees, megalopta genalis and m. ecuadoria (hymenoptera, halictidae)," Insectes Sociaux, vol. 53, no. 2, pp. 220–225, 2006. doi: https://doi.org/10.1007/s00040-005-0861-6.

[41]   T. Schmickl and K. Crailsheim, "Trophallaxis among swarm-robots: A biologically inspired strategy for swarm robotics," in Biomedical Robotics and Biomechatronics, 2006. BioRob 2006. The First IEEE/RAS-EMBS International Conference on, IEEE, 2006, pp. 377–382. doi: 10.1109/BIOROB.2006.1639116.

[42]   A. F. Arif, A. R. Ramli, K. Samsudin, and S. Hashim, "Energy management in mobile robotics system based on biologically inspired honeybees behavior," in Computer Applications and Industrial Electronics (ICCAIE), 2011 IEEE International Conference on, IEEE, 2011, pp. 32–35. doi: 10.1109/ICCAIE.2011.6162099.

[43]   X. Lu, P. Wang, D. Niyato, D. I. Kim, and Z. Han, "Wireless charging technologies: Fundamentals, standards, and network applications," IEEE Communications Surveys & Tutorials, vol. 18, no. 2, pp. 1413–1452, 2016. doi: 10.1109/COMST.2015.2499783.

[44]   S. Sakoda, K. Takada, S. Suzuki, and K. Nakata, Non-contact power transmission apparatus, US Patent 8,248,027, 2012.

[45]   J.-O. Kim, C.-W. Moon, and H.-S. Ahn, "Image processing based a wireless charging system with two mobile robots," in Multimedia and Ubiquitous Engineering, Springer, 2013, pp. 769–775. doi: https://doi.org/10.1007/978-94-007-6738-6_95.

[46] J.-O. Kim and C. Moon, "A vision-based wireless charging system for robot trophallaxis," International Journal of Advanced Robotic Systems, vol. 12, no. 12, p. 177, 2015. doi: https://doi.org/10.5772/62043.

[47] L. Fukshansky, "Revisiting the hexagonal lattice: On optimal lattice circle packing," arXiv preprint arXiv:0911.4106, 2009.

[48] P. Sattayasoonthorn and J. Suthakorn, "Battery management for rescue robot operation," in Robotics and Biomimetics (ROBIO), 2016 IEEE International Conference on, IEEE, 2016, pp. 1227–1232. doi: 10.1109/ROBIO.2016.7866493.

[49] L. Olvitz, D. Vinko, and T. Švedek, "Wireless power transfer for mobile phone charging device," in MIPRO, 2012 Proceedings of the 35th International Convention, IEEE, 2012, pp. 141–145.

[50] V. G. Santos, L. C. Pimenta, and L. Chaimowicz, "Segregation of multiple heterogeneous units in a robotic swarm," in 2014 IEEE International Conference on Robotics and Automation (ICRA), IEEE, 2014, pp. 1112–1117.

[51] J. MacQueen et al., "Some methods for classification and analysis of multivariate observations," in Proceedings of the fifth Berkeley symposium on mathematical statistics and probability, Oakland, CA, USA, vol. 1, 1967, pp. 281–297.

[52] A. K. Jain, M. N. Murty, and P. J. Flynn, "Data clustering: A review," ACM computing surveys (CSUR), vol. 31, no. 3, pp. 264–323, 1999.

[53] B. Heap, "Permutations by interchanges," The Computer Journal, vol. 6, no. 3, pp. 293–298, 1963.

[54] D. Bruff, "The assignment problem and the hungarian method," Notes for Math, vol. 20, no. 29-47, p. 5, 2005.

[55] Y. Lee and J. B. Orlin, "On very large scale assignment problems," in Large Scale Optimization, Springer, 1994, pp. 206–244.

[56] B. Ristic, D. Angley, B. Moran, and J. L. Palmer, "Autonomous multi-robot search for a hazardous source in a turbulent environment," Sensors, vol. 17, no. 4, p. 918, 2017.

[57] D. S. Apostolopoulos, L. Pedersen, B. N. Shamah, K. Shillcutt, M. D. Wagner, and W. L. Whittaker, "Robotic antarctic meteorite search: Outcomes," in Robotics and Automation, 2001. Proceedings 2001 ICRA. IEEE International Conference on, IEEE, vol. 4, 2001, pp. 4174–4179.

[58] J. H. Lever, A. Streeter, and L. Ray, "Performance of a solar-powered robot for polar instrument networks," in Robotics and Automation, 2006. ICRA 2006. Proceedings 2006 IEEE International Conference on, IEEE, 2006, pp. 4252–4257.

[59] L. Valenziano and G. Dall'Oglio, "Millimetre astronomy from the high antarctic plateau: Site testing at dome c," Publications of the Astronomical Society of Australia, vol. 16, no. 2, pp. 167–174, 1999.

[60] B. Ratnakumar, M. Smart, A. Kindler, H. Frank, R. Ewell, and S. Surampudi, "Lithium batteries for aerospace applications: 2003 mars exploration rover," Journal of power sources, vol. 119, pp. 906–910, 2003.

[61] Y. Ji, Y. Zhang, and C.-Y. Wang, "Li-ion cell operation at low temperatures," Journal of The Electrochemical Society, vol. 160, no. 4, A636–A649, 2013.

[62] C. Gilbert, G. Robertson, Y. Le Maho, Y. Naito, and A. Ancel, "Huddling behavior in emperor penguins: Dynamics of huddling," Physiology & Behavior, vol. 88, no. 4, pp. 479–488, 2006. doi: https://doi.org/10.1016/j.physbeh.2006.04.024. [Online]. Available: http://www.sciencedirect.com/science/article/pii/S003193840600182X.

[63] C. D. Hassall, R. Bhargava, T. Trappenberg, and O. E. Krigolson, "A robust wall-following robot that learns by example," in Dalhousie Computer Science In-House Conference (DCSI), 2012.

[64] M. Rubenstein, A. Cornejo, and R. Nagpal, "Programmable self-assembly in a thousand-robot swarm," Science, vol. 345, no. 6198, pp. 795–799, 2014.

[65] M. Rubenstein, C. Ahler, and R. Nagpal, "Kilobot: A low cost scalable robot system for collective behaviors," in Robotics and Automation (ICRA), 2012 IEEE International Conference on, IEEE, 2012, pp. 3293–3298.

[66] T. Mina and B.-C. Min, "Penguin huddling-inspired energy sharing and formation movement in multi-robot systems," in 2018 IEEE International Symposium on Safety, Security, and Rescue Robotics (SSRR), IEEE, 2018, pp. 1–8.

[67] B. Mitchinson, M. Pearson, A. G. Pipe, and T. J. Prescott, "Biomimetic robots as scientific models: A view from the whisker tip," Neuromorphic and Brain-Based Robots, pp. 23–57, 2011.

[68] S. Soltic and N. Kasabov, "A biologically inspired evolving spiking neural model with rank-order population coding and a taste recognition system case study," System and Circuit Design for Biologically-Inspired Intelligent Learning, p. 136, 2011.

[69] L. I. Helgadottir, J. Haenicke, T. Landgraf, R. Rojas, and M. P. Nawrot, "Conditioned behavior in a robot controlled by a spiking neural network," in Neural Engineering (NER), 2013 6th International IEEE/EMBS Conference on, IEEE, 2013, pp. 891–894.

[70] N. E. Leonard and E. Fiorelli, "Virtual leaders, artificial potentials and coordinated control of groups," in Decision and Control, 2001. Proceedings of the 40th IEEE Conference on, IEEE, vol. 3, 2001, pp. 2968–2973.

[71] A. Wilson and R. Adams, "Gaussian process kernels for pattern discovery and extrapolation," in International Conference on Machine Learning, 2013, pp. 1067–1075.

[72] M. Mamei, M. Vasirani, and F. Zambonelli, "Experiments of morphogenesis in swarms of simple mobile robots," Applied Artificial Intelligence, vol. 18, no. 9-10, pp. 903–919, 2004.

[73] R. Nagpal, "Programmable self-assembly using biologically-inspired multirobot control," in ACM Joint Conference on Autonomous Agents and Multiagent Systems, ACM Press Bologna, I, 2002.

[74] R. Nagpal, H. Shrobe, and J. Bachrach, "Organizing a global coordinate system from local information on an ad hoc sensor network," in Information processing in sensor networks, Springer, 2003, pp. 333–348.

[75] R. D. Poor, "Embedded networks: Pervasive, low-power, wireless connectivity," PhD thesis, Massachusetts Institute of Technology, 2001.

[76] R. Gerum, B. Fabry, C. Metzner, M. Beaulieu, A. Ancel, and D. Zitterbart, "The origin of traveling waves in an emperor penguin huddle," New Journal of Physics, vol. 15, no. 12, p. 125 022, 2013.

[77] F. Mondada, M. Bonani, X. Raemy, J. Pugh, C. Cianci, A. Klaptocz, S. Magnenat, J.-C. Zufferey, D. Floreano, and A. Martinoli, "The e-puck, a robot designed for education in engineering," in Proceedings of the 9th conference on autonomous robot systems and competitions, Castelo Branco, Portugal, vol. 1, 2009, pp. 59–65.

[78] J. McLurkin, A. McMullen, N. Robbins, G. Habibi, A. Becker, A. Chou, H. Li, M. John, N. Okeke, J. Rykowski, et al., "A robot system design for low-cost multi-robot manipulation," in 2014 IEEE/RSJ International Conference on Intelligent Robots and Systems, IEEE, 2014, pp. 912–918.

[79] F. Arvin, J. Murray, C. Zhang, and S. Yue, "Colias: An autonomous micro robot for swarm robotic applications," International Journal of Advanced Robotic Systems, vol. 11, no. 7, p. 113, 2014.

[80] W. Qiao and R. Sipahi, "Consensus control under communication delay in a three-robot system: Design and experiments," IEEE Transactions on Control Systems Technology, vol. 24, no. 2, pp. 687–694, 2016.

[81] X. He, Z. Wang, and D. Zhou, "Robust fault detection for networked systems with communication delay and data missing," Automatica, vol. 45, no. 11, pp. 2634–2639, 2009.

[82] G. Antonelli, F. Arrichiello, and S. Chiaverini, "The entrapment/escorting mission," IEEE Robotics & Automation Magazine, vol. 15, no. 1, pp. 22–29, 2008.

[83] K.-K. Oh, M.-C. Park, and H.-S. Ahn, "A survey of multi-agent formation control," Automatica, vol. 53, pp. 424–440, 2015.

[84] C. Belta and V. Kumar, "Abstraction and control for groups of robots," IEEE Transactions on robotics, vol. 20, no. 5, pp. 865–875, 2004.

[85] R. Gayle, W. Moss, M. C. Lin, and D. Manocha, "Multi-robot coordination using generalized social potential fields," in 2009 IEEE International Conference on Robotics and Automation, IEEE, 2009, pp. 106–113.

[86] Y. Ikemoto, Y. Hasegawa, T. Fukuda, and K. Matsuda, "Gradual spatial pattern formation of homogeneous robot group," Information Sciences, vol. 171, no. 4, pp. 431–445, 2005.

[87] H.-T. Zhang, Z. Chen, and M.-C. Fan, "Collaborative control of multivehicle systems in diverse motion patterns," IEEE Transactions on Control Systems Technology, vol. 24, no. 4, pp. 1488–1494, 2016.

[88] S. Takahashi, K. Yoshida, T. Kwon, K. H. Lee, J. Lee, and S. Y. Shin, "Spectral-based group formation control," in Computer Graphics Forum, Wiley Online Library, vol. 28, 2009, pp. 639–648.

[89] R. Olfati-Saber and R. M. Murray, "Consensus problems in networks of agents with switching topology and time-delays," IEEE Transactions on automatic control, vol. 49, no. 9, pp. 1520–1533, 2004.

[90] W. Ren and R. W. Beard, "Consensus seeking in multiagent systems under dynamically changing interaction topologies," IEEE Transactions on automatic control, vol. 50, no. 5, pp. 655–661, 2005.

[91] W. Yu, G. Chen, J. Lu, and J. Kurths, "Synchronization via pinning control on general complex networks," SIAM Journal on Control and Optimization, vol. 51, no. 2, pp. 1395–1416, 2013.

[92] Z. Li, W. Ren, X. Liu, and M. Fu, "Consensus of multi-agent systems with general linear and lipschitz nonlinear dynamics using distributed adaptive protocols," IEEE Transactions on Automatic Control, vol. 58, no. 7, pp. 1786–1791, 2013.

[93] J. Wang and M. Xin, "Integrated optimal formation control of multiple unmanned aerial vehicles," IEEE Transactions on Control Systems Technology, vol. 21, no. 5, pp. 1731–1744, 2013.

[94] A. Karimoddini, H. Lin, B. M. Chen, and T. H. Lee, "Hybrid three-dimensional formation control for unmanned helicopters," Automatica, vol. 49, no. 2, pp. 424–433, 2013.

[95] Z. Ding and Z. Li, "Distributed adaptive consensus control of nonlinear output-feedback systems on directed graphs," Automatica, vol. 72, pp. 46–52, 2016.

[96] B. Wang, J. Wang, B. Zhang, and X. Li, "Global cooperative control framework for multiagent systems subject to actuator saturation with industrial applications," IEEE Transactions on Systems, Man, and Cybernetics: Systems, vol. 47, no. 7, pp. 1270–1283, 2017.

[97] X. Dong, B. Yu, Z. Shi, and Y. Zhong, "Time-varying formation control for unmanned aerial vehicles: Theories and applications," IEEE Transactions on Control Systems Technology, vol. 23, no. 1, pp. 340–348, 2015.

[98] Z. Ding, "Distributed adaptive consensus output regulation of network-connected heterogeneous unknown linear systems on directed graphs," IEEE Transactions on Automatic Control, vol. 62, no. 9, pp. 4683–4690, 2017.

[99] X. Dong, Y. Zhou, Z. Ren, and Y. Zhong, "Time-varying formation tracking for second-order multi-agent systems subjected to switching topologies with application to quadrotor formation flying," IEEE Transactions on Industrial Electronics, vol. 64, no. 6, pp. 5014–5024, 2017.

[100] J. A. Fax and R. M. Murray, "Information flow and cooperative control of vehicle formations," IFAC Proceedings Volumes, vol. 35, no. 1, pp. 115–120, 2002.

[101] L. Krick, M. E. Broucke, and B. A. Francis, "Stabilisation of infinitesimally rigid formations of multi-robot networks," International Journal of control, vol. 82, no. 3, pp. 423–439, 2009.

[102] F. Dorfler and B. Francis, "Geometric analysis of the formation problem for autonomous robots," IEEE Transactions on Automatic Control, vol. 55, no. 10, pp. 2379–2384, 2010.

[103] B. D. Anderson, C. Yu, B. Fidan, and J. M. Hendrickx, "Rigid graph control architectures for autonomous formations," IEEE Control Systems Magazine, vol. 28, no. 6, pp. 48–63, 2008.

[104] Y.-H. Lee, S.-G. Kim, T.-Y. Kuc, J.-K. Park, S.-H. Ji, Y.-S. Moon, and Y.-J. Cho, "Virtual target tracking of mobile robot and its application to formation control," International Journal of Control, Automation and Systems, vol. 12, no. 2, pp. 390–398, 2014.

[105] Y. Zhu, S. J. Gortler, and D. Thurston, "Sensor network localization using sensor perturbation," ACM Transactions on Sensor Networks (TOSN), vol. 7, no. 4, p. 36, 2011.

[106] M. Cao, C. Yu, and B. D. Anderson, "Formation control using range-only measurements," Automatica, vol. 47, no. 4, pp. 776–781, 2011.

[107] Y.-P. Tian and Q. Wang, "Global stabilization of rigid formations in the plane," Automatica, vol. 49, no. 5, pp. 1436–1441, 2013.

[108] M. Bayat and A. P. Aguiar, "Auv range-only localization and mapping: Observer design and experimental results," in 2013 European Control Conference (ECC), IEEE, 2013, pp. 4394–4399.

[109] B. Jiang, M. Deghat, and B. D. Anderson, "Translational velocity consensus using distance-only measurements," in 52nd IEEE Conference on Decision and Control, IEEE, 2013, pp. 2746–2751.

[110] R. Vidal, O. Shakernia, and S. Sastry, "Formation control of nonholonomic mobile robots with omnidirectional visual servoing and motion segmentation," in ICRA, 2003, pp. 584–589.

[111] P. Renaud, E. Cervera, and P. Martiner, "Towards a reliable vision-based mobile robot formation control," in 2004 IEEE/RSJ International Conference on Intelligent Robots and Systems (IROS)(IEEE Cat. No. 04CH37566), IEEE, vol. 4, 2004, pp. 3176–3181.

[112] L. Vig and J. A. Adams, "Multi-robot coalition formation," IEEE transactions on robotics, vol. 22, no. 4, pp. 637–649, 2006.

[113] G. L. Mariottini, F. Morbidi, D. Prattichizzo, G. J. Pappas, and K. Daniilidis, "Leader-follower formations: Uncalibrated vision-based localization and control," in Proceedings 2007 IEEE International Conference on Robotics and Automation, IEEE, 2007, pp. 2403–2408.

146

[114] B. Fidan, V. Gazi, S. Zhai, N. Cen, and E. Karataş, "Single-view distance-estimation-based formation control of robotic swarms," IEEE Transactions on Industrial Electronics, vol. 60, no. 12, pp. 5781–5791, 2013.

[115] R. J. Qureshi, J.-Y. Ramel, and H. Cardot, "Graph based shapes representation and recognition," in International Workshop on Graph-Based Representations in Pattern Recognition, Springer, 2007, pp. 49–60.

[116] M.-Y. Chow, S. Chiaverini, and C. Kitts, "Guest editorial introduction to the focused section on mechatronics in multirobot systems," IEEE/ASME Transactions on Mechatronics, vol. 14, no. 2, pp. 133–140, 2009.

[117] W. Wan, B. Shi, Z. Wang, and R. Fukui, "Multirobot object transport via robust caging," IEEE Transactions on Systems, Man, and Cybernetics: Systems, vol. 50, no. 1, pp. 270–280, 2020.

[118] G. A. Pereira, M. F. Campos, and V. Kumar, "Decentralized algorithms for multi-robot manipulation via caging," The International Journal of Robotics Research, vol. 23, no. 7-8, pp. 783–795, 2004.

[119] A. Rodriguez, M. T. Mason, and S. Ferry, "From caging to grasping," The International Journal of Robotics Research, vol. 31, no. 7, pp. 886–900, 2012.

[120] P. Pipattanasomporn and A. Sudsang, "Two-finger caging of nonconvex polytopes," IEEE Transactions on Robotics, vol. 27, no. 2, pp. 324–333, 2011.

[121] W. Wan and R. Fukui, "Efficient planar caging test using space mapping," IEEE Transactions on Automation Science and Engineering, vol. 15, no. 1, pp. 278–289, 2016.

[122] M. Cai, S. Wang, Y. Wang, R. Wang, and M. Tan, "Coordinated control of underwater biomimetic vehicle-manipulator system for free floating autonomous manipulation," IEEE Transactions on Systems, Man, and Cybernetics: Systems, vol. Early Access, 2019.

[123] H. Hajieghrary, D. Kularatne, and M. A. Hsieh, "Differential geometric approach to trajectory planning: Cooperative transport by a team of autonomous marine vehicles," in 2018 Annual American Control Conference (ACC), IEEE, 2018, pp. 858–863.

[124] N. Michael, J. Fink, and V. Kumar, "Cooperative manipulation and transportation with aerial robots," Autonomous Robots, vol. 30, no. 1, pp. 73–86, 2011.

[125] G. Wu and K. Sreenath, "Geometric control of multiple quadrotors transporting a rigid-body load," in 53rd IEEE Conference on Decision and Control, IEEE, 2014, pp. 6141–6148.

[126] C. R. Kube and H. Zhang, "Collective robotics: From social insects to robots," Adaptive behavior, vol. 2, no. 2, pp. 189–218, 1993.

[127] C. R. Kube, "Task modelling in collective robotics," Autonomous Robots, vol. 4, no. 1, pp. 53–72, 1997.

[128] C. R. Kube and E. Bonabeau, "Cooperative transport by ants and robots," Robotics and Autonomous Systems, vol. 30, no. 1-2, pp. 85–101, 2000.

[129] B. P. Gerkey and M. J. Mataric, "Pusher-watcher: An approach to fault-tolerant tightly-coupled robot coordination," in Proceedings 2002 IEEE International Conference on Robotics and Automation (Cat. No. 02CH37292), IEEE, vol. 1, 2002, pp. 464–469.

[130] M. H. M. Alkilabi, A. Narayan, and E. Tuci, "Cooperative object transport with a swarm of e-puck robots: Robustness and scalability of evolved collective strategies," Swarm Intelligence, vol. 11, no. 3-4, pp. 185–209, 2017.

[131] M. A. Neumann, M. H. Chin, and C. A. Kitts, "Object manipulation through explicit force control using cooperative mobile multi-robot systems," in Proceedings of the World Congress on Engineering and Computer Science, vol. 1, 2014.

[132] Z. Wang, E. Nakano, and T. Takahashi, "Solving function distribution and behavior design problem for cooperative object handling by multiple mobile robots," IEEE Transactions on Systems, Man, and Cybernetics-Part A: Systems and Humans, vol. 33, no. 5, pp. 537–549, 2003.

[133] R. G. Brown and J. S. Jennings, "A pusher/steerer model for strongly cooperative mobile robot manipulation," in Proceedings 1995 IEEE/RSJ International Conference on Intelligent Robots and Systems. Human Robot Interaction and Cooperative Robots, IEEE, vol. 3, 1995, pp. 562–568.

[134] J. Chen, M. Gauci, W. Li, A. Kolling, and R. Groß, "Occlusion-based cooperative transport with a swarm of miniature mobile robots," IEEE Transactions on Robotics, vol. 31, no. 2, pp. 307–321, 2015.

[135] G. Kapellmann-Zafra, J. Chen, and R. Groß, "Using google glass in human–robot swarm interaction," in Annual Conference Towards Autonomous Robotic Systems, Springer, 2016, pp. 196–201.

[136] M. A. Neumann and C. A. Kitts, "A hybrid multirobot control architecture for object transport," IEEE/ASME Transactions on Mechatronics, vol. 21, no. 6, pp. 2983–2988, 2016.

[137] A. Stroupe, T. Huntsberger, A. Okon, H. Aghazarian, and M. Robinson, "Behavior-based multi-robot collaboration for autonomous construction tasks," in 2005 IEEE/RSJ International Conference on Intelligent Robots and Systems, IEEE, 2005, pp. 1495–1500.

[138] Z. Wang and M. Schwager, "Kinematic multi-robot manipulation with no communication using force feedback," in 2016 IEEE International Conference on Robotics and Automation (ICRA), IEEE, 2016, pp. 427–432.

[139] P. K. Agarwal, J.-C. Latombe, R. Motwani, and P. Raghavan, "Nonholonomic path planning for pushing a disk among obstacles," in Proceedings of International Conference on Robotics and Automation (ICRA), IEEE, vol. 4, 1997, pp. 3124–3129.

[140] M. De Berg and D. H. Gerrits, "Computing push plans for disk-shaped robots," International Journal of Computational Geometry & Applications, vol. 23, no. 01, pp. 29–48, 2013.

[141] G. Lee, T. Lozano-Pérez, and L. P. Kaelbling, "Hierarchical planning for multi-contact non-prehensile manipulation," in 2015 IEEE/RSJ International Conference on Intelligent Robots and Systems (IROS), IEEE, 2015, pp. 264–271.

[142] K. Miyazawa, Y. Maeda, and T. Arai, "Planning of graspless manipulation based on rapidly-exploring random trees," in (ISATP 2005). The 6th IEEE International Symposium on Assembly and Task Planning: From Nano to Macro Assembly and Manufacturing, 2005., IEEE, 2005, pp. 7–12.

[143] T. Yoshikawa and M. Kurisu, "Indentification of the center of friction from pushing an object by a mobile robot," in Proceedings IROS'91: IEEE/RSJ International Workshop on Intelligent Robots and Systems' 91, IEEE, 1991, pp. 449–454.

[144] A. Inceoglu, C. Koc, B. O. Kanat, M. Ersen, and S. Sariel, "Continuous visual world modeling for autonomous robot manipulation," IEEE Transactions on Systems, Man, and Cybernetics: Systems, vol. 49, no. 1, pp. 192–205, 2018.

[145] M. Bauza and A. Rodriguez, "A probabilistic data-driven model for planar pushing," in 2017 IEEE International Conference on Robotics and Automation (ICRA), IEEE, 2017, pp. 3008–3015.

[146] K.-T. Yu, M. Bauza, N. Fazeli, and A. Rodriguez, "More than a million ways to be pushed. a high-fidelity experimental dataset of planar pushing," in 2016 IEEE/RSJ International Conference on Intelligent Robots and Systems (IROS), IEEE, 2016, pp. 30–37.

[147] J. Stüber, C. Zito, and R. Stolkin, "Let's push things forward: A survey on robot pushing," Frontiers in Robotics and AI, vol. 7, p. 8, 2020.

[148] Z. Wang, Y. Takano, Y. Hirata, and K. Kosuge, "Decentralized cooperative object transportation by multiple mobile robots with a pushing leader," in Distributed Autonomous Robotic Systems 6, Springer, 2007, pp. 453–462.

[149] O. Khatib, "Real-time obstacle avoidance for manipulators and mobile robots," in Autonomous robot vehicles, Springer, 1986, pp. 396–404.

[150] E. Rohmer, S. P. Singh, and M. Freese, "V-rep: A versatile and scalable robot simulation framework," in 2013 IEEE/RSJ International Conference on Intelligent Robots and Systems (IROS), IEEE, 2013, pp. 1321–1326.

[151] K. Smith and S. C. Goldstein, "Programmable matter: Applications for gastrointestinal endoscopy and surgery," Gastroenterology, vol. 140, no. 7, pp. 1884–1886, 2011.

[152] J.-Q. Liu and T. Nakano, "Principles and methods for nanomechatronics: Signaling, structure, and functions toward nanorobots," IEEE Transactions on Systems, Man, and Cybernetics, Part C (Applications and Reviews), vol. 42, no. 3, pp. 357–366, 2011.

[153] H. Wei, C. Shen, and Y. Shi, "Distributed lyapunov-based model predictive formation tracking control for autonomous underwater vehicles subject to disturbances," IEEE Transactions on Systems, Man, and Cybernetics: Systems, vol. Early Access, 2019.